Nature Communications

https://doi.org/10.1038/s41467-026-71476-y

Article in Press

D-π-A sensitized carbon dots as long-lived type-I/II photosensitizers for NIR-excited hypoxia-regulated photodynamic therapy

Received: 28 October 2025

Accepted: 24 March 2026

Cite this article as: Zhang, Z., Yan, L., Li, W. *et al.* D-π-A sensitized carbon dots as long-lived type-I/II photosensitizers for NIR-excited hypoxia-regulated photodynamic therapy. *Nat Commun* (2026). https://doi.org/10.1038/s41467-026-71476-y

Zhenlin Zhang, Lang Yan, Weiwei Li, Jinyan Hu, Yang Wang, Hongjing Dou, Dengyu Pan, Longxiang Shen, Sheng Shi & Bijiang Geng

D-π-A sensitized carbon dots as long-lived type-I/II photosensitizers for NIR-excited hypoxia-regulated photodynamic therapy

Zhenlin Zhang[1,Δ], Lang Yan[2,Δ], Weiwei Li[1,Δ], Jinyan Hu[1], Yang Wang[3], Hongjing Dou[4], Dengyu Pan[1]*, Longxiang Shen[3]*, Sheng Shi[5]*, Bijiang Geng[1]*

[1] School of Environmental and Chemical Engineering, Shanghai University, Shanghai 200444, China

[2] Department of Health Toxicology, College of Naval Medicine, Naval Medical University, Shanghai 200433, China

[3] Department of Orthopedic Surgery, Shanghai Sixth People's Hospital Affiliated to Shanghai Jiao Tong University School of Medicine, Shanghai 200233, China

[4] State Key Laboratory of Metal Matrix Composites, School of Materials Science and Engineering, Shanghai Jiao Tong University, Shanghai 200240, China

[5] Department of Orthopedics, Shanghai Tenth People's Hospital, Tongji University, Shanghai 200072, China.

[Δ] These authors contributed equally to this work.

*Correspondence should be addressed to D.P. (e-mail: dypan617@shu.edu.cn) or to L.S. (7250012700@shsmu.edu.cn) or to S.S. (shisheng273@163.com) or to B.G. (e-mail: bjgeng1992@shu.edu.cn)

Abstract

In the development of clinically translatable triplet photosensitizers for hypoxia regulated photodynamic therapy (PDT), there is an unmet need for engineering sensitizers as near-infrared (NIR)-responsive, type I/type II dual photosensitizers and mild photothermal agents. Herein, we develop a binary precursor-engineering strategy for precise regulation of the D-π-A configuration of carbon dots (CDs) as ultralong-lived triplet, type I/II dual photosensitizers by utilizing phenolic hydroxyl as an electron-rich donor and pyridine N as an electron-withdrawing acceptor. The photodynamic performance of CDs is enhanced by intramolecular charge transfer and mild photothermal conversion. We further design M1-like macrophage-derived cell membrane-camouflaged CDs to realize preferential tumor accumulation while guaranteeing rapid systemic clearance. D-π-A sensitized CD-mediated PDT induces anti-tumor activity against primary and distant tumors. Our work highlights the crucial roles of D-π-A sensitization of CDs in boosting PDT by triplet state tuning, surface charge transfer, and mild photothermal relief of hypoxia.

Introduction

Phototherapy including photodynamic and photothermal therapy (PDT/PTT) utilizes light of a specific wavelength to activate photosensitizers (PSs) or photothermal conversion reagents enriched in the tumor site, and selectively kills tumors by generating cytotoxic reactive oxygen

species (ROS) or local hyperthermia with spatiotemporal precision.[1-5] Recently, both PDT and PTT have demonstrated their ability to elicit immunogenic immune responses for photoimmunotherapy against both primary and abscopal/metastatic tumors, and thus hold potential for establishing long-term cancer-free health.[6-10] While PTT also induces immunogenic cell death (ICD) to activate innate immunity, significant ICD of irradiated tumor cells was induced by PTT only in a high photothermal window (50−60 °C).[11-13] This means that high doses of irradiation at a high laser power density is required to effectively trigger ICD for photothermal immunotherapy, which instead may raise severe concerns about thermal damage to the surrounding anatomical structures, including blood vessels, ECM scaffolds and nerves.[14-17] In contrast, immunogenic PDT is superior to immunogenic PTT in photoimmunotherapy since irradiation at rather lower laser power density can trigger desirable ICD mode of tumor cells.[18-20] However, the effectiveness of PDT for photoimmunotherapy is subject to the hypoxic tumor microenvironment (TME), since conventional PDT generates ROS typically in the single product of only $^1O_2$ through the energy-transfer type-II mechanism that is highly dependent on oxygen level.[21-23] Albeit respective drawbacks for PTT or PDT as a single treatment mode, type-II PDT and mild PTT may synergize to enhance phototherapy efficacy owing to partial alleviation of hypoxia by mild hyperthermia. With rapid development in multimodal nanoplatforms composed of photodynamically and photothermally active agents, PDT/PTT combinations have recently gained momentum in tumor phototherapy.[24-27] Nevertheless, currently available PDT/PTT combined systems suffer from two intrinsic shortcomings. On the one hand, owing to a lack of a common optimal excitation wavelength for PDT and PTT agents, the utilization of two different lasers for sequential excitation

complicates treatment and prolongs treatment duration.[28-31] On the other hand, although the dual modes can be triggered by a single near-infrared (NIR) laser, relatively high-power photoirradiation or utilization of highly efficient photothermal agents is required, leading to an interrupted tumor perfusion and oxygenation owing to hyperthermia-induced vascular damage and collapse.[32-34]

Very recently, an emerging class of PSs with type-I and type-II dual modes have been developed as alternative avenues for treating normoxic/hypoxic tumors by switching between oxygen-dependent type-II and oxygen-independent type-I mechanisms based on local oxygen concentration.[25,35,36] Different from the energy-transfer type-II mechanism, the type-I mechanism works by photoinduced single electrons transferring to molecular oxygen in a low O_2-dependence and reduction manner to produce superoxide radical ($O_2^{\bullet-}$) or/and hydroxyl radical (•OH).[24,37-39] To date, most type-I/II PSs are constructed from inorganic semiconducting nanomaterials, whose electron-hole separation and charge transfer can be enhanced by surface defects or/and heterojunctions.[18,37,40,41] Despite they show excellent photostability compared to less-stable organic PSs, their PDT applications are limited by short absorption/excitation wavelengths, ultrashort excited-state lifetimes (~ ns), and poor biocompatibility owing to metal toxicity and less degradability.[42,43] It is still a terrible challenge to develop single-component, metal-free, NIR-responsive, type-I/II photosensitizers with matching photothermal tunability, high photostability and high biocompatibility to meet the above standard for robust photoimmunotherapy.

As a metal-free zero-dimensional semiconductor, carbon dots (CDs) have garnered increasing attention for a wide range of applications, since their electronic, optical and catalytic properties

can be facilely tailored through molecular engineering, by which functional groups containing heteroatoms of O, N, S with lone pairs of electrons can be in situ incorporated at core and surface sites during hydrothermal/solvothermal processes.[44-49] Given their superior properties, such as high photostability, high biocompatibility, excellent water-solubility, and tunable fluorescent or phosphorescent properties, small-sized CDs have been extensively employed as highly stable and kidney-excretable theranostic agents for bioimaging and imaging guided tumor multimodal treatments, including sonodynamic therapy (SDT), PTT, and type-I/II PDT.[50,51] As type-I/II PSs, however, all CDs reported so far exhibit ultrashort excited state lifetimes (~ ns), leading to unsatisfactory PDT efficacy owing to inefficient triplet population through intersystem crossing.[52,53] Moreover, most CDs exhibited a wide bandgap, with absorption/excitation wavelengths in the UV-vis range.[54,55] Although there also were a few reports on NIR-responsive type-I/II CDs excited at 808 nm, light intensity of 0.8-1.0 W cm^{-2} was still required, which far exceeds the maximum permissible exposure (MPE) (808 nm, 0.33 W cm^{-2}) to skin and tissue.[2,56]

In this work, we report the rational design of D-π-A sensitized photodynamic CDs as NIR-excited type-I/II sensitizers for hypoxia regulated photodynamic immunotherapy, which inspires by the design principle of D-A sensitized molecular photosensitizers. Generally, D-A sensitized photosensitizers are organic molecules designed to enhance the efficiency of photovoltaic or photodynamic processes in dye-sensitized solar cells and photodynamic therapy by harnessing the properties of donor (D) and acceptor (A) components.[57-59] Especially, the D-π-A structure facilitates electron transfer between the donor and acceptor groups through an extended π bridge for enhancing type-I/II photodynamic performances.[60-62] As an extended π-conjugated nano-

system of CDs in the D-π-A configuration, electron-rich oxygen atoms from -OH modifications at edge sites significantly improve the electron-donating capability, which combine with electron-withdrawing moieties (largely pyridinic N) to form the D-π-A configuration, resulting in an elongated triplet state lifetime (tens of ms), an enhanced intramolecular charge transfer, and a reduced bandgap (1.49 eV). To demonstrate the CD-based design of the D-π-A sensitized type-I/II PSs and the precise regulation of PDT/PTT performances of CDs, a molecular-engineering combination strategy is employed to synthesize three types of CDs with different regional modifications from two molecular precursors: O-CDs from OPD + ICG, M-CDs from MPD + ICG, and P-CDs from PPD + ICG (Fig. 1). Among them, D-π-A type CDs (P-CDs) with an average carrier lifetime of 36.32 ms demonstrate the highest efficacy in generation of both $^1O_2$ and $O_2^{\bullet-}$ but the lowest photothermal conversion efficiency (32.2%), revealing the D-π-A enhanced type-I/II photodynamic mechanisms. In contrast, donor N-rich (pyrrolic N) yet acceptor-deficient M-CDs as D-π-D type CDs show the highest photothermal conversion efficiency of 69.6% but the poor PDT efficacy. Mechanically, an intramolecular charge transfer (CT) state with a ultralong lifetime mediated by the D-π-A structure enables the enhanced PDT performance. Importantly, the hypoxia condition is substantially relieved by mild PTT + PDT, as evidenced by immunofluorescence staining of HIF-1α in tumor. We further design and synthesize M1-like macrophage-derived cell membrane (MM)-camouflaged P-CDs (P-CD@MM) to realize preferential tumor accumulation while guarantee rapid systemic clearance. On the one hand, the encapsulation of P-CDs in MM can prevent the rapid clearance of CDs, actively targeting the tumor tissue to improve the tumor accumulation level of P-CDs. On the other hand, MM-encapsulated P-CD can enhance reversion

of the immunosuppressive TME and realize the cascade amplification of antitumor immune response through triggering ICD and reprogramming tumor-associated macrophages (TAMs) into antitumoral M1-like phenotype. Collectively, satisfactory therapeutic outcomes for primary and distant tumors are achieved by P-CD@MM-mediated precise PDT-enhanced immunotherapy at low laser power density of 0.30 W/cm^2 (808 nm). Our work highlights the crucial roles of D-π-A sensitization of CDs in boosting NIR-photoimmunotherapy by triplet state stabilization, surface charge transfer, and mild photothermal relief of hypoxia.

Results

Molecular engineering of D-π-A sensitized CDs. To screen D-π-A sensitized nanosensitizers from surface-functionalized CDs, we developed a one-step combination strategy for controllable solvothermal synthesis of a series of O, N, S co-doped NIR-CDs with narrow bandgaps by combining one of the three isomers of o-, m-, and p-phenylenediamines (OPD, MPD, PPD) with indocyanine green (ICG) as key precursors, as schemed in Fig. 2a. Benefited from the combination synthetic strategy, three kinds of NIR-CDs with an decreasing graphitization level and significantly reduce bandgaps (1.40-1.56 eV), denoted as O-CDs, M-CDs, and P-CDs, were successfully synthesized from OPD/ICG, MPD/ICG, PPD/ICG, respectively. In contrast, without the combination with ICG, N-doped CDs with wide bandgaps (1.93-2.28 eV) were derived from one of the phenylenediamine isomers (Supplementary Fig. 1), which was similar to the previous report.[63] On the other hand, without addition of any phenylenediamine isomers, the solvothermal treatment of only ICG precursor, O, S co-doped CDs (ICG-CDs) with slightly reduced bandgap

(1.92 eV) were synthesized (Fig. 2j), but exhibited a high oxygen content (19.27 at. %) and low carbonization level, as revealed by XPS and Raman characterization (Supplementary Fig. 2, 3a). As verified by evaluation of the potential in the following phototherapy for NIR-CDs, P-CDs were eventually screened out as superior a type-I photodynamic agent, while M-CDs were found to serve as a superior PTT agent, suggesting that the combination synthetic strategy was effective in the regulation of the PDT/PTT performances.

We then characterized the structural features of three distinct types of CDs and attempted to unveil the structure-activity relationship between the N doping types of CDs with the enhanced photothermal or photodynamic performances. TEM images presented in Fig. 2b-d demonstrated the successful preparation of these CDs, revealing their dot-like morphology. We also found that M-CD and P-CD exhibited comparable average diameters, measuring 1.69 ± 0.45 nm for M-CDs and 1.38 ± 0.40 nm for P-CDs, while O-CD displayed a significantly larger average size of 5.30 ± 0.75 nm. The high crystallinity of these CDs was confirmed by high-resolution TEM images (Fig. 2e-g), which revealed well-defined lattice fringes with a spacing of 0.21 nm, corresponding to the (100) crystallographic plane characteristic of graphitic carbon. Raman spectroscopy further validated the graphitic structures of all four types of CDs (Supplementary Fig. 3). The D/G intensity ratios for ICG-CD, O-CD, M-CD, and P-CD were determined to be 0.817, 0.784, 0.854, and 0.867, respectively, indicating the lowest degree of graphitization in P-CD, which could be ascribed to the presence of abundant surface functional groups. In addition, the para-configuration of PPD could impede the generation of ordered graphitic domains. The symmetrical structure of PPD lacks sufficient spatial degrees of freedom during the carbonization process, thereby

hindering effective structural rearrangement and aromatization. Therefore, many disordered structures are formed within the carbon core, leading to the low graphitization level of P-CDs. XPS analysis revealed that the content of N element in P-CD (10.31 at. %) was significantly higher than that of ICG-CD (3.06 at. %), O-CD (5.82 at. %), and M-CD (8.33 at. %) (Supplementary Fig. 2, 4-6). The predominant form of N in P-CD was pyridinic N, which exhibited peaks at 398.6 eV. In contrast, no peak of pyridinic N can be detected in the high-resolution N 1s spectrum of the other three CDs. However, M-CD contained graphitic N with a content of 3.19 at. %, suggesting that M-CD possessed graphitic N-doped features. For O-CD, no peaks of graphitic N and pyridinic N can be detected, illustrating that O-CD possessed pyrrolic N-doped characteristics (Fig. 2k). Collectively, we can confirm that M-CD had the characteristic of graphitic-N-doping, while P-CD possessed the features of pyridinic-N-doping. We also performed ^{1}H NMR and ^{13}C NMR analysis to clarify the specific structures and molecular arrangements of these CDs. As depicted in Supplementary Fig. 7a, the ^{1}H NMR exhibited that the peaks of P-CD and ICG monomers partially overlapped at δ 7.5-8.5 ppm, indicating that the conjugated motif of ICG composed of several -CH= units is likely retained in the extended π conjugated aromatic section in the P-CD, which can be beneficial to extend its absorption in the NIR region. However, the additional strong signal of hydroxyl (-OH) was observed at δ 6.35 ppm in the P-CD ^{1}H NMR spectrum, further confirming the structural characteristics of P-CD containing the -OH donor. Additionally, the ^{13}C NMR analysis of P-CD revealed the existence of conjugated carbon skeletons at δ 110-150 ppm, which were the basis of π bridges in the D-π-A structure, but such extended conjugated carbon skeletons cannot be observed in the ICG ^{13}C NMR spectrum (Supplementary Fig. 7b).

We further investigated the characteristics of surface functional groups of these CDs using FT-IR spectroscopy. As depicted in Supplementary Fig. 8, the broad peak at approximately 3430 cm^{-1} was detected in the three kinds of CDs, which indicated the presence of O-H or N-H on the edge of these CDs. Because O-CDs, M-CDs, and P-CDs all contain hydroxyl groups, we believe that the hydroxyl groups may originate from ethanol solvents during the solvothermal synthesis of O-CDs, M-CDs, and P-CDs. These surface functional groups could endow these CDs with good colloidal stability and dispersibility. Additionally, stretching vibration bands associated with $-SO_3$, C-N, C=N, and C-S were evident in the FT-IR spectrum, indicating the presence of SO_3^- and N-containing heterocycles in these CDs. Subsequently, we performed Zeta potential characterization to determine the surface charge characteristics of O-CD, M-CD, and P-CD. The measured values of zeta potential were found to be -21.63 ± 0.8 mV, -31.4 ± 0.8 mV, and -21.83 ± 0.4 mV, respectively (Supplementary Fig. 9). The characteristics of negative charges of these CDs could be ascribed to the presence of SO_3^- and O-H. The bandgap values of these CDs were determined by measuring their absorption spectra. As depicted in Fig. 2j, O-CD, M-CD, and P-CD exhibit broad UV to NIR absorption, with significant absorption bands observed between 600-850 nm, demonstrating that the doping of N could increase the NIR absorption of CDs. Based on the $(\alpha E)^2$-E diagram, the bandgap for O-CD, M-CD, and P-CD were calculated to be 1.56, 1.40, and 1.49 eV, respectively. In contrast, the absorption spectrum of ICG-CD was restricted to the UV-visible light region, displaying a band gap of 1.92 eV.

Photothermal properties of CDs. We performed NIR-responsive photothermal performance measurements on O-CDs, M-CDs and P-CDs to investigate the influence of N doping on the

photothermal conversion properties. To avoid damage to skin tissue caused by laser irradiation, we measured the PTT performances at low power density of 0.3 W/cm^2 with an 808 nm laser. We found that the temperature of the M-CD aqueous solution increased rapidly from 26 °C to 54.7 °C during 5 min irradiation (Fig. 3a and Supplementary Fig. 10), achieving a remarkable photothermal conversion efficiency of 69.6%. In contrast, P-CD and O-CD solutions exhibited slow rise in solution temperature and significantly lower conversion efficiencies at only 32.2% and 42.9%, respectively (Fig. 3b, c). We also performed photothermal stability evaluation of M-CD. As shown in Supplementary Fig. 11, after 9 cycles of heating and cooling, the temperature of M-CD still reached 53.7 ℃ under 808 nm laser irradiation (0.3 W/cm^2), indicating the excellent photothermal stability of M-CD. We monitored solution temperature changes with reduced laser-power (0.3-0.1 W/cm^2) and reduced concentration (0.1-0.3 mg/mL) under consistent irradiation of 808 nm laser. With decreasing laser-power or CD concentration, the photothermal effect of all the three CDs was markedly reduced (Fig. 3d-i). Notably, for P-CD solutions at low concentration (0.1 mg/mL) with 808 nm laser at low power density (0.3-0.1 W/cm^2), the rise in temperature was rather low (~10 °C), suggesting that P-CDs exhibited a rather mild NIR PTT effect compared with M-CDs. Previous reports have demonstrated that the doping of graphitic N and pyrrolic N with electron donating capability can trigger the red-shift of absorption spectrum of CDs, thereby improving their photothermal conversion properties. Indeed, M-CDs contained the highest N doping level (8.33 at. %) in forms of graphitic and pyrrolic N compared with other two CD samples, which endowed them with the highest photothermal conversion efficiency. For PTT-poor P-CDs, almost all N doping was in the pyridinic N form (an electron-withdrawing group) with absence of graphitic and

pyrrolic N, despite the highest N doping level (10.31 at. %). These results indicate that molecular engineering can be harnessed to regulate photothermal performances of NIR-responsive CDs as a photothermal conversion reagent by varying N doping level and N-contained species.

Enhanced photodynamic properties of P-CD. Having demonstrated the molecular regulation of the NIR photothermal effect of CDs, the NIR photodynamic property of the three types of CDs as type II and type I photosensitizers was then investigated first using DPBF as a chemical capture agent for ROS including singlet oxygen ($^1O_2$) and superoxide radicals ($O_2^{\bullet-}$) after photoreactions with an 808 nm laser (0.3 W/cm^2). As the irradiation time increased from 0 to 10 min, the characteristic absorption peak of DPBF at 418 nm diminished gradually (Fig. 4a). Among these CDs, P-CDs exhibited the strongest ROS generation efficiency. The ROS generation efficiency of P-CDs was measured to be 0.038 min^{-1}, which was approximately 2.9 times greater than that of O-CD and about 4.75 times greater than that of M-CD, respectively (Supplementary Fig. 12a). To differentiate the generated ROS type, we then utilized DHR123 as a specific fluorescent probe for detecting $O_2^{\bullet-}$. In the presence of $O_2^{\bullet-}$, DHR123 exhibited a distinct fluorescence emission peak at 525 nm. Following irradiation with an 808 nm laser, the fluorescence intensity induced by P-CDs was significantly enhanced, thereby confirming the generation of $O_2^{\bullet-}$ by the type I photodyanmic mechanism (Fig. 4c). Moreover, the $O_2^{\bullet-}$ generation efficiency in P-CD group was higher than that of M-CDs and O-CDs (Supplementary Fig. 12b), further demonstrating the enhanced type-I photodynamic activity of P-CDs in generation of $O_2^{\bullet-}$. To confirm the type I photodyanmic mechanism, we utilized the ESR spectrum to measure $O_2^{\bullet-}$ signals by using the DMPO as the scavenger for $O_2^{\bullet-}$. The characteristic ESR signal of $O_2^{\bullet-}$ in P-CDs was stronger than that in M-

CDs and O-CDs (Fig. 4e). Furthermore, the generation of another ROS type ($^1O_2$) was tested by ESR spectra using TEMP as the capture agent of $^1O_2$. Following irradiation for a duration of 5 minutes, three characteristic peaks exhibiting an intensity ratio of 1:1:1 were observed (Fig. 4f). The ESR signal intensity of TEMPO progressively increased from M-CDs to O-CDs and subsequently to P-CDs, verifying that P-CDs exhibited highest $^1O_2$ production efficiency. We then evaluated the photostability of P-CD through measuring photothermal conversion efficiency and ROS generation efficiency under multiple laser irradiations. As presented in Supplementary Fig. 13a, no significant change of the photothermal conversion efficiency of P-CD was detected during the six consecutive laser irradiation cycles. In addition, the $O_2^{\bullet-}$ generation efficiency of P-CD remained unchanged after five cycles (Supplementary Fig. 13b). These results demonstrated the good photostability of P-CD under multiple laser irradiations.

We then attempted to unveil the ambiguous structure-activity relationship of CD-based PSs owing to their complex components and understand why type II/I P-CDs possessed the strongest photodynamic property in greatly enhanced generation of $^1O_2$ and $O_2^{\bullet-}$ compared with the other CDs. For organic triplet PS molecules, the type II PDT mechanism has been widely accepted, which involves relatively stable population of long-lived triplet states (T_1) through photoexcitation from S_0 to S_n state, and then to T_1 by intersystem crossing (ISC). Excited PSs return from T_1 to S_0 state by energy transfer to triplet oxygen ($^3O_2$) to generate $^1O_2$. Accordingly, prolonging carrier lifetime in stable T_1 states is a crucial factor in augmenting photodynamic activity of triplet PSs. We determined their photoexcited carrier lifetime by measuring time-resolved PL spectra. For O-CDs and M-CDs, time-resolved PL spectra exhibited relatively rapid decay, with average lifetimes

of 2.02 ns and 8.88 ns determined, respectively (Fig. 4g, h), suggesting a characteristic for common fluorescent CDs with an ultrashort lifetime (~ ns). In contrast, P-CDs demonstrated slow phosphorescence decay with ultralong carrier lifetime of 36.32 ms, which was six orders of magnitude longer than those observed for O-CDs and M-CDs (Fig. 4i). These results suggest that P-CDs can emit phosphorescence rather than fluorescence. Given the enhanced catalytic potential of long-lived triplet excited states, we propose an enhanced mechanism for both $^1O_2$ and $O_2^{\bullet-}$ generation mediated by long-lived triplet excited states.

Spin-orbit coupling (SOC) serves as the primary driving force for ISC, a process that can be significantly enhanced by modifying the features of the participating triplet states. In accordance with the EI-Sayed rule, heteroatom groups such as oxygen, nitrogen, and sulfur—characterized by their abundant lone pairs of electrons—are incorporated into aromatic compounds to augment SOC and thus ISC. There is a negligible difference in heteroatom-induced SOC effect on electronic configurations since the total heteroatom content of O, N, S in O-CDs, M-CDs and P-CDs are 24.89%, 20.72%, 21.90%, respectively (Fig. 2i). However, notably, there is a large difference in contents of donor and acceptor groups between donor-rich, acceptor-rich CDs (P-CDs) and donor-rich yet acceptor-deficient CDs (M-CDs and O-CDs). Since D-A sensitized photosensitizers commonly possess stable triplet states with lifetime of ~ μs to ms, we further proposed that phosphorescent P-CDs have a D-π-A configuration with a long-lived intramolecular charge transfer (CT) state, which may facilitate electron transfer between the donor and acceptor groups through an extended π bridge for enhancing type-I/II photodynamic performances (Fig. 2h, 4i). In contrast, donor-rich yet acceptor-deficient O-CDs and M-CDs with a D-π-D configuration

exhibited low-efficacy type-I photodynamic performances likely owing to absence of effective intramolecular CT between the donor and acceptor groups. Intramolecular CT excited states in D-A sensitized photosensitizers generally exhibit solvent polarity-dependent optical properties such as red shift in emitting wavelength with increasing solvent polarity. To test this, we measured PL spectra of O-CDs, M-CDs and P-CDs in solvents (EA, acetone, EtOH, and H_2O) with increased polarity ordering. It was found that there was a pronounced PL red shift effect consistently induced by solvent polarity in P-CDs, while in M-CDs and O-CDs, the solvent polarity effect on PL red-shift or blue-shift was irregular (Fig. 4j). Combining the long-lived T_1 and solvent polarity effect clearly revealed the evidence for D-π-A sensitized type II/I photodynamic mechanism of molecule-engineered CDs with enhanced charge-transfer dynamics.

To highlight the advantages of the D-π-A configured P-CDs, we compared the excited-state lifetime, ROS generation efficiency, and hypoxic adaptability between D-π-A structured CDs (P-CDs), traditional CDs (O-CD), and commercial photosensitizers (ICG, TCPP). First, P-CDs exhibited ultralong triplet state lifetime of 36.32 ms, which was six orders of magnitude longer than those observed for O-CDs and M-CDs (Fig. 4i). The triplet state lifetime of P-CDs was also significantly higher than that of commercial photosensitizers (0.8 ns for ICG and 8.48 ns for TCPP) (Supplementary Table 1). Second, this ultralong triplet state lifetime is a crucial factor in augmenting photodynamic activity of P-CDs. The calculated $^1O_2$ quantum yield of P-CD was measured to be 1.49%, which was much higher than that of O-CD (0.58%), ICG (0.20%), and TCPP (0.10%). Third, under hypoxic conditions, the P-CD with type I/II photodyanmic mechanism can still effectively produce $O_2^{\bullet-}$ (Fig. 4b, d). In contrast, no ROS generation of ICG

and TCPP can be detected under hypoxic conditions (Supplementary Fig. 14), which could be attributed to their O_2-depecdent type II photodyanmic mechanism. These results demonstrate that the D-π-A configured P-CDs possess the largest excited-state lifetime, highest ROS generation efficiency, and optimal hypoxic adaptability compared with the traditional CDs and commercial photosensitizers.

Theoretical calculation of CDs. We then performed the density functional theory (DFT) calculations to visually illustrate molecular orbital distributions, electron localization, and charge transfer pathways. We establish three kinds of sp^2 hybrid carbon molecules as simple CD models according to the theoretical models presented in Fig. 2h. Although the simplified CD model established in the theoretical calculations did not represent the true structure of these CDs, the relative comparison among the model enabled identification of trends and suggested explanations for the observed findings. Fig. 5a exhibits the spatial distributions of the HOMO (highest occupied molecular orbital) and LUMO (lowest unoccupied molecular orbital) for O-CD, M-CD, and P-CD. In the P-CD model, the HOMO is predominantly localized on the hydroxyl-rich region ("donor", D), whereas the LUMO is strongly concentrated on the pyridinic nitrogen-containing domain ("acceptor", A). This clear spatial separation of frontier orbitals directly demonstrates that, in the ground state of P-CD, the highest-energy electrons reside primarily in the donor moiety, while the lowest-energy vacant orbitals are located in the acceptor moiety, with both regions bridged by a conjugated π-system (carbon core). This configuration constitutes definitive evidence for a well-defined D-π-A architecture. Fig. 5b presents the calculated energy levels of the first singlet excited state (S_1) and the first triplet state (T_1), along with their respective singlet-triplet energy gaps

(ΔE_{ST}). Notably, P-CD exhibits a significantly smaller ΔE_{ST} (0.39 eV) compared to O-CD (0.82 eV) and M-CD (0.96 eV). Such a reduced energy gap facilitates efficient intersystem crossing (ISC) from the singlet to the long-lived triplet state. The theoretical calculation results consistent with the experiment results of ultralong phosphorescence lifetime of P-CD (36.32 ms), offering a mechanistic explanation for its excellent performance as a photosensitizer.

We then performed the surface electrostatic potential (ESP) analysis of O-CD, M-CD, and P-CD. As depicted in Fig. 5c, red regions represent the negative potential (electron-rich zones) and blue regions indicate positive potential (electron-deficient zones). In the P-CD model, a pronounced negative potential is observed in the hydroxyl-enriched region, contrasting sharply with the positive potential in the pyridinic nitrogen zone. This phenomenon confirms that hydroxyl groups act as the primary electron-donating center (D), while the pyridinic nitrogen serves as the electron-accepting center (A). These findings are further demonstrated by Fukui-DD function analysis (Fig. 5d), which reveals electrophilic features at the pyridinic nitrogen site with a high propensity for electron acceptance. In addition, the nucleophilic features over the hydroxyl and π-bridge regions was consistent with electron donation. These two complementary analyses confirm that the hydroxyl groups function as the strongest electron donor within the P-CD framework, serving as the driving force for intramolecular charge transfer. In summary, the DFT calculations provide comprehensive evidence from orbital distribution, energy-level alignment, and quantitative reactivity descriptors for the proposed D-π-A model. Orbital visualization confirms the spatial segregation of donor and acceptor units linked via a π-conjugated bridge. Energy-level calculations rationalize the experimentally observed long-lived triplet state. Electrostatic potential

and Fukui function analyses jointly establish the functional roles of the hydroxyl group as the dominant donor and pyridinic nitrogen as the key acceptor.

In vitro antitumor effectiveness evaluation of P-CD@MM. Having demonstrated the mild photothermal and D-π-A enhanced photodynamic effects of ultrasmall-sized P-CDs as superior type-I and type-II photosensitizers, we then prepared size-suitable and biomimetic P-CD@MM nanoparticles by harnessing tumor-associated MM as the nanocarrier to encapsulate P-CDs for enhancing both active and passive tumor-targeting capabilities, as previously reported in biomimetic nanomedicines.[64-66] It is noted that the encapsulation of M1-like MM can not only avoid immune clearance of free CDs for extended circulation time, but also promote the polarization of TAMs from protumoral M2-like phenotype to antitumoral M1-like phenotype. The loading efficiency and Zeta potential of P-CD@MM were determined to be about 20% and -30.8 ± 1.4 mV, respectively (Supplementary Fig. 15). The TEM images showed a size of ~ 150 nm suitable for affording the passive tumor-targeting capability via the EPR effect (Fig. 6a, b). As WB analysis revealed, there was the high expression level of M1-like macrophage specific proteins CD86 in P-CD@MM, while there was no significant band of CD206 as the M2-like macrophage specific protein, confirming the successful preparation of P-CD@MM with tumor-associated M1-like phenotype (Fig. 6c). The quantitative result of the expression levels of CD86 was added in Supplementary Fig. 16a. We then investigated the stability evaluation of P-CD@MM during storage. As depicted in Supplementary Fig. 16b, c, no significant change of size and Zeta potential of P-CD@MM were observed within 9 days, demonstrating the good colloidal stability of P-CD@MM. We then investigated the cellular uptake behaviors of P-CD@MM based on the intrinsic

fluorescence of P-CD. Confocal imaging of NIH-3T3 normal cells and 4T1 tumor cells exposed to P-CD@MM exhibited a much higher level of cell internalization in cancer cells, further clarifying the augmentation in tumor targeting levels of P-CDs through M1-like MM encapsulation (Fig. 6d). We then investigated the biocompatibility of P-CD@MM exposed to NIH-3T3 normal cells without photoirradiation through the MTT assay across a concentration range of 0-100 μg/mL. Even at the concentration up to 100 μg/mL, P-CD and P-CD@MM exhibited insignificant cytotoxicity to normal cells (Fig. 6e and Supplementary Fig. 17a), indicating their favorable biosafety profiles for potential applications in PDT.

To investigate the in vitro PDT efficacy of P-CD@MM, MTT assays were conducted under 808 nm laser irradiation (0.3 W/cm^2) for 5 minutes. As depicted in Fig. 6f, almost all 4T1 cells were killed by P-CD@MM +laser, suggesting the high in vitro antitumor efficacy of P-CD@MM under 5-min photoirradiation. The in vitro antitumor efficacy of MM-free P-CDs was also evaluated for comparison. Although a concentration-dependent cytotoxic profile of P-CD@MM similar to that of MM-free P-CDs, the real photoactive concentration of P-CDs in P-CD@MM was merely one-fifth of MM-free P-CDs owing to the only 20% loading efficiency. In other words, real antitumor efficacy of P-CD@MM + laser was five times higher than MM-free P-CD + laser owing to increased tumor targeting capability through MM coating, as confirmed by the cell imaging result (Supplementary Fig. 17b). We also performed the MTT assay to evaluate the relative cell viability of NIH-3T3 cells after being treated with P-CD@MM + L. As depicted in Supplementary Fig. 18, no significant decrease of the cell viability of NIH-3T3 cells was detected in the P-CD@MM + L group, which could be ascribed to the low cellular internalization efficiency of P-CD@MM in

normal cells.

To further investigate the therapeutic effects of P-CD@MM-mediated PDT, we conducted live/dead cell staining using Calcein-AM and PI as the probes of live and dead cells, respectively. The experimental groups were as follows: Group 1: PBS; Group 2: laser; Group 3: P-CD@MM; Group 4: P-CD@MM + laser. No dead cells can be detected in the control, laser alone, and P-CD@MM alone (Fig. 6g). In contrast, when the NIR laser was applied, the images presented in P-CD@MM + laser group exhibited no green fluorescence signal, verifying the excellent antitumor effectiveness of P-CD@MM-mediated PDT.

Notably, the photodynamic property of P-CDs was excellent (Supplementary Fig. 19, 20), while their photothermal property was of low-efficiency (only 32.2%). At the mild PTT conditions (0.3 W/cm^2) and a low P-CD concentration (<100 μg/mL), the rise in temperature was rather low (~10 °C) (Fig. 3i). Therefore, the excellent phototherapy effectiveness of P-CDs and P-CD@MM was not attributive to the mild PTT effect. To confirm the PDT effect as the main phototherapy mechanism, intracellular ROS levels under different treatment conditions were tested by ROS detection assay using DCFH-DA as the probe of ROS. This ROS-sensitive probe is oxidized by intracellular ROS to generate green fluorescence in cells. No significant ROS fluorescence signal was detected in groups 1-3 (Fig. 6h), implying no ROS generation in the absence of laser treatment or P-CD@MM. In contrast, strong green fluorescence was observed in the cytoplasm of cells in the P-CD@MM + laser group, confirming that ROS-mediated cell death was effectively induced by P-CD@MM based PDT. To further investigate the mechanisms of cell death, we analyzed apoptosis levels using Annexin V-FITC and PI staining combined with flow cytometry. As shown

in Supplementary Fig. 21, significant apoptosis of 4T1 cells was detected in the P-CD + laser and P-CD@MM + laser groups. Extensive studies have demonstrated that PDT can induce tumor cell apoptosis while PTT can induce tumor cell necrosis.[2] Collectively, these results indicated that P-CD@MM exhibits excellent antitumor efficacy in vitro by PDT induced cell apoptosis.

P-CD@MM-mediated PDT induces ICD and M1-like polarization. After confirming that P-CD@MM induced cancer cell apoptosis through PDT, we then investigated the ROS-triggered ICD effect to evaluate the tumor-specific immune responses. It is well known that the generation of ROS in tumors could trigger the exposure of CRT, secretion of HMGB1, and leakage of ATP.[12,67] On this basis, we initially evaluated CRT exposure level on 4T1 cells through immunofluorescence staining. Notable CRT signals were observed in both the P-CD + laser group and the P-CD@MM + laser group, indicating a translocation of CRT from the endoplasmic reticulum to the cell surface (Fig. 7a). Subsequently, ELISA assay and ATP detection kit were utilized to assess the HMGB1 and APT levels, respectively. The concentration of HMGB1 released from 4T1 cells treated with P-CD@MM + laser was measured at 30.7 ± 1.6 μg/L (Fig. 7b), significantly surpassing that observed in other groups. This finding suggests that the PDT effects of P-CD and P-CD@MM enhance HMGB1 release, which may trigger pro-inflammatory cytokine secretion and subsequently stimulate DC maturation. In addition, ATP levels were markedly diminished in both the P-CD + laser group and the P-CD@MM + laser group (Fig. 7c). Collectively, these results indicate that P-CD@MM can induce an enhanced ICD effect via PDT.

Having demonstrated that P-CD@MM can induce ICD and enhance the secretion of DAMPs, we proceeded to investigate DAMP-activated DC maturation and the subsequent immune

responses. BMDCs were isolated from the tibias and femurs of BALB/c mice. 4T1 cells were pretreated with P-CD@MM + laser, after which the supernatant containing DAMPs was collected to stimulate BMDCs (Fig. 7d). The expression ratios of mature DC markers $CD80^+$ and $CD86^+$ in the P-CD@MM + laser group were measured at 15.7 ± 0.8%, significantly higher than those observed in the other groups (Fig. 7e, f). These results indicate that P-CD@MM-mediated ICD effectively triggers BMDC maturation, potentially activating a systemic immune response capable of targeting tumor cells for destruction.

It is well known that macrophages can switch between their main phenotypes, M1-like and M2-like, depending on cytokines or pathogenic signals.[68] M1-like macrophages are known for their pro-inflammatory, immunogenic, and anti-tumoral features, whereas M2-like macrophages are recognized for their anti-inflammatory, tolerogenic, and pro-tumoral traits.[68] Within the TME, most macrophages showcase the M2-like phenotype, prompting the exploration of reprogramming M2-like to M1-like macrophages as a strategy for cancer therapy. Increased ROS levels have been shown to significantly induce TAMs to switch from the pro-tumoral M2-like to the anti-tumoral M1-like phenotype, thus reversing the immunosuppressive TME. Based on this situation, we utilized commercialized RAW 264.7 cells and BMDMs as model systems to evaluate the ability of P-CD@MM + laser to reprogram macrophages. Similar to the evaluation of DC maturation, 4T1 cells were pre-treated with P-CD@MM + laser, and the supernatant was collected to stimulate RAW 264.7 cells (M0-like) (Supplementary Fig. 22a). A significant increase of $CD86^+CD206^-$ TAMs (M1-like) was observed in P-CD@MM + laser group, suggesting that the treatment of P-CD@MM plus laser irradiation can promote the polarization of TAMs from M2-like to M1-like

phenotype (Supplementary Fig. 22b, c). For BMDMs, we first pre-polarized TAMs with M0-like phenotype to M2-like phenotype. After treatment with P-CD@MM + laser, a pronounced shift from the M2-like to M1-like phenotype was observed compared to the other groups (Fig. 7g). Specifically, $CD86^{+}CD206^{-}$ TAMs (M1-like) increased from 6.3 ± 0.6% to 36.0 ± 1.0%, while $CD86^{-}CD206^{+}$ TAMs (M2-like) decreased from 41.7 ± 0.8% to 8.4 ± 0.8% (Fig. 7h, i). A similar M2-like to M1-like polarization was also observed in RAW 264.7 cells (M2-like) after being treated with P-CD@MM + laser (Supplementary Fig. 23). We also noted that the M1-like macrophage membrane can inherently promote M1-like polarization. On this basis, we explored the interaction mechanism between M1-like macrophage membrane and TAMs. As shown in Supplementary Fig. 24, compared with the Control, Laser, and P-CD groups without M1-like macrophage membrane, P-CD@MM treatment alone significantly increased the expression levels of phosphorylated NF-κB p65 (p-NF-κB p65) and phosphorylated STAT1 (p-STAT1) in TAMs. This enhancement effect was further amplified after adding laser irradiation (P-CD@MM + Laser). The results provide direct molecular evidence that the M1-like macrophage membrane is not an inert carrier, but interacts with TAMs through its surface retained ligands, actively activating the core signaling pathways (NF-κB and STAT1) that drive M1-like polarization, thereby reprogramming the pro-tumoral M2-like phenotype to the anti-tumoral M1-like phenotype. These findings confirm that P-CD@MM-triggered ICD can reprogram TAMs from the M2-like to M1-like phenotype, effectively reversing the immunosuppressive TME.

In vivo antitumor effectiveness evaluation. We established a unilateral tumor model to determine the time-dependent accumulation level of intravenously injected P-CD@MM in tumor

sites and the optimal time window for PDT by in vivo imaging (Fig. 8a). For comparison, free P-CDs without MM encapsulation was also evaluated by the in vivo imaging. As presented in the Fig. 8b, c, MM-free P-CDs exhibited a rather low accumulation level in the tumor sites at 24 h post-injection owing to rapid metabolization out of the body, while P-CD@MM showed a high level of accumulation in the tumor sites at 12-48 h (Supplementary Fig. 25), clearly confirming the crucial role of MM encapsulation in enhancing tumor targeting capability and elongating blood circulation time. The optimal time for laser irradiation was thus determined to be at 24 h post-injection since at this time point the strongest fluorescent signal of P-CDs was observed. This tumor targeting distribution of P-CD@MM was also revealed by the ex vivo imaging (Fig. 8d and Supplementary Fig. 26). For MM-free P-CDs, following intravenous administration, P-CD predominantly accumulated in the liver of mice (Supplementary Fig. 27), which was consistent with the in vivo NIR imaging results (Fig. 8b), suggesting the low accumulation level of P-CDs in tumors. We also investigated the in vivo pharmacokinetics of MM-free P-CDs and MM-encapsulated P-CDs by measuring plasma concentration-time profiles. As depicted in Supplementary Fig. 28a, a typical double-compartment pharmacokinetic behavior of P-CD and P-CD@MM can be detected. The elimination half-life ($t_{1/2}$) of P-CD and P-CD@MM was determined to be 0.9 ± 0.1 h and 10.6 ± 1.1 h, respectively (Supplementary Fig. 28b). The prolonged half-life of P-CD after coating of MM illustrates that P-CD@MM possesses longer circulation time compared with the pristine P-CD, enabling the accumulation of P-CD@MM in tumors at high levels.

We also monitored a PTT induced moderate rise in local temperature at the tumor location

exposed to 808 nm NIR laser (0.3 W/cm^2) using an IR thermal camera. In Fig. 8e, the tumor temperature treated with P-CD@MM under 10 min NIR irradiation slowly reached 49.1 °C, which was insufficient for tumor thermal ablation but could relieve tumor hypoxia. Generally, PDT efficacy is compromised due to its oxygen dependent nature as the continuous oxygen consumption during the treatment prohibits further ROS generation and induces a hypoxic environment in tumor to trigger the hypoxia-inducing factor-1α (HIF-1α)-mediated signaling cascade that could desensitize tumors to PDT and even provoke tumor invasion and metastasis. Therefore, the exploration of the moderate PTT effect on alleviation of hypoxia in TME is of great importance for improving PDT efficiency and safety. To confirm this effect, we conducted the immunofluorescence hypoxia staining assay to verify the alleviation of hypoxia in the tumor tissue induced by mild NIR PTT. As expected, the hypoxia signal of tumor slices in P-CD@MM plus NIR laser group was less than that of the control group, only NIR laser group, and only P-CD@MM group (Fig. 8f), illustrating that the severe tumor hypoxia was alleviated by the mild PTT.

According to these pre-examinations, we finally designed the treatment protocol for PTT-assisted PDT, by which single dosing and single irradiation under 808 nm at low power density (0.3 W/cm^2) for 10 min irradiation were administrated (Fig. 7a). To evaluate the in vivo antitumor efficacy of P-CD@MM by photoimmunotherapy, we established a bilateral tumor model and examined the inhibitory rates of local tumors and distant metastases by measuring the volumes of primary and distant tumors. As shown in Fig. 8g, h, P-CD and P-CD@MM alone showed limited antitumor effects in vivo. However, when combined with 808 nm laser irradiation, tumor growth

was significantly inhibited. Notably, the P-CD@MM + laser treatment achieved complete eradication of the primary tumor, suggesting that P-CD@MM-mediated PDT can achieve optimal therapeutic outcomes. Furthermore, the volume of distant tumors also exhibited a significant inhibiting effect after treatment of P-CD@MM + laser, indicating that P-CD@MM-mediated PDT also possessed antitumor immune response. Mice in the P-CD@MM + laser group survived for over 50 days, whereas mice in the control group survived only up to 26 days (Supplementary Fig. 29a). This phenomenon indicates that P-CD@MM-mediated PDT can induce a strong immune response for synergistic therapy, thereby prolonging the survival of mice. We also investigated the influence of laser irradiation parameters on the therapeutic effects of P-CD@MM-mediated combination therapy. To evaluate the impact of irradiation spatial coverage and duration, we evaluated tumor growth under different light spot sizes (d = 0.4 cm, insufficient to fully cover the tumor; d = 0.8 cm, slightly larger than the tumor; d = 1.2 cm, substantially exceeding tumor dimensions) at a fixed power density of 0.3 W/cm^2 and irradiation time of 10 min. Additionally, under the same power density and a spot size of 0.8 cm, we examined the effects of varied irradiation durations (0, 5, 10, and 15 min) on therapeutic outcomes. As shown in Supplementary Fig. 30, both insufficient irradiation area and suboptimal exposure time failed to achieve complete tumor growth inhibition. The optimal therapeutic efficacy was observed at a power density of 0.3 W/cm^2, a spot diameter of 0.8 cm, and an irradiation time of 10 min. While longer irradiation times or larger spot sizes also yielded strong antitumor effects, they may increase the risk of collateral damage to surrounding healthy tissues due to excessive energy deposition. ROS staining of tumor tissues showed the highest ROS signals in the P-CD@MM + laser group (Fig. 8i). H&E and

TUNEL staining images indicated apoptosis or necrosis in both primary and distant tumors in the P-CD@MM + laser group (Supplementary Fig. 31, 32). These findings suggest that P-CD@MM-mediated PDT induces a strong immune response, leading to severe tumor cell apoptosis/necrosis.

In vivo photoimmunotherapy antitumor mechanism. As indicated by in vitro cellular experiments, P-CD@MM-mediated PDT can effectively trigger ICD, promote DC maturation, and reverse the immunosuppressive TME. To further elucidate the synergistic therapy of PDT and immunotherapy, we investigated the immune responses induced by ICD at the solid tumor level. We detected the levels of pro-inflammatory cytokines in mice including interleukin-6 (IL-6), interferon-γ (IFN-γ), and tumor necrosis factor-α (TNF-α) using ELISA assay. As shown in Supplementary Fig. 33, the levels of IL-6, IFN-γ, and TNF-α in P-CD@MM + laser group were significantly higher than those in other groups. These results suggest that P-CD@MM-mediated PDT can activate the immune response in vivo by releasing tumor-associated antigen, thus inducing ICD and M1-like polarization. Then, immunofluorescence staining for CRT expression in tumor tissues showed the most evident green fluorescence in the P-CD@MM + laser group (Fig. 9a). ELISA and an ATP detection kit were used to measure the other two ICD markers, revealing significantly higher HMGB1 and ATP levels in tumor tissues of the P-CD@MM + laser group than in other groups (Supplementary Fig. 34), further confirming marked ICD induction by P-CD@MM-mediated PDT.

Subsequently, tumor-draining lymph nodes, spleens, and tumor tissues were collected from mice in each group for flow cytometric analysis of immune cell populations. Analysis of DCs in tumor-draining lymph nodes revealed a significantly higher proportion of $CD80^+CD86^+$ DCs in the P-

CD@MM + laser group (Supplementary Fig. 35). This confirmed that P-CD@MM + laser effectively promoted DC maturation, attributed to ROS induced ICD and M1-like polarization of TAMs. We also noted that the treatment of P-CD@MM + laser induced the higher DC maturation level compared with the treatment of P-CD + laser, which could be ascribed to the stronger tumor targeting and enrichment capabilities of P-CD after encapsulating by MM. The higher local tumor concentration means that a stronger photodynamic effect can be generated under NIR laser irradiation, thereby triggering stronger ICD to activate antitumor immune response. After P-CD@MM + laser treatment, the proportions of $CD8^+CD3^+$ T cells and $CD4^+CD3^+$ T cells in mouse spleens increased significantly from 1.3 ± 0.3% to 16.0 ± 0.7% and from 1.6 ± 0.3% to 18.0 ± 0.9%, respectively (Supplementary Fig. 36). Further assessment of T cell activation in tumor tissues showed that the proportions of $CD8^+CD3^+$ T cells and $CD4^+CD3^+$ T cells in both primary and distant tumors were significantly higher in the P-CD@MM + Laser group compared with the other groups (Fig. 9b and Supplementary Fig. 37). These results clearly indicate that P-CD@MM effectively triggered immune responses through PDT. As the TME is enriched with M2-like TAMs that promote tumor progression, we used flow cytometry to analyze macrophage polarization in primary and distant tumors following various treatments. As shown in Fig. 9c and Supplementary Fig. 38, in primary tumors treated with P-CD@MM + laser, M2-like TAMs ($CD206^+F4/80^+$) were markedly reduced, while M1-like TAMs ($CD86^+F4/80^+$), which have anti-tumor properties, were significantly increased. Similar results were observed in distant tumors (Supplementary Fig. 39). These findings forcefully indicate that the photosensitizer P-CD@MM triggered tumor-specific ICD, reprogramed TAMs from M2-like to M1-like phenotype, promoted DC maturation, and

activated T cells.

To demonstrate the pivotal role of P-CD-mediated phototherapy in activation of antitumor immune response, we employed the M0-like phenotype RAW264.7 macrophage membrane as an empty cell membrane to encapsulate P-CD (P-CD@EM). As depicted in Supplementary Fig. 40a, b, no significant antitumor effectiveness of P-CD@EM alone can be detected, suggesting the encapsulation of P-CD in EM did not trigger the antitumor immune response. For comparison, a slight inhibition effect on the growth of primary and distant tumors was observed in the P-CD@MM, demonstrating that cell membrane derived from M1-like phenotype macrophage can activate a certain antitumor immune response. We also noted that the treatment of P-CD@EM + L can inhibit the tumor growth, which could be attributed to the P-CD-induced PDT. However, the stronger antitumor effectiveness can be detected in the P-CD@MM + L group, which was superior to that in the P-CD@EM + L group, illustrating that the antitumor immune response of P-CD-mediated PDT could be further enhanced by the encapsulation of P-CD in MM rather than in EM. Immunological analyses revealed that P-CD@EM alone did not elicit antitumor immune responses. P-CD@EM failed to promote DC maturation, induce T cell infiltration, or drive polarization of macrophages from M2-like phenotype to M1-like phenotype (Supplementary Fig. 40c-n). In contrast, P-CD@MM exhibited a certain immunostimulatory activity, implying that the encapsulation of P-CD in MM can endow immunoregulation functions to P-CD. We also noted that P-CD@EM combined with laser irradiation triggered strong immunological activation, demonstrating that P-CD-mediated PDT served as the essential core component for the activation of antitumor immune responses.

Long-term immunological memory evaluation. It is well known that the immune-memory response represents an essential aspect of adaptive immunity, enabling the immune system to remember previous pathogen invasions and provide long-lasting immunity. On this basis, we constructed a re-challenging tumor model to evaluate the long-term immune memory effect induced by P-CD@MM-mediated combination therapy (Fig. 10a). After the first tumor was cured by P-CD@MM + L, we inoculated 4T1 cells on the opposite axilla of mice to fabricate the re-challenging tumor model. No injection of P-CD@MM and no irradiation of 808 nm laser were performed. For comparison, five healthy mice were also inoculated with 4T1 cells as the control group. We then monitored the change of tumor volume and performed the immunological analysis. As depicted in Fig. 10b, c, the significantly inhibited tumor growth was detected in the P-CD@MM + L group, while rapid tumor growth was observed in the control group, suggesting that the treatment of P-CD@MM + L can induce an effective immune memory response for the long-term protection against tumor recurrence of mice. During the treatment period, no loss of weight can be found in the control and P-CD@MM + L groups (Fig. 10d), demonstrating that the treatment of P-CD@MM + L possessed good biosafety. Subsequently, we investigated the T cell activation level in each group to clarify the immune memory response. As presented in Fig. 10e, the higher expression levels of CD4 and CD8 were detected in the P-CD@MM + L group compared with the control group. Specifically, the proportion of $CD3^+CD8^+$ and $CD3^+CD4^+$ T cells in the P-CD@MM + L group were measured to be approximately 24.5 ± 1.4% and 22.2 ± 1.3%, respectively (Fig. 10f, g), which was much higher than those in the control group (3.9 ± 0.5% for $CD3^+CD8^+$ and 2.9 ± 0.7% for $CD3^+CD4^+$). Additionally, the proportion of effector memory T cells

($CD3^+CD8^+CD44^+CD62L^-$) in the spleens of both groups was analyzed. As depicted in Fig. 10h, i, in the P-CD@MM + L group, a significantly higher proportion of effector memory T cells (34.3 ± 1.4%) was observed, which was four times greater than that in the control group (8.6 ± 0.9%). Collectively, these results indicate that the administration of P-CD@MM + L induces a long-lasting immune memory response, which can enable the immune system to remember previous pathogen invasions and provide long-lasting immunity to prevent the reappearance of tumors.

Finally, we assessed the biological safety of the P-CD@MM + laser treatment modality. During the treatment period, no significant weight loss was observed in any group compared to normal mice (Supplementary Fig. 29b). We then explored the in vivo biodistribution and excretion pathways of P-CD@MM. Supplementary Fig. 41a showed that P-CD@MM mainly accumulated in the liver at 24 h post-injection, which was attributed to the capture of the reticuloendothelial system. Importantly, no obvious P-CD signal was observed in these organs after 14 days, indicating that P-CD@MM has been almost completely cleared. To study the excretion pathways, the concentrations of P-CD in urine and feces were also measured. The results indicated that P-CD@MM was mainly excreted from the mice through the liver and kidney. We also noted that no P-CD signal can be detected after 14 days (Supplementary Fig. 41b), suggesting the complete clearance of P-CD@MM. The major organs of mice subjected to different treatments were analyzed via H&E staining. The results reveal no significant differences compared to the control group, with no evident damage observed (Supplementary Fig. 42). Furthermore, blood biochemical analysis (Supplementary Fig. 43a) and hematological parameters (Supplementary Fig. 43b) demonstrated that all blood indices in treated mice remained within the normal physiological

range. We also performed the hemolysis test of P-CD@MM. As shown in Supplementary Fig. 44, hemolysis assays confirmed the good blood compatibility of P-CD@MM, with a hemolysis rate below 5% at concentration of 100 μg/mL. Collectively, these results substantiate the good biocompatibility and biosafety profile of P-CD@MM-mediated PDT, thereby supporting its potential utility in antitumor therapy.

Discussion

In the development of clinically translatable CD-based photodynamic systems for hypoxia regulated photo-immunotherapy, one challenging issue confronted with us is a lack of precise regulation strategies for engineering CDs as NIR-responsive, type-I and type-II dual photosensitizers with tunability in narrow bandgap, ultralong excited state lifetime, NIR photothermal conversion, and NIR photodynamic generation of both $^1O_2$ and $O_2^{\bullet-}$. Herein, we developed a one-step, solvothermal, binary precursor-engineering strategy for precise regulation of photothermal and photodynamic properties of CDs with the distinct D-π-A configuration and ultralong-lived triplet states for photo-immunotherapy against hypoxic tumors within the phototherapeutic window with minimal adverse effects. Mechanically, an intramolecular CT state with a ultralong lifetime mediated by the D-π-A structure enables the enhanced PDT performance. Importantly, the hypoxia condition was substantially relieved by mild PTT + PDT, as evidenced by immunofluorescence staining of HIF-1α in tumor. We further designed M1-like macrophage-derived cell membrane-camouflaged P-CD to realize preferential tumor accumulation while guarantee rapid systemic clearance. On the one hand, the encapsulation of P-CD in MM can

prevent the rapid clearance of CDs, actively targeting the tumor tissue to improve the tumor accumulation level of P-CDs. On the other hand, MM-encapsulated P-CDs can enhance reversion of the immunosuppressive TME and realize the cascade amplification of antitumor immune response through triggering ICD and reprogramming TAMs into antitumoral M1-like phenotype. Collectively, satisfactory therapeutic outcomes for primary and distant tumors were achieved by P-CD@MM-mediated precise PDT-enhanced immunotherapy at low laser power density of 0.30 W/cm^2 (808 nm). Our work highlights the crucial roles of D-π-A sensitization of CDs in boosting NIR-photoimmunotherapy by triplet state stabilization, surface charge transfer, and mild photothermal relief of hypoxia.

Although we demonstrated the D-π-A structure design and controllable synthetic strategy for CD-based type-I/II photo-systems, there are still some questions that need to be addressed before clinical translation.

First, the formation mechanism of CDs synthesized from the co-precursor systems was unclear. To date, the exact formation mechanism of all reported CDs under hydrothermal or solvothermal conditions has not been elucidated clearly owing to a lack of in situ, real-time tools for direct observation of evolution processes of organic molecules as precursors. In our cases, for the synthesis of O-CDs, M-CDs, and P-CDs from the relatively complex binary co-precursor systems, the CD formation may involve multiple steps, such as initial fusion/polymerization, partial decomposition, and final graphitization under the low-temperature (150 °C), short-time (4 h) solvothermal synthesis conditions. Besides the binary precursors, the alcohol solvent also participated in these reaction processes because phenolic hydroxyl at high content was

incorporated into the CDs. Therefore, we speculated that these molecules could be initially integrated through a hydrogen bond network formed among molecules of ICG, phenylenediamine isomers, and alcohol for driving subsequent solvothermal reactions.

Second, which component serves as the primary precursor for the carbon core? We proposed that the core of CDs should be more graphitized than the heteroatom functional edge of CDs. Considering that M-CDs and P-CDs from the binary combination of ICG + MPD, ICG + PPD have a much higher graphitization level than CDs from ICG only, the phenylenediamine component may serve as the primary precursor for construction of the carbon core as well as N-heteroatom modification at the edge.

Third, how to define ICG's role in the construction of the D-π-A system? The ICG precursor indirectly provided D-π-A sensitized CDs with the D-type modification, majorly because ICG as electrophilic centers at positively charged N sites can react with nucleophilic alcohol, leading to the electron-rich functionalization of P-CDs with rich -OH groups as donors (7.92 at.%). Although the ICG precursor also provided P-CDs with electron-deficient modification by inclusion of an acceptor $-SO_3^-$/$-SO_3H$, but there was a much lower doping level for the S-based acceptor (1.80 at.%) than the N-based acceptor (pyridinic N 8.68 at.%) from another precursor (PPD). In other words, the A-type modification in P-CDs was largely ascribed to PPD rather than ICG.

Finally, how to understand the impact of the D-π-A configuration on photodynamic performance? the D-π-A system in the type-I/II dual photosensitizer (P-CDs) was different from the previously reported D-π-A system in the type-II photosensitizer (termed p-n-CDs) with an intermolecular p-n junction.[50] The p-n-CDs were synthesized by microwave-assisted co-treatment of ICG and BPEI

(branched polyethylenimine) as dual precursors. In the p-n-CDs, the D-π-A configuration was composed of $-SO_3^-$/$-SO_3H$ groups as the electron acceptor (A) and pyrrolic N primarily as the electron donor (D). Notably, the p-n-CDs exhibited no activity in $O_2^{\bullet-}$ generation under ultrasonic or photo-irradiation (Supplementary Fig. 45), suggesting that the type-I mechanism was deactivated in the pyrrolic N/$-SO_3H$ configuration with a high S doping level (8.1 at.%). We speculated that $-SO_3^-$/$-SO_3H$ groups enriched in p-n-CDs with the strong electron-withdrawing capability may block photoinduced electron transfer from CDs to molecular O_2, leading to ineffective generation of $O_2^{\bullet-}$. In the D-π-A system with high photosensitization activity in both type-I and type-II, however, the electron withdrawing effect by the strong S-based acceptor was greatly weakened owing to the low S doping level (1.80 at.%), and the high-content pyridinic N (8.68 at.%) as a weak N-based acceptor plays a crucial role in the D-π-A system for optimization of desirable photodynamic types, activation wavelength, and ultra-stable triplets.

Collectively, to overcome such limitations as short excited-state lifetime (ns) and absence of NIR-photodynamic activity of common CDs, and deactivated type-I mechanism in the type-II D-π-A photo-system, we designed the type-I/II D-π-A NIR-photo-system by changing the chemical components of the D-π-A configuration, i.e. using electron-rich phenolic hydroxyl groups as donors and pyridine N with weak electron withdrawing ability as acceptors. This work demonstrates that it is possible to improve the electron donating and withdrawing ability of long-lived excited states within the D-π-A framework to activate the type-I photodynamic mechanism under NIR irradiation.

Methods

Ethical statement

All animal experiments were approved by the Animal Protection and Use Committee of Shanghai University (SYXK2019-0020). All mice were housed in an animal facility under constant environmental conditions (room temperature, 22 ± 1 °C, relative humidity, 40-70% and a 12 h light-dark cycle). The experiment was designed without considering the sex of the animals. Both male and female mice were used for the in vivo experiments. Maximal tumor sizes were within permission limits (⩽1200 mm^3). Tumor volume was calculated using the formula: Volume = (Length × Width × Width)/2.

Synthesis of P-CDs, M-CDs and O-CDs

For the preparation of P-CDs, ICG (5 mg) (Aladdin, China) and p-phenylenediamine (10 mg) (Aladdin, China) were dissolved in ethanol (10 mL) (Sinopharm Chemical Reagent Co., Ltd., China). The solution was transferred into a 25 mL Teflon-lined autoclave and reacted at 150 °C for 4 h. The reactor is then cooled to room temperature. Large particles were removed by 0.22 μm membrane, followed by dialysis for 36 h using a dialysis bag. The preparation methods for M-CDs and O-CDs were analogous to that of P-CDs, with the exception that meta-phenylenediamine (Aladdin, China) was used as the precursor for M-CDs and ortho-phenylenediamine (Aladdin, China) for O-CDs.

Synthesis of M1-like macrophage cell membrane

RAW264.7 cells (Haixing Biosciences, TCM-C766-UD, China) were co-cultured with LPS (1 μg/mL) (Beyotime, China) for 24 h to obtain M1-like macrophages. The cells were resuspended

in lysis buffer (Beyotime, China) and sonicated on ice (80 W, 20 min). The solution was centrifuged at 4 °C for 30 min, and the supernatant was collected to obtain macrophage membranes (MM). The M0-like macrophage membranes were obtained from RAW 264.7 cells using the same method.

Synthesis of P-CD@MM

The P-CD aqueous solution (1 mL, 0.5 mg/mL) and the M1-like macrophage cell membrane (1 mL, 1 mg/mL) were separately transferred to syringes and successively extruded through a 100 nm water-phase filter using an extruder to form P-CD@MM. Finally, the P-CD@MM solution was centrifuged to remove unbound P-CD. We also employed the M0-like phenotype RAW264.7 macrophage membrane as an empty cell membrane (EM) to encapsulate P-CD (P-CD@EM) using the same method.

Characterization

TEM images of O-CD, M-CD, and P-CD were acquired using a JEOL JEM-2100F microscope. XPS, FT-IR, and Raman spectra of CDs were obtained with a Kratos Axis Ultra DLD spectrometer, Nicolet AVATAR 370 spectrophotometer, and Renishaw in plus laser Raman spectrometer, respectively. NMR of these CDs were obtained by Bruker Avance NEO 500MHz. Phosphorescence lifetimes were determined via an Edinburgh Instruments FLS 1000 spectrofluorometer. UV-vis-NIR absorption and fluorescence spectra were detected by Agilent Cary 5000 and Hitachi 7000 spectrophotometer, respectively.

Photothermal performance measurements

The photothermal properties of P-CD were studied by irradiating centrifuge tubes containing P-

CD solutions (0-0.3 mg/mL, 1 mL) for 5 min. The temperature of the P-CD solution was measured every 30 s by Fluke infrared thermal imager. The photothermal conversion efficiency of P-CD was calculated according to the following four formula.

$$\eta = \frac{hA(T_{max}-T_{surr})-Q_{Dis}}{I(1-10^{-A_\lambda})} \quad (1)$$

$$\theta = \frac{T-T_{surr}}{T_{max}-T_{surr}} \quad (2)$$

$$\tau_s = \frac{m_D C_D}{hA} \quad (3)$$

$$t = -\tau(\ln\theta) \quad (4)$$

Photodynamic performance measurements

The generation efficiency of ROS was recorded by measuring the absorbance of DPBF (Aladdin, China) at 418 nm after irradiating the mixture of 30 μg DPBF and P-CD (0.1 mg/mL) with an 808 nm laser (0.3 W/cm^2) for 10 min.

The generation efficiency of $O_2^{\bullet-}$ was determined by recording the green fluorescence of DHR123 (Aladdin, China) at 525 nm after irradiating the mixture of 10 μM DHR123 and P-CD (0.1 mg/mL) under the same laser and time conditions. To detect $O_2^{\bullet-}$ under hypoxia, a similar method was performed except that the mixed solution was bubbled with N_2 for 15 min before exposure to 808 nm laser.

For the ESR measurements of $^1O_2$ and $O_2^{\bullet-}$, TEMP (20 μL) (Sigma) and DMPO (10 μL) (Sigma) were respectively added to the P-CD solution (0.1 mg/mL). The ESR spectrometer is used to detect $^1O_2$ and $O_2^{\bullet-}$ produced by P-CD for 5 min under 808 nm laser irradiation (0.3 W/cm^2). The $^1O_2$ and $O_2^{\bullet-}$ generation efficiencies of O-CD and M-CD were also obtained under the same conditions.

We then utilized an indirect method to determine the quantum yield (QY) of $^1O_2$ produced by

P-CD. Free ICG solution was used as a comparison standard with a $^1O_2$ QY of 0.2%. The $^1O_2$ QY of the P-CD solution was calculated using the following Eq. (1)

$$\Phi_{sample} = \Phi_{ICG}\left(\frac{K_{sample}}{K_{ICG}}\right)\left(\frac{A_{ICG}}{A_{sample}}\right) \qquad (1)$$

Where K_{sample} and K_{ICG} represent the decomposition rate constants of DPBF by P-CD and free ICG solution, respectively. A_{ICG} and A_{sample} are the integral areas of the optical absorption bands between 808 and 810 nm by P-CD and free ICG solution, respectively.

DFT details

All quantum chemical calculations were performed using the Gaussian 16 program package. The geometries of all molecules were optimized within the framework of DFT using the B3LYP functional in combination with the def2-SVP basis set, without imposing any symmetry constraints. Vibrational frequency analyses were carried out at the same level of theory to confirm that all optimized structures correspond to true minimum on the potential energy surface, with no imaginary frequencies. Based on the optimized ground-state geometries, the energy and spatial distributions of the frontier molecular orbitals, including HOMO and LUMO, were calculated to analyze the intramolecular charge transfer characteristics. Excited-state properties were investigated using time-dependent DFT (TD-DFT) to obtain the low-lying singlet and triplet excited-state energy levels. The resulting data were used to construct excited-state energy level diagrams, providing insight into the fluorescence and phosphorescence transition processes. Molecular electrostatic potential (ESP) surface analyses were performed on the optimized ground-state structures. The electrostatic potential distributions were calculated and visualized using the Multiwfn program to elucidate the surface charge distribution characteristics of the molecules. In

addition, Fukui function analyses were carried out to identify potential reactive sites and regions with high electronic responsiveness, thereby assisting in understanding charge redistribution behaviors in the excited states. All molecular orbital isosurfaces and electron density-related images were visualized using VMD and Gauss View.

MTT assay

To evaluate the cytotoxicity of M-CD, P-CD, and P-CD@MM on NIH-3T3 (Haixing Biosciences, TCM-C752, China) and 4T1 cells (Haixing Biosciences, TCM-C705, China), NIH-3T3 or 4T1 cells were first inoculated and cultured in 96-well plates, and then incubated with different concentrations of M-CD, P-CD, and P-CD@MM for 24 h. The survival rate was detected by standard MTT assay. After incubating with M-CD, P-CD and P-CD@MM for 4 h, NIH-3T3 or 4T1 cells were irradiated with 808 nm laser (0.3 W/cm^2) for 5 min, and then incubated for another 24 h.

Live/dead cell staining, ROS detection, $O_2^{\bullet-}$ detection, and apoptosis assay

4T1 cells were seeded in 6-well plates at 2×10^5 cells per well. They were treated with PBS, 808 nm laser (0.3 W/cm^2), P-CD, P-CD@MM, P-CD + laser, or P-CD@MM + laser. After 24 h of incubation, cells were stained with Calcein-AM (488 nm) and PI (561 nm) (Beyotime, China), and live/dead cell fluorescence images were captured via fluorescence microscopy (Olympus, Japan). For ROS staining, the cells were stained with DCFH-DA and DAPI (Beyotime, China). Confocal images were captured using a confocal microscope (Olympus, Japan) to assess intracellular ROS levels. For $O_2^{\bullet-}$ staining, replace the culture medium with DHE staining solution (Beyotime, China) and incubate for 30 min. Then, the cells were exposed to an 808 nm (0.3 W/cm^2)

laser for 5 min and imaged under a confocal microscope. For apoptosis analysis, cells were collected by centrifugation (300 × g, 5 min) and apoptosis was detected using an Annexin V-FITC/PI kit (Dojindo, Japan) via flow cytometry (Beckman, CytoFLEX LX).

In vitro ICD marker detection

4T1 cells were seeded in a 6-well plate at 2×10^5 cells per well and treated with control, laser (808 nm, 0.3 W/cm^2), P-CD, P-CD@MM, P-CD + laser, or P-CD@MM + laser. The intracellular ATP and HMGB1 levels were measured using an ATP kit (Beyotime, China) and an HMGB1 kit (Beyotime, China), respectively. CRT was detected using confocal microscope after 4T1 cells were incubated with calreticulin rabbit mAb (Beyotime, AF1666, 1:500) and FITC-conjugated goat-anti-rabbit IgG (Beyotime, A0562, 1:500).

In vitro evaluation of DC maturation

BMDCs were extracted from the femurs and tibias of 5-week-old Balb/c mice and cultured for 7 days in 1640 medium with GM-CSF (20 ng/mL) and IL-4 (10 ng/mL) (Beyotime, China). Then, BMDCs were co-incubated for 24 h with 4T1 cell suspensions that had been treated with control, laser (808 nm, 0.3 W/cm^2), P-CD, P-CD@MM, P-CD + laser, or P-CD@MM + laser. BMDCs were collected and stained with anti-CD11c-FITC (Biolegend, 117306, 1:200), anti-CD80-PE (Biolegend, 104707, 1:200), and anti-CD86-APC (Biolegend, 105011, 1:200), then analyzed by flow cytometry.

In vitro macrophage polarization evaluation

RAW264.7 macrophages (M0-like phenotype) were first cultured in a 6-well plate for 24 h and then treated with IL-4 (20 ng/mL) to differentiate into M2-like phenotype. These cells were treated

with PBS, laser (808 nm, 0.3 W/cm^2), P-CD, P-CD@MM, P-CD + laser, or P-CD@MM + laser. Finally, these cells were collected and analyzed by flow cytometry after staining by anti-F4/80-APC (Biolegend, 123116, 1:200), anti-CD86-PE (Biolegend, 159204, 1:200), and anti-CD206-FITC (Biolegend, 141704, 1:200). We also utilized BMDMs to evaluate the polarization effect of P-CD@MM-mediated combination therapy. BMDMs were extracted from the tibiae and femurs of 5-week-old Balb/c mice and then treated with M-CSF and IL-4 to obtain M2-like phenotype.

Western blot analysis

Proteins in macrophage lysates, macrophage membranes, and P-CD@MM were characterized by Western blot analysis. Cells were lysed in RIPA buffer containing 1% PMSF. Protein concentrations were measured using the BCA method. Twenty micrograms of protein were separated by SDS-PAGE and transferred to a PVDF membrane, which was blocked with 5% skim milk at room temperature for 1 h and washed with TBST. The membrane was incubated overnight at 4 ^{o}C with primary antibodies: anti-β-actin Rabbit mAb (ABclonal, AC026, 1:5000), anti-CD206 Rabbit mAb (ABclonal, A26948, 1:5000), and anti-CD86 Rabbit mAb (ABclonal, A21198, 1:10000). STAT1 monoclonal antibody (Proteintech, 66545-1-Ig, 1:5000), p-STAT1 monoclonal antibody (Proteintech, 82674-10-RR, 1:2000), NF-κB p65 monoclonal antibody (Proteintech, 80979-1-RR, 1:5000), phospho-NF-κB p65 monoclonal antibody (Proteintech, 82335-1-RR, 1:2000), After washing with TBST, the membrane was incubated with the secondary antibody HRP-labeled Goat Anti-Rabbit IgG (H+L) (Beyotime, A0208, 1:8000) or secondary antibody HRP-labeled Goat Anti-Mouse IgG (H+L) (Beyotime, A0216, 1:8000) at room temperature for 2 h. Finally, the membrane was washed with TBST and the images were captured using a digital gel

imaging system.

In vivo antitumor effectiveness evaluation in bilateral tumor model

Balb/c mice, 5 weeks old, were purchased from SLAC Laboratory Animal Co. in Shanghai, China. On day -8, 1×10^6 4T1 cells were implanted into the right axilla of the mice to establish a primary tumor. On day -1, 1×10^6 4T1 cells were implanted into the left axilla to create a distant tumor. Mice were divided into six groups for different treatments (PBS, laser (808 nm, 0.3 W/cm^2), P-CD, P-CD@MM, P-CD + laser, P-CD@MM + laser). On day 0, mice were treated with PBS, P-CD, or P-CD@MM via intravenous injection. On day 1, the primary tumor was irradiated with a laser for 10 min. On day 7, tumors were collected for H&E and TUNEL staining. Primary tumors, distant tumors, spleens, and lymph nodes were collected to assess ICD markers, DC maturation, and T cell activation. We measured the HMGB1 and ATP level in the supernatant of tumor tissue homogenate. Tumor tissues of equal mass were processed identically by adding 500 μL of RIPA lysis buffer and homogenizing on ice. Following homogenization, samples were centrifuged at 12,000 rpm for 15 min at 4 °C, and the resulting supernatants were collected. ATP levels were quantified using an ATP assay kit, while HMGB1 concentrations were determined by ELISA. The evaluation of ICD markers and DC maturation level was similar to the cellular experiments. For the evaluation of T cells, single cell suspensions of tumor tissues and spleen were obtained after mixed collagenase digestion and filtration using cell strainers. Then, anti-FITC-CD3 (Biolegend, 100203, 1:200), anti-APC-CD4 (Biolegend, 100412, 1:200) and anti-PE-CD8a (Biolegend, 162304, 1:200) were utilized to stain cells, which were then analyzed by flow cytometer.

In vivo antitumor effectiveness evaluation in rechallenge tumor model

To assess the long-term immune memory response induced by P-CD@MM + L, a tumor re-challenge model was established. 4T1 tumor-bearing Balb/c mice in each group were intravenously injected with PBS or P-CD@MM on days 0, 2, and 4. After 24 h, tumors were irradiated with an 808 nm laser (0.3 W/cm^2) for 10 min. After tumors were eradicated by P-CD@MM + L, on day 30, 4T1 cells were injected into the opposite axilla of mice to fabricate the rechallenge tumor model. Another 6 healthy mice were utilized as the control, which were also inoculated by 4T1 cells. On day 50, spleens were harvested to analyze the proportion of TEM ($CD3^+$) cells, particularly $CD8^+$ T cells exhibiting high CD44 and low CD62L expression. The single cell suspensions of spleen were stained by anti-CD3-FITC (Biolegend, 102023, 1:200), anti-CD8a-PE (Biolegend, 162304, 1:200), anti-CD44-PE-Cy7 (Biolegend, 103030, 1:200), and anti-CD62L-APC (Biolegend, 161218, 1:200) and then analyzed by flow cytometer.

Pharmacokinetic and metabolism evaluation

Balb/c mice aged 5 weeks (n = 3) were intravenously administered P-CD or P-CD@MM at a dose of 2.0 mg/kg of P-CD. For pharmacokinetic study, blood samples (10 μL) were collected from the tail vein at predetermined time points. Then, blood samples were transferred into heparinized microcentrifuge tubes, followed by dilution with 990 μL of PBS. The samples were centrifuged at 1500 × g for 10 min to isolate plasma. Both P-CDs and P-CD@MM exhibited plasma concentration-time profiles characteristic of a two-compartment pharmacokinetic model, indicating biphasic distribution and elimination kinetics in vivo. For metabolism evaluation, the major organs were collected on the 1st, 7th, and 14th day after administration. In the excretion pathway study, Balb/c mice were intravenously injected with the same dose of P-CD@MM, and

then immediately placed in metabolic cages to collect fecal and urine samples. The collected samples (organs, feces, or urine) were digested with aqua regia and the absorbance at 720 nm was measured to determine the metabolism and excretion pathway of P-CD@MM.

Statistical analysis

Data are representative results from at least three independent experiments and are presented as mean ± standard deviation. All statistical analyses were performed using Origin 2024 and Excel software. Statistical comparisons were performed using one-way ANOVA for multiple comparisons or two-tailed Student's t-test for comparisons between two groups.

Data availability

The authors declare that all relevant data supporting the findings of this study are available within the article, its Supplementary Information, and Source data. Source data are provided with this paper.

References

1. Li J*, et al.* Off-Photosensitizing Derived Immuno-Photodynamic Therapy toward Postoperative Care. *Adv. Funct. Mater.* **35**, 2419598 (2024).
2. Lucky SS, Soo KC, Zhang Y. Nanoparticles in photodynamic therapy. *Chem. Rev.* **115**, 1990-2042 (2015).
3. Li X, Lovell JF, Yoon J, Chen X. Clinical development and potential of photothermal and photodynamic therapies for cancer. *Nat. Rev. Clin. Oncol.* **17**, 657-674 (2020).
4. Jiang Y, Li J, Zhen X, Xie C, Pu K. Dual-peak absorbing semiconducting copolymer nanoparticles for first and second near-infrared window photothermal therapy: a comparative study. *Adv. Mater.* **30**, 1705980 (2018).

5. Yi X*, et al.* Bacteria-triggered tumor-specific thrombosis to enable potent photothermal immunotherapy of cancer. *Sci. Adv.* **6**, eaba3546 (2020).
6. Huang L*, et al.* Mild photothermal therapy potentiates anti-PD-L1 treatment for immunologically cold tumors via an all-in-one and all-in-control strategy. *Nat. Commun.* **10**, 4871 (2019).
7. Nam J, Son S, Park KS, Zou W, Shea LD, Moon JJ. Cancer nanomedicine for combination cancer immunotherapy. *Nat. Rev. Mater.* **4**, 398-414 (2019).
8. Shao Y*, et al.* Engineering of Upconverted Metal-Organic Frameworks for Near-Infrared Light-Triggered Combinational Photodynamic/Chemo-/Immunotherapy against Hypoxic Tumors. *J. Am. Chem. Soc.* **142**, 3939-3946 (2020).
9. He C*, et al.* Core-shell nanoscale coordination polymers combine chemotherapy and photodynamic therapy to potentiate checkpoint blockade cancer immunotherapy. *Nat. Commun.* **7**, 12499 (2016).
10. Wei Q, Liu S, Huang X, Xin H, Ding J. Immunologically effective biomaterials-enhanced vaccines against infection of pathogenic microorganisms. *Biosaf. Health* **5**, 45-61 (2023).
11. Guo Y*, et al.* Magnetic-responsive and targeted cancer nanotheranostics by PA/MR bimodal imaging-guided photothermally triggered immunotherapy. *Biomaterials* **219**, 119370 (2019).
12. Li J*, et al.* Second Near-Infrared Photothermal Semiconducting Polymer Nanoadjuvant for Enhanced Cancer Immunotherapy. *Adv. Mater.* **33**, 2003458 (2021).
13. Zheng RR*, et al.* Paraptosis Inducer to Effectively Trigger Immunogenic Cell Death for Metastatic Tumor Immunotherapy with IDO Inhibition. *ACS Nano* **17**, 9972-9986 (2023).
14. Li X*, et al.* A Diketopyrrolopyrrole-Based All-in-One Nanoplatform for Self-Reinforcing Mild Photothermal Therapy Cascade Immunotherapy for Tumors. *Adv. Healthcare Mater.* **13**, 2400766 (2024).
15. Liu T*, et al.* Rhythmic mild photothermal therapy enhancing anti-PD-L1 response for oral squamous cell carcinoma immunotherapy. *Chem. Eng. J.* **488**, 150908 (2024).
16. Wang M*, et al.* A Noble AuPtAg-GOx Nanozyme for Synergistic Tumor Immunotherapy Induced by Starvation Therapy-Augmented Mild Photothermal Therapy. *Adv. Sci.* **9**, 2202332 (2022).
17. Liu C, Li S, Ma R, Ji C, Müllen K, Yin M. NIR-triggered dual sensitization of nanoparticles for mild

tumor phototherapy. *Nano Today* **42**, 101363 (2022).

18. Sun J*, et al.* Multi-bioactive poly(amino acid)-metal-organic framework nanocomposite for reinforced cascading photodynamic immunotherapy of cancer. *Biomaterials* **324**, 123488 (2025).
19. Kang X*, et al.* A photo-triggered self-accelerated nanoplatform for multifunctional image-guided combination cancer immunotherapy. *Nat. Commun.* **14**, 5216 (2023).
20. Luo T*, et al.* Nanoscale Metal-Organic Frameworks Stabilize Bacteriochlorins for Type I and Type II Photodynamic Therapy. *J. Am. Chem. Soc.* **142**, 7334-7339 (2020).
21. Shi Z*, et al.* Engineering Structural Metal–Organic Framework for Hypoxia-Tolerant Type I Photodynamic Therapy against Hypoxic Cancer. *ACS Materials Lett.* **3**, 781-789 (2021).
22. Deng Y*, et al.* 3-Bromopyruvate-Conjugated Nanoplatform-Induced Pro-Death Autophagy for Enhanced Photodynamic Therapy against Hypoxic Tumor. *ACS Nano* **14**, 9711-9727 (2020).
23. Chen D*, et al.* A Highly-Efficient Type I Photosensitizer with Robust Vascular-Disruption Activity for Hypoxic-and-Metastatic Tumor Specific Photodynamic Therapy. *Small* **16**, 2001059 (2020).
24. Yuan Z*, et al.* Near-Infrared Light-Triggered Nitric-Oxide-Enhanced Photodynamic Therapy and Low-Temperature Photothermal Therapy for Biofilm Elimination. *ACS Nano* **14**, 3546-3562 (2020).
25. Wen K*, et al.* Achieving Efficient NIR-II Type-I Photosensitizers for Photodynamic/Photothermal Therapy upon Regulating Chalcogen Elements. *Adv. Mater.* **34**, 2108146 (2022).
26. Wen K*, et al.* Precisely Tuning Photothermal and Photodynamic Effects of Polymeric Nanoparticles by Controlled Copolymerization. *Angew. Chem. Int. Ed.* **59**, 12756-12761 (2020).
27. Wang Y, Gong N, Li Y, Lu Q, Wang X, Li J. Atomic-Level Nanorings (A-NRs) Therapeutic Agent for Photoacoustic Imaging and Photothermal/Photodynamic Therapy of Cancer. *J. Am. Chem. Soc.* **142**, 1735-1739 (2020).
28. Chuang C-C*, et al.* Stem Cell-Based Delivery of Gold/Chlorin e6 Nanocomplexes for Combined Photothermal and Photodynamic Therapy. *ACS Appl. Mater. Interfaces* **12**, 30021-30030 (2020).
29. Chen W*, et al.* Black Phosphorus Nanosheet-Based Drug Delivery System for Synergistic Photodynamic/Photothermal/Chemotherapy of Cancer. *Adv. Mater.* **29**, 1603864 (2017).
30. Chang X*, et al.* Enhanced manipulation of tumor microenvironments by nanomotor for synergistic

therapy of malignant tumor. *Biomaterials* **290**, 121853 (2022).

31. Zhang L, Yang XQ, Wei JS, Li X, Wang H, Zhao YD. Intelligent gold nanostars for in vivo CT imaging and catalase-enhanced synergistic photodynamic & photothermal tumor therapy. *Theranostics* **9**, 5424-5442 (2019).
32. Yu Y*, et al.* Bortezomib-Encapsulated CuS/Carbon Dot Nanocomposites for Enhanced Photothermal Therapy via Stabilization of Polyubiquitinated Substrates in the Proteasomal Degradation Pathway. *ACS Nano* **14**, 10688-10703 (2020).
33. Li B*, et al.* Aggregation-Induced Emission-Based Macrophage-Like Nanoparticles for Targeted Photothermal Therapy and Virus Transmission Blockage in Monkeypox. *Adv. Mater.* **36**, 2305378 (2024).
34. Xi D*, et al.* NIR Light-Driving Barrier-Free Group Rotation in Nanoparticles with an 88.3% Photothermal Conversion Efficiency for Photothermal Therapy. *Adv. Mater.* **32**, 1907855 (2020).
35. Zhu D*, et al.* Tumor-derived exosomes co-delivering aggregation-induced emission luminogens and proton pump inhibitors for tumor glutamine starvation therapy and enhanced type-I photodynamic therapy. *Biomaterials* **283**, 121462 (2022).
36. Wang J, Gong Q, Jiao L, Hao E. Research advances in BODIPY-assembled supramolecular photosensitizers for photodynamic therapy. *Coordin. Chem. Rev.* **496**, 215367 (2023).
37. Liu S*, et al.* Cationization-Enhanced Type I and Type II ROS Generation for Photodynamic Treatment of Drug-Resistant Bacteria. *ACS Nano* **16**, 9130-9141 (2022).
38. Lu J*, et al.* Spin Manipulation Engineering of Photodynamic Intermediates: Magnetic Amplification of Oxyradicals Generation for Enhanced Antitumor Phototherapeutic Efficacy. *J. Am. Chem. Soc.* **147**, 18100-18109 (2025).
39. Cai X*, et al.* Nanoparticles Selectively Regulate the Generation and Scavenging of Multiple Reactive Oxygen Species at Designated Locations and States. *J. Am. Chem. Soc.* **147**, 21385-21399 (2025).
40. Yan K*, et al.* Versatile Nanoplatforms with enhanced Photodynamic Therapy: Designs and Applications. *Theranostics* **10**, 7287-7318 (2020).
41. Lo P-C, Salome Rodriguez-Morgade M, Pandey RK, Ng DKP, Torres T, Dumoulin F. The unique

features and promises of phthalocyanines as advanced photosensitisers for photodynamic therapy of cancer. *Chem. Soc. Rev.* **49**, 1041-1056 (2020).

42. Xu G, *et al.* A supramolecular photosensitizer derived from an Arene-Ru(II) complex self-assembly for NIR activated photodynamic and photothermal therapy. *Nat. Commun.* **13**, 3064 (2022).
43. Zhang DY, *et al.* Tumor Microenvironment-Responsive Theranostic Nanoplatform for Guided Molecular Dynamic/Photodynamic Synergistic Therapy. *ACS Appl. Mater. Interfaces* **13**, 17392-17403 (2021).
44. Jian HJ, *et al.* Super-cationic carbon quantum dots synthesized from spermidine as an eye drop formulation for topical treatment of bacterial keratitis. *ACS Nano* **11**, 6703-6716 (2017).
45. Liu KK, *et al.* Efficient red/near-infrared-emissive carbon nanodots with multiphoton excited upconversion fluorescence. *Adv. Sci.* **6**, 1900766 (2019).
46. Rosenkrans ZT, *et al.* Selenium-Doped Carbon Quantum Dots Act as Broad-Spectrum Antioxidants for Acute Kidney Injury Management. *Adv. Sci.* **7**, 2000420 (2020).
47. Cai Y, *et al.* Insights on forming N,O-coordinated Cu single-atom catalysts for electrochemical reduction CO_2 to methane. *Nat. Commun.* **12**, 586 (2021).
48. Yang H, *et al.* Hydrophobic carbon dots with blue dispersed emission and red aggregation-induced emission. *Nat. Commun.* **10**, 1789 (2019).
49. Gong N, *et al.* Carbon-dot-supported atomically dispersed gold as a mitochondrial oxidative stress amplifier for cancer treatment. *Nat. Nanotechnol.* **14**, 379-387 (2019).
50. Geng B, *et al.* Near-infrared phosphorescent carbon dots for sonodynamic precision tumor therapy. *Nat. Commun.* **13**, 5735 (2022).
51. Jia Q, *et al.* A Magnetofluorescent Carbon Dot Assembly as an Acidic H_2O_2 -Driven Oxygenerator to Regulate Tumor Hypoxia for Simultaneous Bimodal Imaging and Enhanced Photodynamic Therapy. *Adv. Mater.* **30**, 1706090 (2018).
52. Song RW, Jiang TC, Zhang XY, Shen CL, Lou Q, Shan CX. Triplet Electron Exchange in Carbon Nanodots-assisted Long-persistent near-infrared Chemiluminescence for Oncology Synergistic Imaging and Therapy. *Adv. Sci.* **12**, 2411898 (2025).

53. Zhang Y*, et al.* Carbon dots nanophotosensitizers with tunable reactive oxygen species generation for mitochondrion-targeted type I/II photodynamic therapy. *Biomaterials* **293**, 121953 (2023).

54. Yan Y*, et al.* Systematic bandgap engineering of graphene quantum dots and applications for photocatalytic water splitting and CO_2 reduction. *ACS Nano* **12**, 3523-3532 (2018).

55. Li Y*, et al.* Enhancing the magnetic relaxivity of MRI contrast agents via the localized superacid microenvironment of graphene quantum dots. *Biomaterials* **250**, 120056 (2020).

56. Luo T*, et al.* Bifunctional Cascading Nanozymes Based on Carbon Dots Promotes Photodynamic Therapy by Regulating Hypoxia and Glycolysis. *ACS Nano* **17**, 16715-16730 (2023).

57. Xu L*, et al.* Ultralong Organic Phosphorescent Nanocrystals with Long-Lived Triplet Excited States for Afterglow Imaging and Photodynamic Therapy. *ACS Appl. Mater. Interfaces* **12**, 18385-18394 (2020).

58. Dai J*, et al.* Efficient Near-Infrared Photosensitizer with Aggregation-Induced Emission for Imaging-Guided Photodynamic Therapy in Multiple Xenograft Tumor Models. *ACS Nano* **14**, 854-866 (2020).

59. Xu J*, et al.* All-in-One Theranostic Nanomedicine with Ultrabright Second Near-Infrared Emission for Tumor-Modulated Bioimaging and Chemodynamic/Photodynamic Therapy. *ACS Nano* **14**, 9613-9625 (2020).

60. Liu M*, et al.* Golgi apparatus-targeted aggregation-induced emission luminogens for effective cancer photodynamic therapy. *Nat. Commun.* **13**, 2179 (2022).

61. Li S*, et al.* Targeted tumour theranostics in mice via carbon quantum dots structurally mimicking large amino acids. *Nat. Biomed. Eng.* **4**, 704-716 (2020).

62. Xin Q, Ma H, Wang H, Zhang XD. Tracking tumor heterogeneity and progression with near-infrared II fluorophores. *Exploration* **3**, 20220011 (2023).

63. Jiang K*, et al.* Red, Green, and Blue Luminescence by Carbon Dots: Full-Color Emission Tuning and Multicolor Cellular Imaging. *Angew. Chem. Int. Ed.* **54**, 5360-5363 (2015).

64. Zhang L*, et al.* Cancer-macrophage hybrid membrane-camouflaged photochlor for enhanced sonodynamic therapy against triple-negative breast cancer. *Nano Res.* **15**, 4224-4232 (2022).

65. Yang G, Ni JS, Li Y, Zha M, Tu Y, Li K. Acceptor Engineering for Optimized ROS Generation

Facilitates Reprogramming Macrophages to M1 Phenotype in Photodynamic Immunotherapy. *Angew. Chem. Int. Ed.* **60**, 5386-5393 (2021).

66. Xiao T*, et al.* Macrophage Membrane-Camouflaged Responsive Polymer Nanogels Enable Magnetic Resonance Imaging-Guided Chemotherapy/Chemodynamic Therapy of Orthotopic Glioma. *ACS Nano* **15**, 20377-20390 (2021).
67. Yu N*, et al.* Near-infrared photoactivatable semiconducting polymer nanocomplexes with bispecific metabolism interventions for enhanced cancer immunotherapy. *Nano Today* **46**, 101600 (2022).
68. Li Y*, et al.* Sono/Photodynamic Nanomedicine-Elicited Cancer Immunotherapy. *Adv. Funct. Mater.* **31**, 2008061 (2020).

Acknowledgements

This work was supported by the National Natural Science Foundation of China (No. 12375345 to L.S., 22278262 to D.P.), the Science and Technology Commission of Shanghai Municipality (No. 25ZR1402150 to B.G.), the Young Elite Scientists Sponsorship Program by CAST (No. 2023QNRC001 to B.G.), the Innovative Research Team of High-level Local Universities in Shanghai, and the cultivation project (ynms202103 to L.S.) from Shanghai Jiao Tong University affiliated Sixth People's Hospital.

Author contributions

B.G. and D.P. designed and directed the study, analysed the data and wrote the manuscript. S.S. and L.S. directed the study and improved the manuscript. Z.Z., L.Y., and W.L. performed experiments and analyzed data. J.H. provided important suggestions and improved the manuscript. Y.W. and H.D. provided advice and technical help with cell experiments and mouse cancer models. All authors discussed the results and reviewed the manuscript.

Competing interests

The authors declare no competing interests.

Figure legends

Fig. 1. Schematic illustration of D-π-A sensitized CDs as long-lived triplet photosensitizers for low-thermal NIR-photodynamic immunotherapy. A molecular-engineering combination strategy was employed to synthesize three types of CDs with different regional modifications for the demonstration of the CD-based design of the D-π-A sensitized type-I/II PSs. M1-like macrophage-derived cell membrane was then utilized to camouflage P-CD to realize preferential tumor accumulation for NIR-excited hypoxia-regulated photodynamic therapy. (CT-S_1: Charge Transfer-S_1; ISC: Intersystem Crossing; CT-T_1: Charge Transfer-T_1; PTT: Photothermal Therapy; ICD: Immunogenic Cell Death; HMGB1: High Mobility Group Box 1; ATP: Adenosine Triphosphate; CRT: Calreticulin).

Fig. 2. Molecular engineering of D-π-A sensitized CDs. (a) Synthetic route of three kinds of CDs with different N doping features. (b-g) TEM and high-resolution TEM images of O-CD, M-CD, and P-CD. (h, i) Summary of theoretical models and structural parameters of O-CD, M-CD, and P-CD. (j, k) High-resolution N 1s spectrum and absorption spectrum (inset: Tauc plot curves) of ICG-CD, O-CD, M-CD, and P-CD. For (b-g), experiment was repeated three times independently with similar results. For (j, k), the data shown are representative of three independent experiments with similar results. Source data are provided as a Source Data file.

Fig. 3. The photothermal properties of CDs. (a-c) Enhanced photothermal effect evaluation

through measuring the temperature changes and comparing the photothermal conversion efficiency of O-CD, M-CD and P-CD solutions. (d-i) Temperature changes of these CDs when varying the power density of laser (d-f) and the concentration of samples (g-i). For (a-i), the data shown are representative of three independent experiments with similar results. Source data are provided as a Source Data file.

Fig. 4. Enhanced photodynamic properties of P-CD in the D-π-A configuration. (a, b) Measurements and comparison of ROS generation efficiency of O-CD, M-CD, and P-CD under 808 nm laser irradiation in the absence or presence of hypoxia conditions. (c, d) Measurements and comparison of $O_2^{\bullet-}$ generation efficiency of O-CD, M-CD, and P-CD under 808 nm laser irradiation in the absence or presence of hypoxia conditions. (e, f) ESR spectra of laser-triggered $^1O_2$ and $O_2^{\bullet-}$ generation of O-CD, M-CD and P-CD. (g-i) Time-resolved PL spectra of O-CD, M-CD, and P-CD and the corresponding fitting curves. (j) Solvation effect and peak positions of O-CD, M-CD and P-CD. (k) Schematic diagram of P-CD-mediated photodynamic mechanism. For (a-j), The data shown are representative of three independent experiments with similar results. Source data are provided as a Source Data file.

Fig. 5. Theoretical calculation of CDs. (a) Illustration of the frontier molecular orbitals (LUMOs and HOMOs) of O-CD, M-CD and P-CD. (b-d) Singlet and triplet energy levels and ΔE_{ST} (b), Surface electrostatic potential (c), Fukui-DD function analysis (d) of O-CD, M-CD and P-CD.

Fig. 6. In vitro antitumor effectiveness evaluation of P-CD@MM mediated PDT. (a, b) TEM images of P-CD@MM. (c) Measurements of the expression levels of CD86 and CD206 in each group. (d) Representative fluorescence images of cellular uptake of P-CD@MM in 4T1 or NIH-

3T3. (e, f) Relative cell viability of NIH-3T3 and 4T1 cells after different treatments (n = 6 independent samples). (g, h) Live/dead cell and ROS staining of 4T1 cells after different treatments. For (a-d, g, h), experiment was repeated three times independently with similar results. Data are presented as mean ± SD and statistical significance was analyzed via two-tailed Student's *t*-test. Source data are provided as a Source Data file.

Fig. 7. P-CD@MM-mediated PDT induces ICD and M1-like polarization in vitro. (a) Confocal images of CRT exposure in 4T1 cells after different treatments. (b, c) Evaluation of HMGB1 and ATP levels in 4T1 cells after different treatments (n = 6 independent samples). (d) A scheme to show the experimental process of the evaluation of DC maturation (Relative drawing materials were created in BioRender. zhenlin, Z. (2026) https://BioRender.com/9u519d6). (e, f) Evaluation of DC maturation level in each group (n = 6 mice). (g-i) Flow cytometry analysis and the corresponding quantitative results of $CD86^+$ and $CD206^+$ expression in TAMs of BMDM after different treatments (n = 6 mice). For (a), experiment was repeated three times independently with similar results. Data are presented as mean ± SD and statistical significance was analyzed via one-way ANOVA. Source data are provided as a Source Data file.

Fig. 8. In vivo photoimmunotherapy antitumor effectiveness evaluation. (a) A scheme to show the administration procedure of P-CD@MM-mediated PDT (Relative drawing materials were created in BioRender. zhenlin, Z. (2026) https://BioRender.com/9u519d6). (b) In vivo NIR imaging of mice with free P-CDs (n = 3 mice). (c) Tumor-targeted in vivo NIR imaging of mice with P-CD@MM (n = 3 mice). (d) Ex vivo NIR imaging of major tissues and tumors with P-CD@MM (n = 3 mice). (e) Infrared imaging of tumor temperature with P-CD@MM under NIR

laser irradiation for 10 minutes (n = 3 mice). (f) Immunofluorescence staining for HIF-1α expression levels assays (n = 3 mice). (g, h) Antitumor effectiveness evaluation of P-CD@MM-mediated PDT through measuring the primary tumor volume and distant tumor volume (n = 6 mice). (i) ROS staining images of tumors after indicated treatments with DHE as the ROS probe (n = 3 mice). For (f, i), experiment was repeated three times independently with similar results. Data are presented as mean ± SD and statistical significance was analyzed via two-tailed Student's *t*-test. Source data are provided as a Source Data file.

Fig. 9. In vivo photoimmunotherapy antitumor mechanism. (a) CRT staining of tumor tissues after different treatments (n = 3 mice). (b) Expression levels of $CD4^+$ T cells and $CD8^+$ T cells in the primary tumors after different treatments (n = 6 mice). (c) Expression levels of $CD86^+$ and $CD206^+$ in TAMs in the primary tumors after different treatments (n = 6 mice). (d) Schematic diagram of P-CD@MM-mediated PDT to induce an immune response in vivo (Relative drawing materials were created in BioRender. zhenlin, Z. (2026) https://BioRender.com/9u519d6). For (a), experiment was repeated three times independently with similar results.

Fig. 10. Long-term immunological memory evaluation. (a) Schematic illustration of the experimental timeline to assess the antitumor immunological memory response triggered by P-CD@MM-mediated combination therapy (Relative drawing materials were created in BioRender. zhenlin, Z. (2026) https://BioRender.com/9u519d6). (b-d) Tumor volume and body weight of mice after different treatments (n = 6 mice). (e-g) The expression of $CD4^+CD8^+$ T cells in the rechallenged tumors (n = 6 mice). (h, i) The expression of $CD8^+$ memory T cells ($CD3^+CD8^+CD44^+CD62L^-$) in spleen of mice with different treatments (n = 6 mice). Data are

presented as mean ± SD and statistical significance was analyzed via two-tailed Student's *t*-test.

Source data are provided as a Source Data file.

Editorial summary

The properties of small-sized carbon dots have been exploited to generate theranostic agents for bioimaging and imaging-guided cancer therapies. Here the authors report the design and characterization of D-π-A sensitized carbon dots for type-I/II photodynamic therapy (PDT), showing PDT-induced anti-tumor activity in preclinical models.

Peer Review Information: *Nature Communications* thanks Mingtao Zheng and the other, anonymous, reviewer(s) for their contribution to the peer review of this work. A peer review file is available.

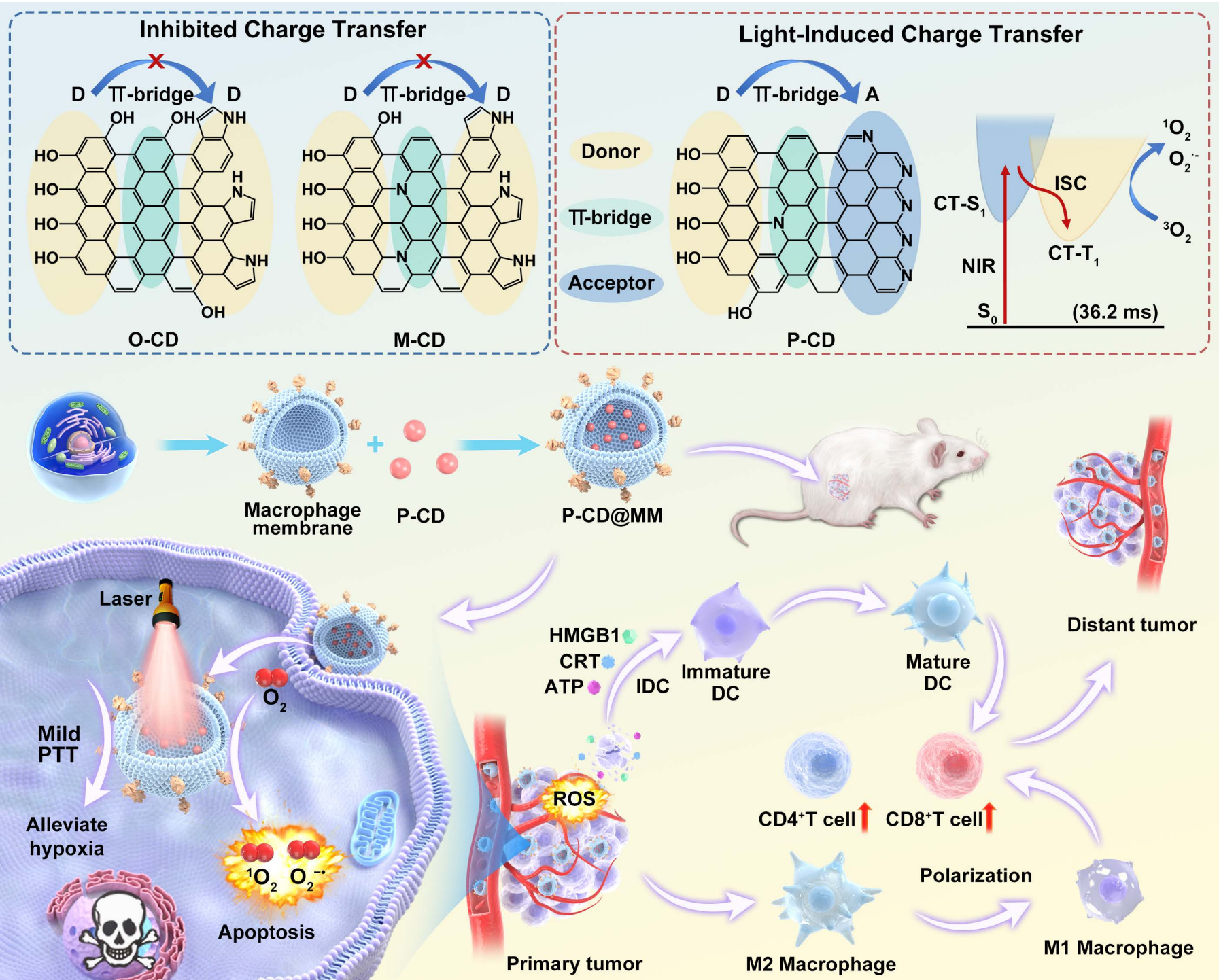
Inhibited Charge Transfer
D
π-bridge
D
O-CD
M-CD
Light-Induced Charge Transfer
D
π-bridge
A
Donor
π-bridge
Acceptor
P-CD
CT-S1
ISC
CT-T1
NIR
S0
(36.2 ms)
1O2
O2·-
3O2
Macrophage membrane
P-CD
P-CD@MM
Distant tumor
Laser
O2
Mild PTT
Alleviate hypoxia
1O2
O2·-
Apoptosis
HMGB1
CRT
ATP
IDC
Immature DC
Mature DC
ROS
CD4+T cell
CD8+T cell
Primary tumor
M2 Macrophage
Polarization
M1 Macrophage

a

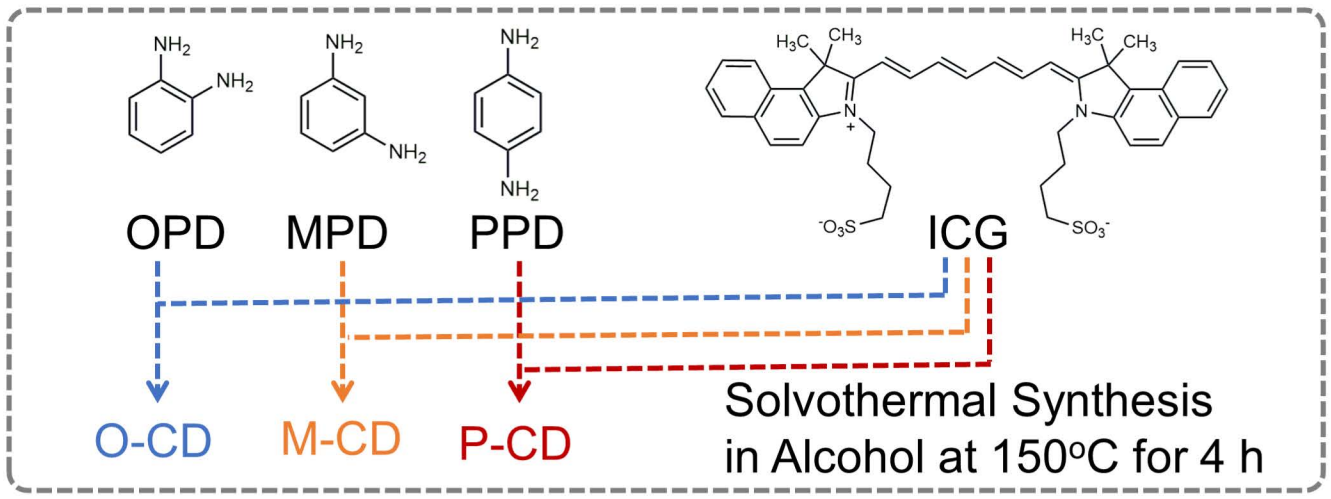

b

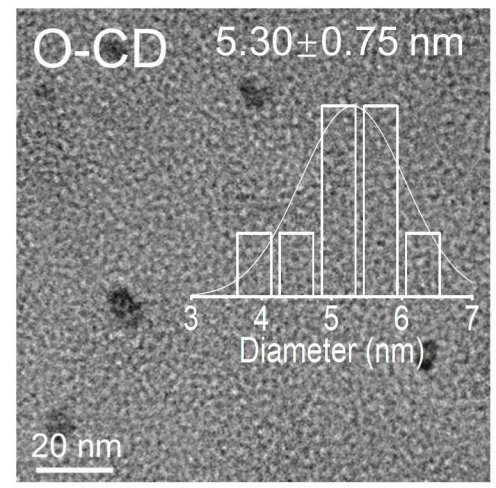

e

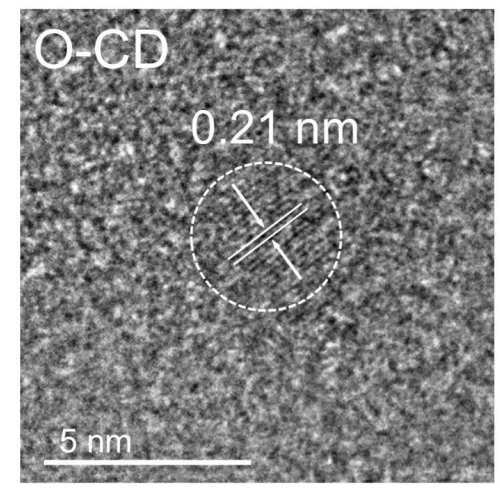

c

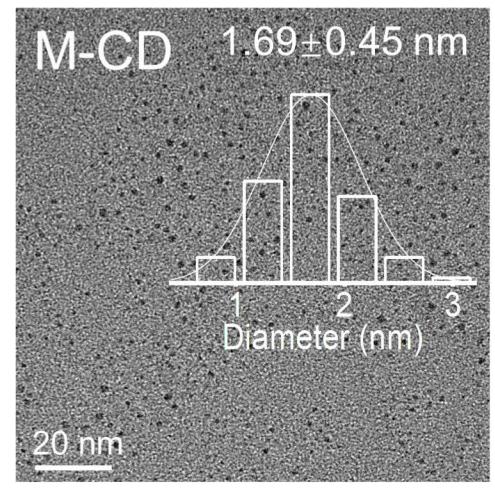

f

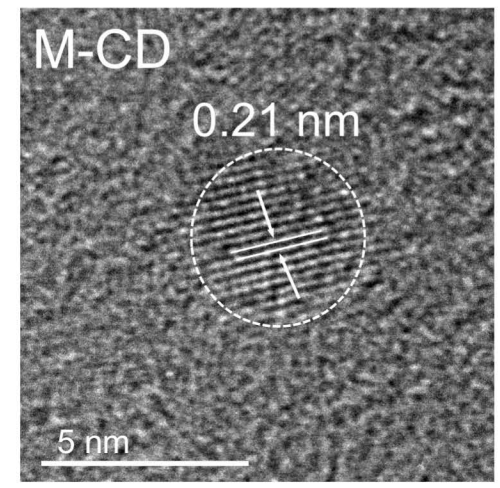

d

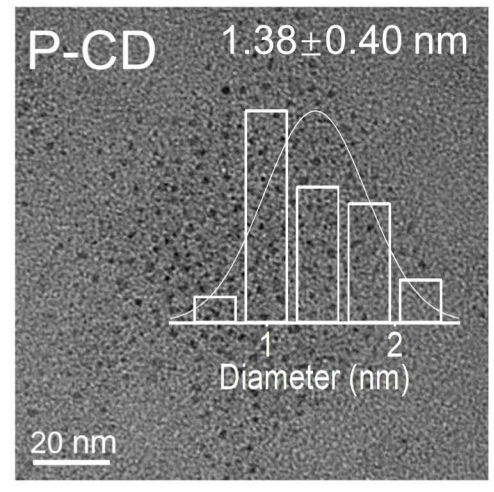

g

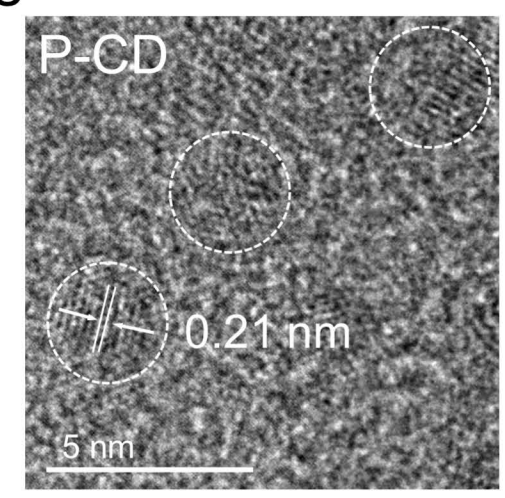

h

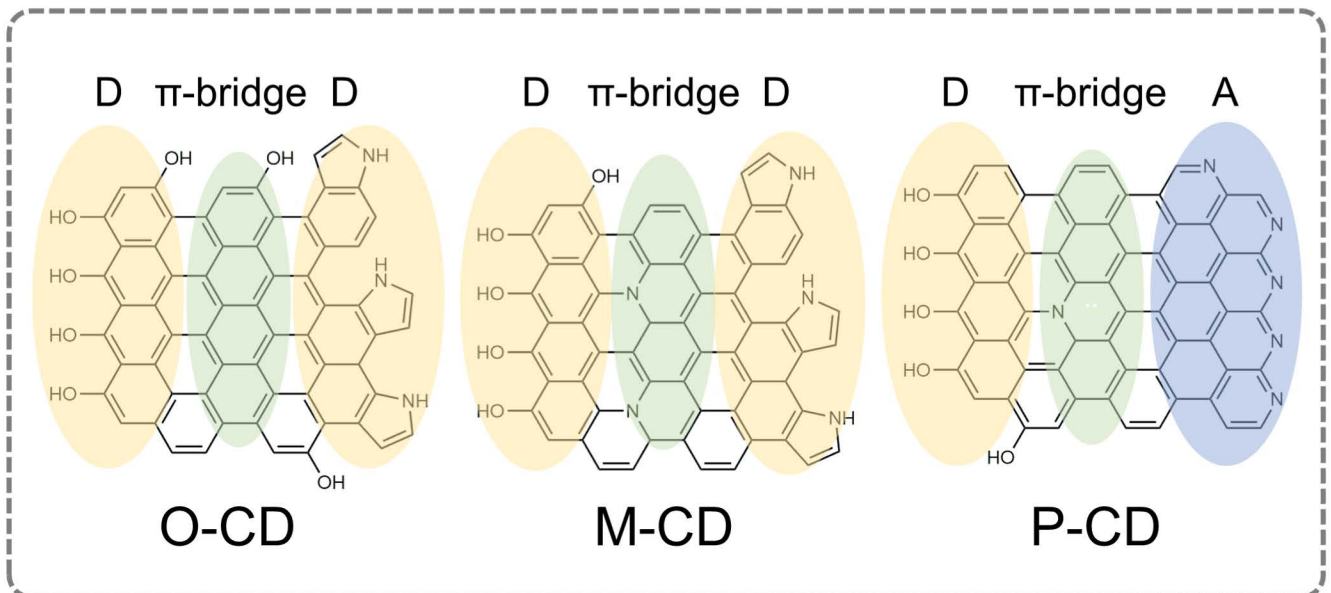

i

Sample	Element content			Donor		Acceptor
	N (at.%)	O (at.%)	S (at.%)	O-H (at.%)	Pyrrolic N (at.%)	Pyridinic N (at.%)
O-CD	5.82	17.33	1.74	16.38	5.82	-
M-CD	8.33	10.55	1.84	7.60	5.14	-
P-CD	10.31	9.79	1.80	7.92	-	8.68

j

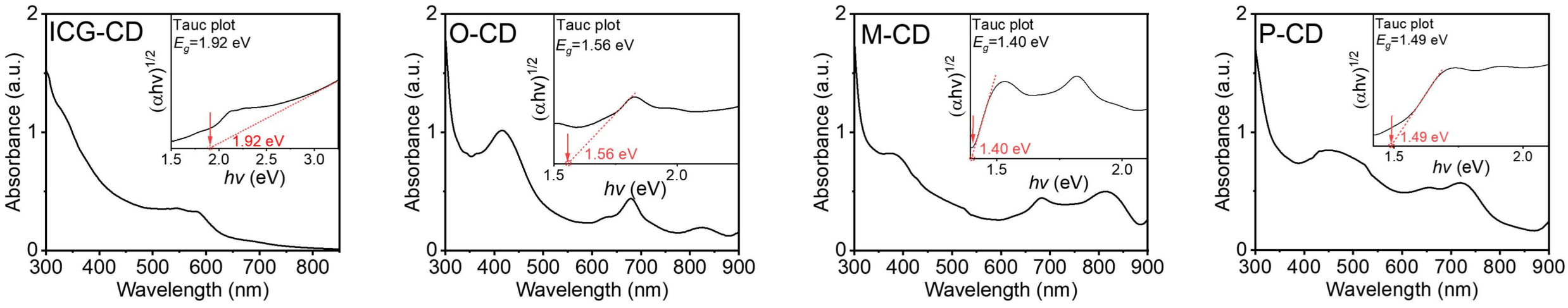

k

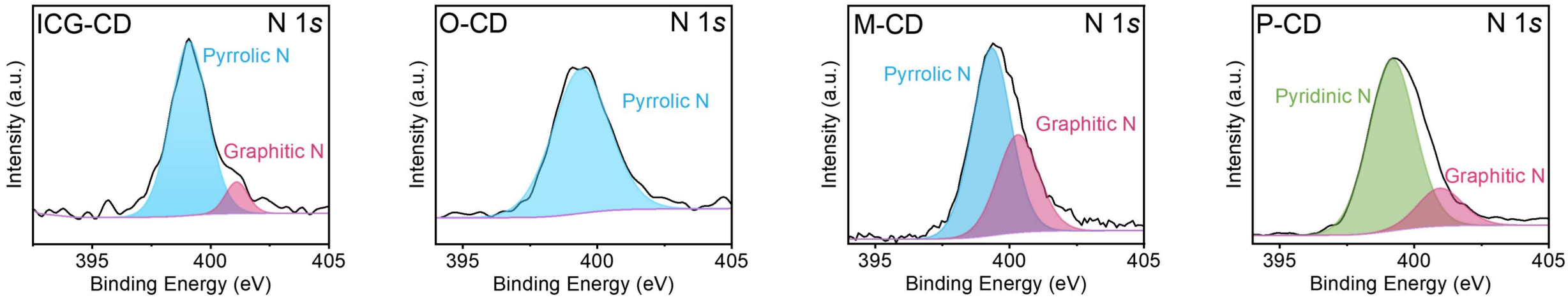

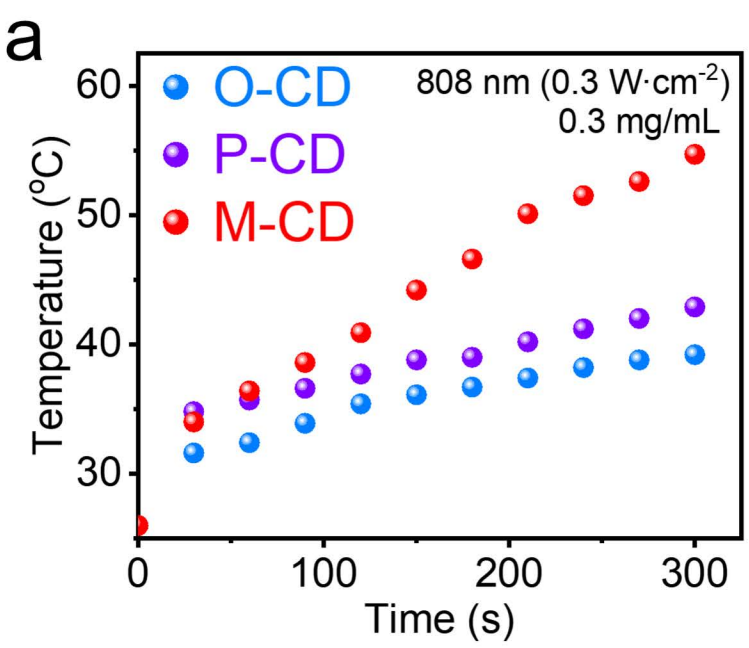
a
O-CD
P-CD
M-CD
808 nm (0.3 W·cm-2)
0.3 mg/mL
Temperature (°C)
Time (s)

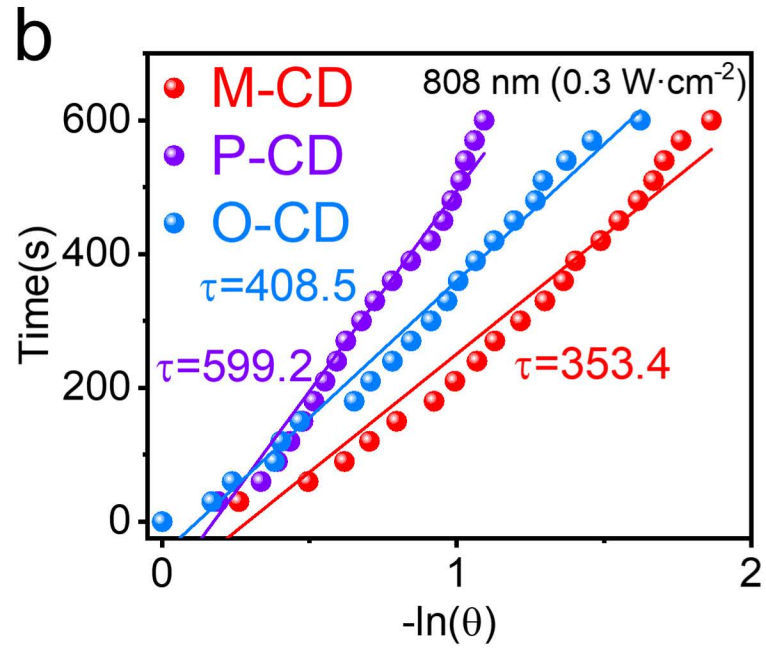
b
M-CD
P-CD
O-CD
808 nm (0.3 W·cm-2)
τ=408.5
τ=599.2
τ=353.4
Time(s)
-ln(θ)

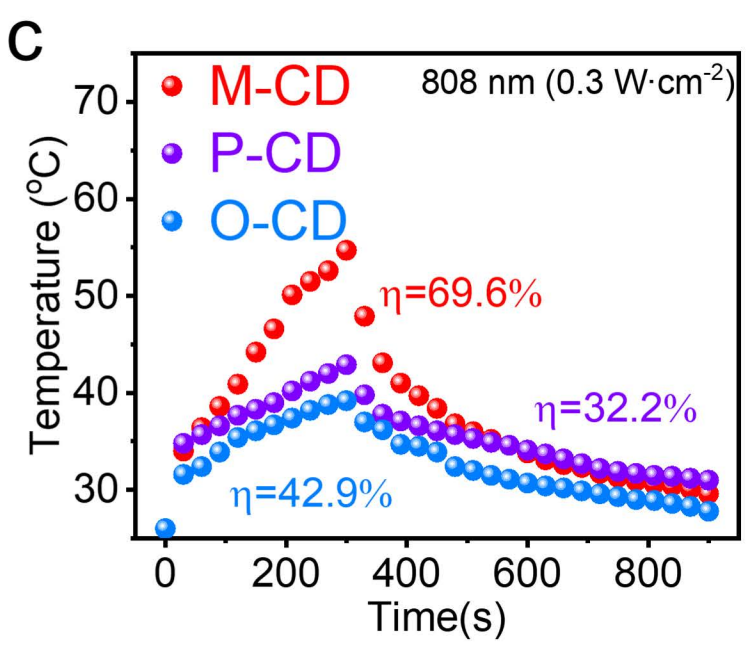
c
M-CD
P-CD
O-CD
808 nm (0.3 W·cm-2)
η=69.6%
η=32.2%
η=42.9%
Temperature (°C)
Time(s)

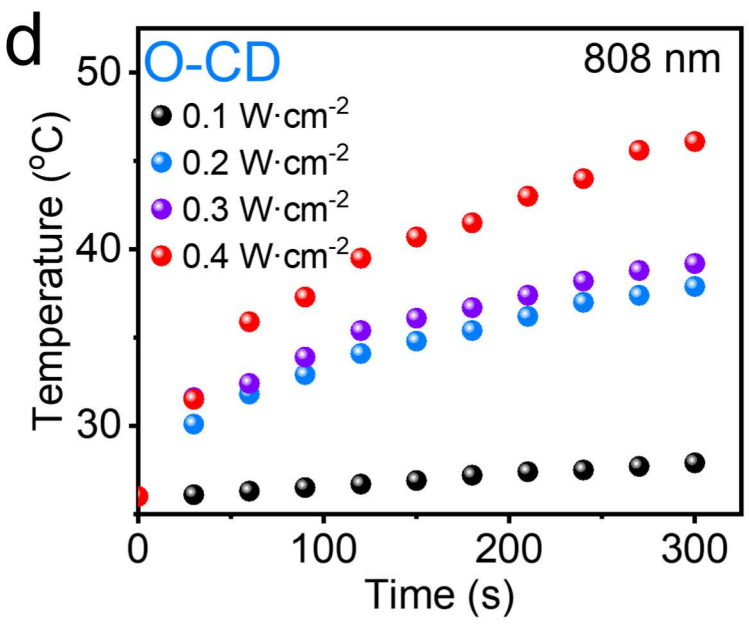
d
O-CD
808 nm
0.1 W·cm-2
0.2 W·cm-2
0.3 W·cm-2
0.4 W·cm-2
Temperature (°C)
Time (s)

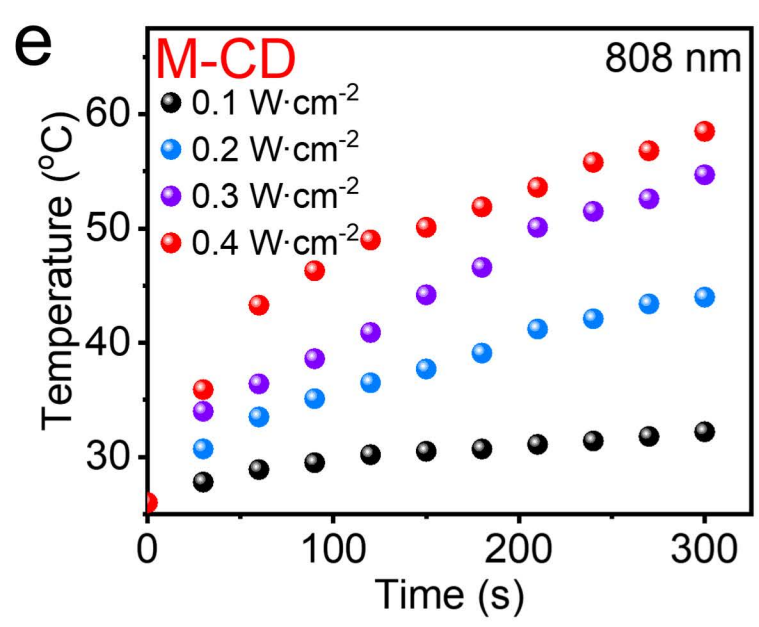
e
M-CD
808 nm
0.1 W·cm-2
0.2 W·cm-2
0.3 W·cm-2
0.4 W·cm-2
Temperature (°C)
Time (s)

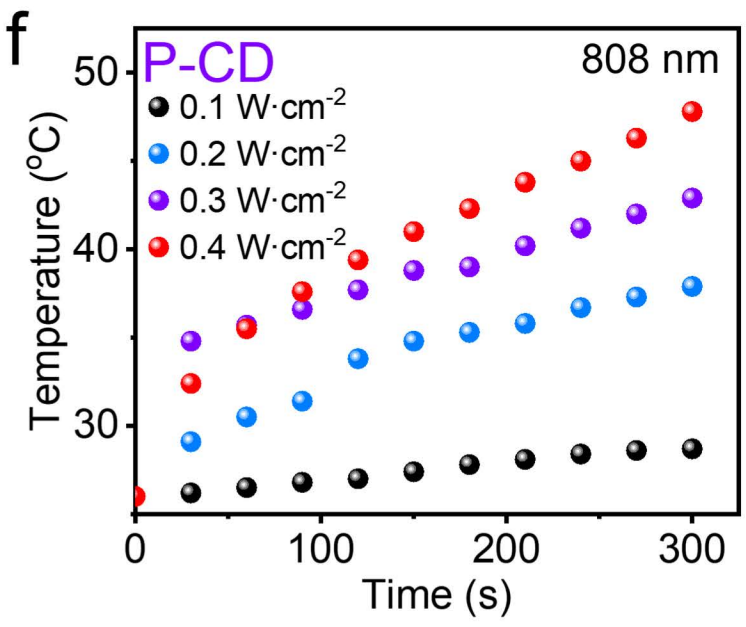
f
P-CD
808 nm
0.1 W·cm-2
0.2 W·cm-2
0.3 W·cm-2
0.4 W·cm-2
Temperature (°C)
Time (s)

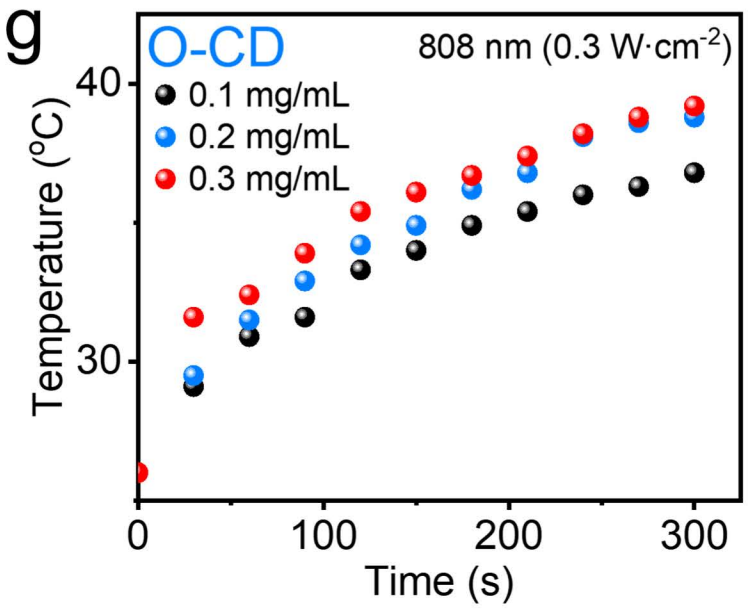
g
O-CD
808 nm (0.3 W·cm-2)
0.1 mg/mL
0.2 mg/mL
0.3 mg/mL
Temperature (°C)
Time (s)

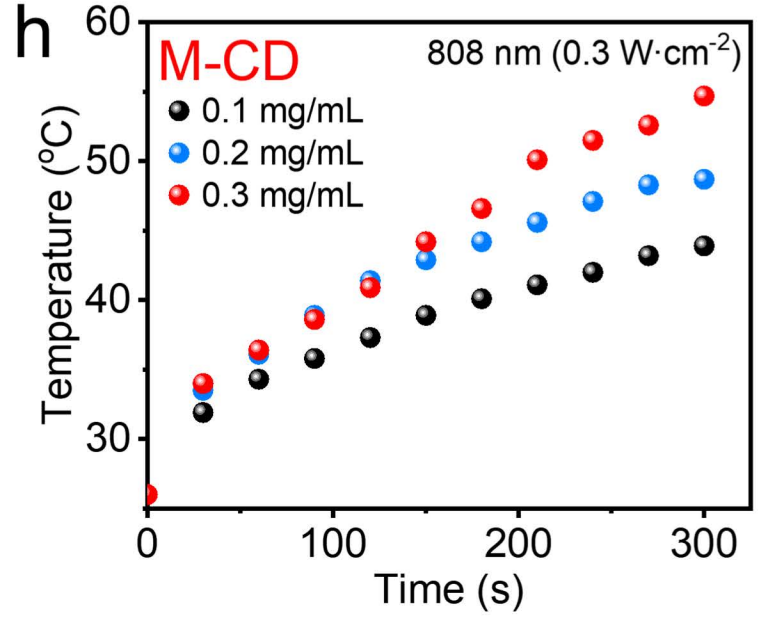
h
M-CD
808 nm (0.3 W·cm-2)
0.1 mg/mL
0.2 mg/mL
0.3 mg/mL
Temperature (°C)
Time (s)

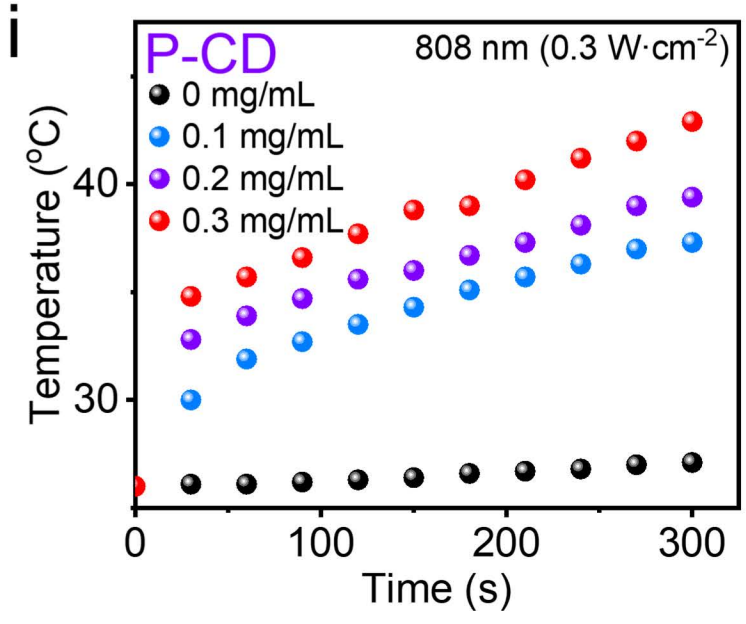
i
P-CD
808 nm (0.3 W·cm-2)
0 mg/mL
0.1 mg/mL
0.2 mg/mL
0.3 mg/mL
Temperature (°C)
Time (s)

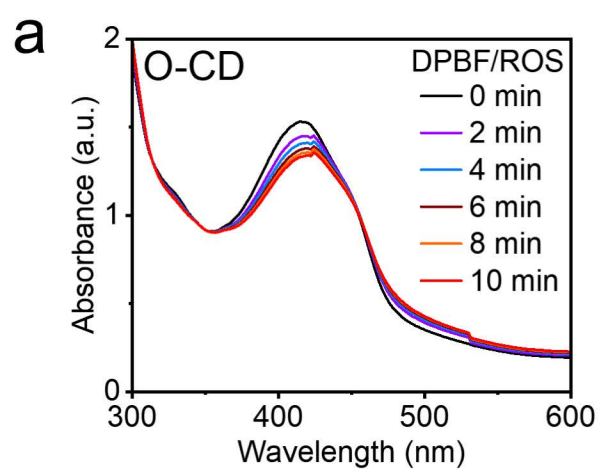
a
O-CD
DPBF/ROS
0 min
2 min
4 min
6 min
8 min
10 min
Absorbance (a.u.)
Wavelength (nm)

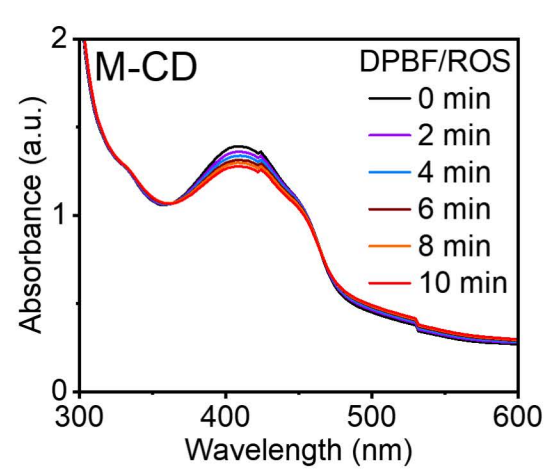
M-CD
DPBF/ROS
0 min
2 min
4 min
6 min
8 min
10 min
Absorbance (a.u.)
Wavelength (nm)

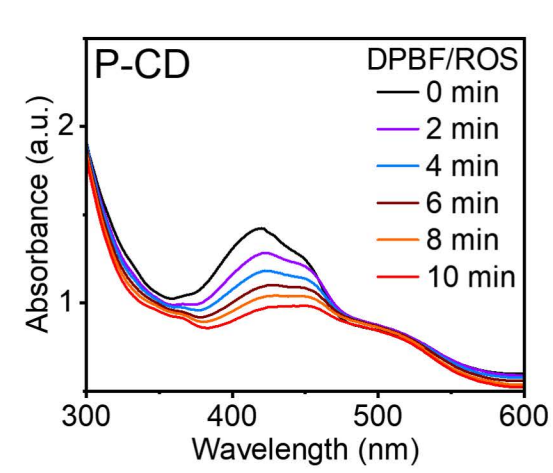
P-CD
DPBF/ROS
0 min
2 min
4 min
6 min
8 min
10 min
Absorbance (a.u.)
Wavelength (nm)

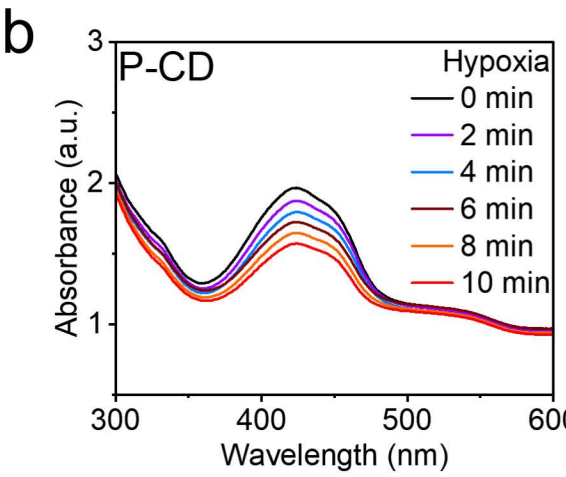
b
P-CD
Hypoxia
0 min
2 min
4 min
6 min
8 min
10 min
Absorbance (a.u.)
Wavelength (nm)

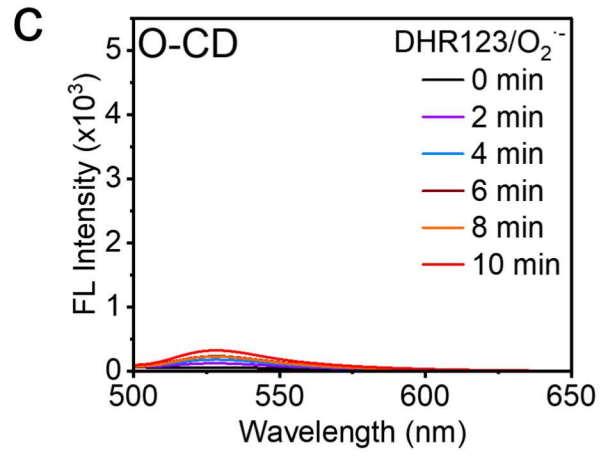
c
O-CD
DHR123/O2•-
0 min
2 min
4 min
6 min
8 min
10 min
FL Intensity (x10³)
Wavelength (nm)

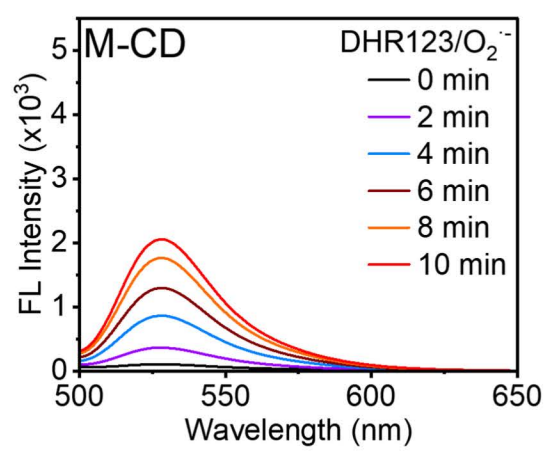
M-CD
DHR123/O2•-
0 min
2 min
4 min
6 min
8 min
10 min
FL Intensity (x10³)
Wavelength (nm)

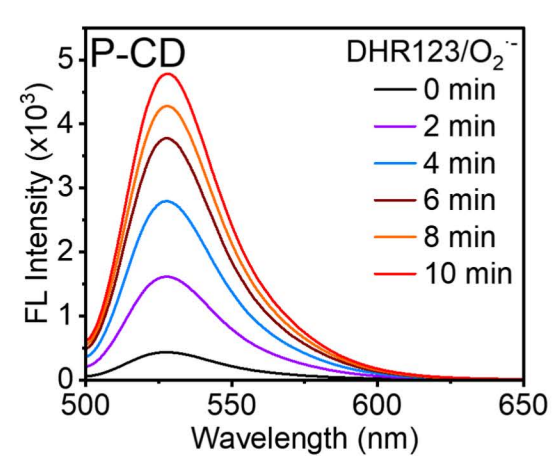
P-CD
DHR123/O2•-
0 min
2 min
4 min
6 min
8 min
10 min
FL Intensity (x10³)
Wavelength (nm)

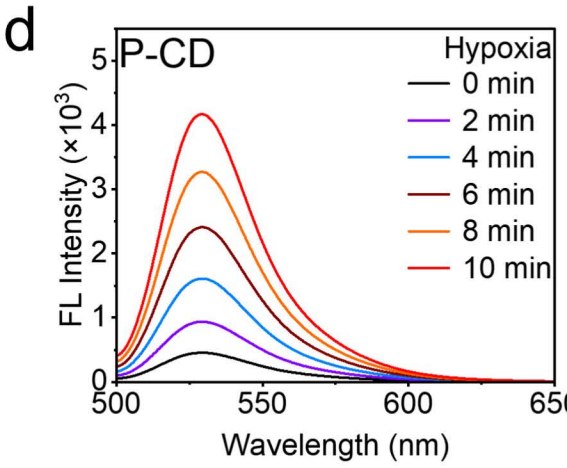
d
P-CD
Hypoxia
0 min
2 min
4 min
6 min
8 min
10 min
FL Intensity (×10³)
Wavelength (nm)

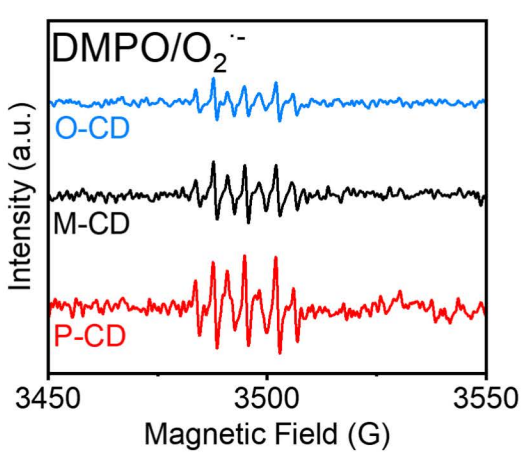
e
DMPO/O2•-
O-CD
M-CD
P-CD
Intensity (a.u.)
Magnetic Field (G)

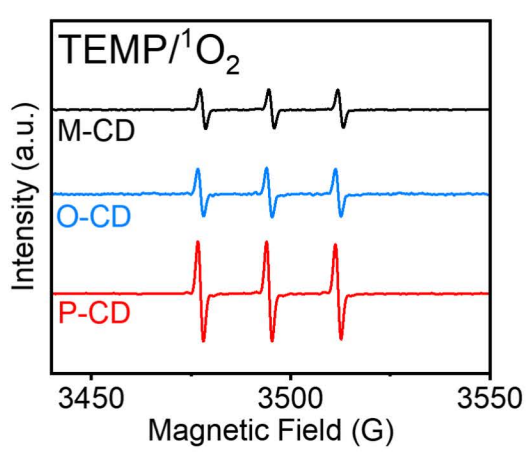
f
TEMP/1O2
M-CD
O-CD
P-CD
Intensity (a.u.)
Magnetic Field (G)

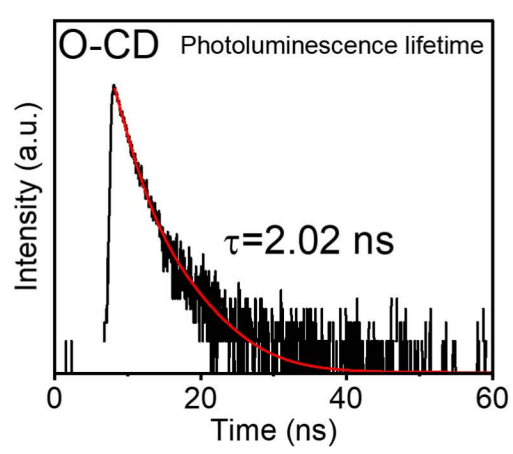
g
O-CD
Photoluminescence lifetime
τ=2.02 ns
Intensity (a.u.)
Time (ns)

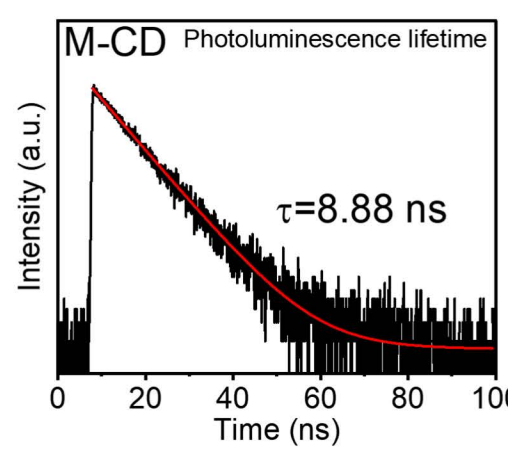
h
M-CD
Photoluminescence lifetime
τ=8.88 ns
Intensity (a.u.)
Time (ns)

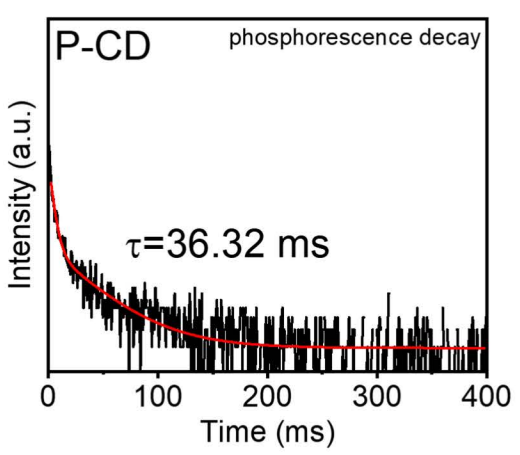
i
P-CD
phosphorescence decay
τ=36.32 ms
Intensity (a.u.)
Time (ms)

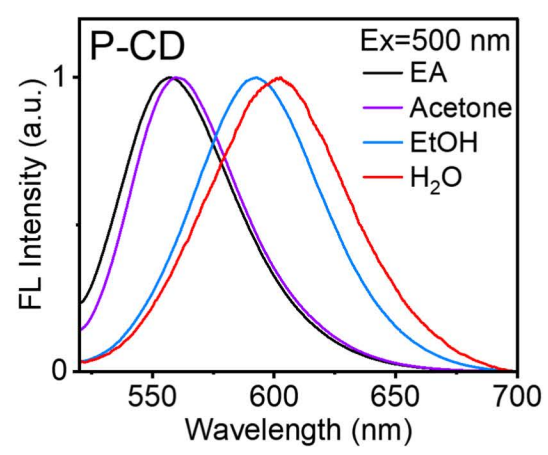
j
P-CD
Ex=500 nm
EA
Acetone
EtOH
H2O
FL Intensity (a.u.)
Wavelength (nm)

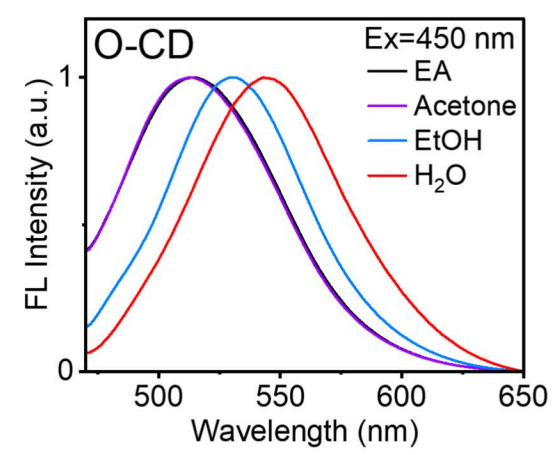
O-CD
Ex=450 nm
EA
Acetone
EtOH
H2O
FL Intensity (a.u.)
Wavelength (nm)

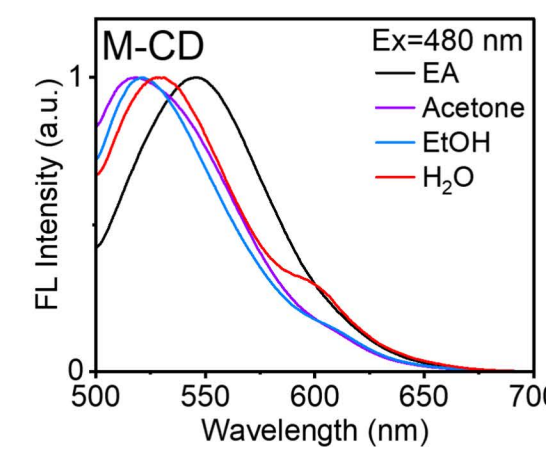
M-CD
Ex=480 nm
EA
Acetone
EtOH
H2O
FL Intensity (a.u.)
Wavelength (nm)

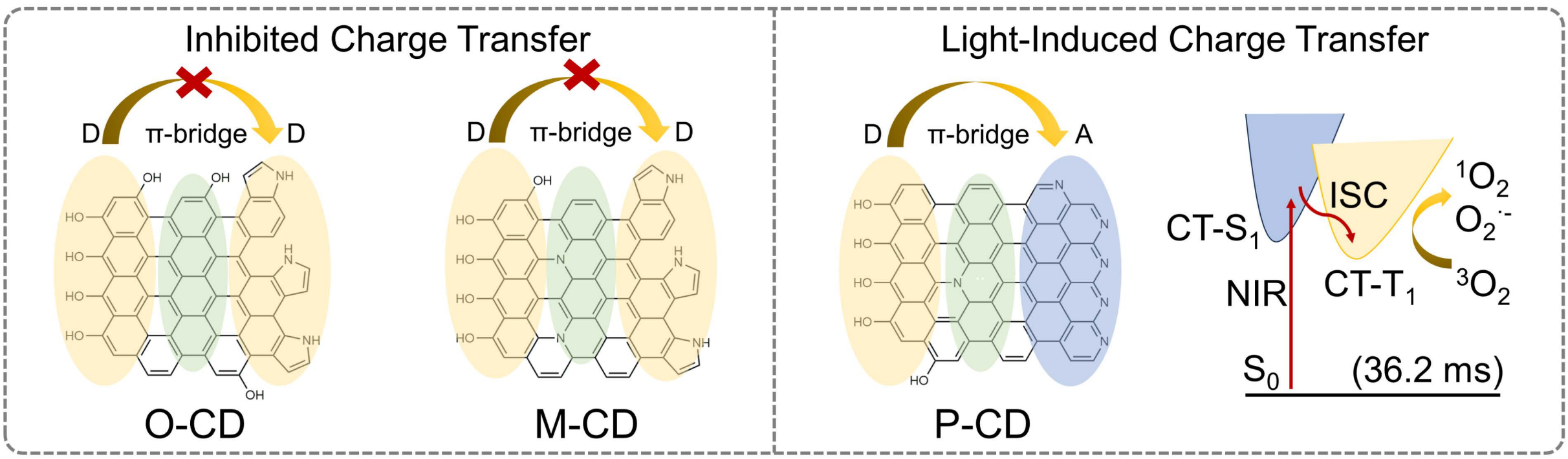
k
Inhibited Charge Transfer
D
π-bridge
D
O-CD
M-CD
Light-Induced Charge Transfer
D
π-bridge
A
P-CD
CT-S1
ISC
1O2
O2•-
3O2
CT-T1
NIR
S0
(36.2 ms)

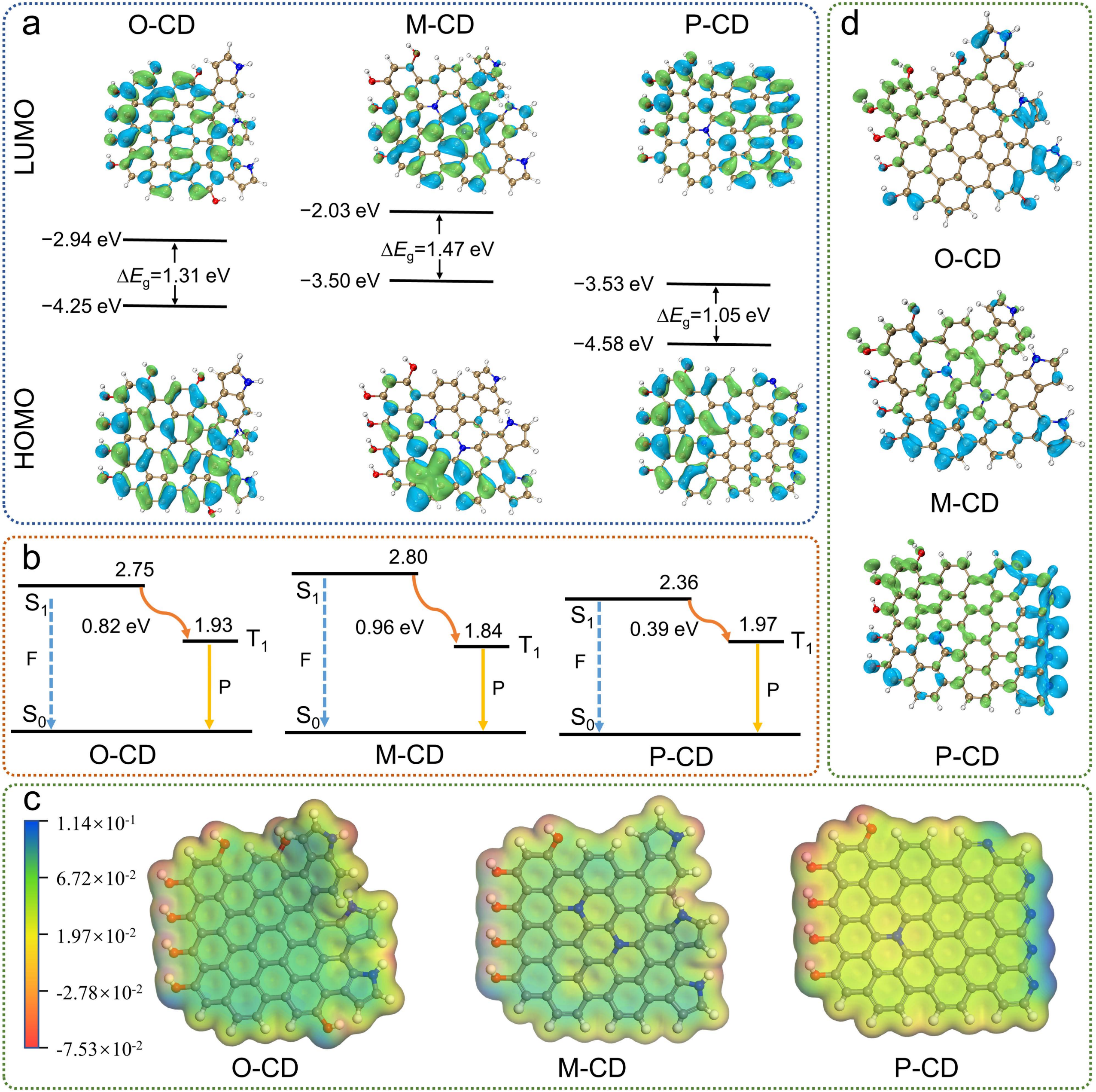
a
O-CD
M-CD
P-CD
LUMO
HOMO
−2.94 eV
ΔEg=1.31 eV
−4.25 eV
−2.03 eV
ΔEg=1.47 eV
−3.50 eV
−3.53 eV
ΔEg=1.05 eV
−4.58 eV
b
2.75
S1
0.82 eV
1.93
T1
F
P
S0
O-CD
2.80
S1
0.96 eV
1.84
T1
F
P
S0
M-CD
2.36
S1
0.39 eV
1.97
T1
F
P
S0
P-CD
d
O-CD
M-CD
P-CD
C
1.14×10-1
6.72×10-2
1.97×10-2
-2.78×10-2
-7.53×10-2
O-CD
M-CD
P-CD

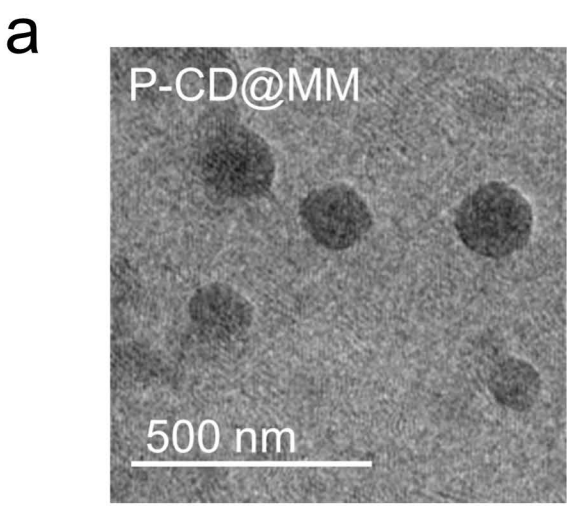

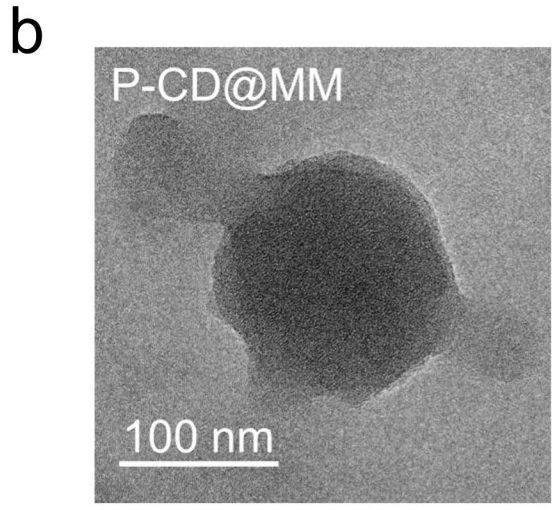

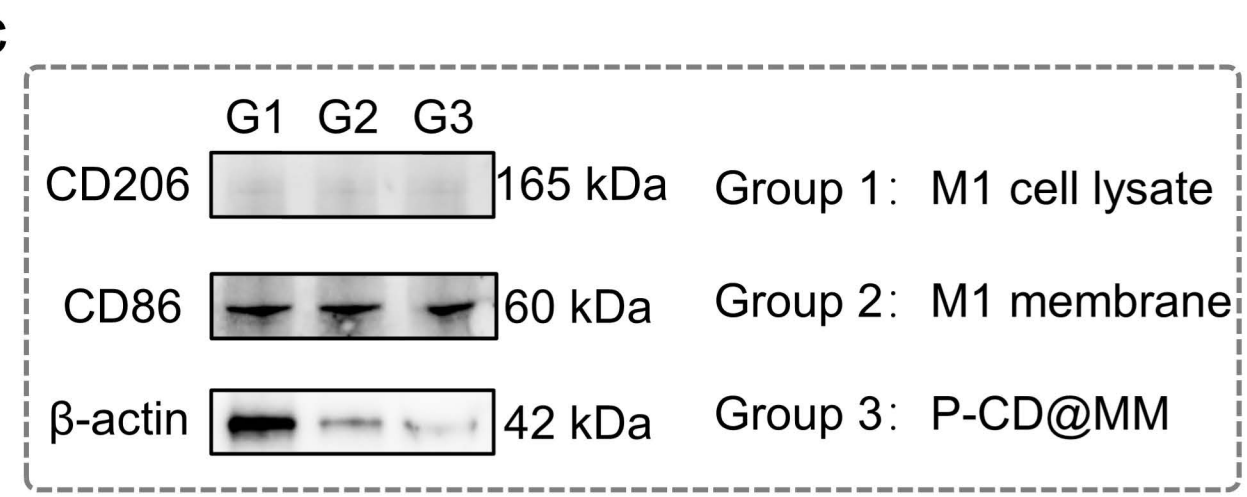

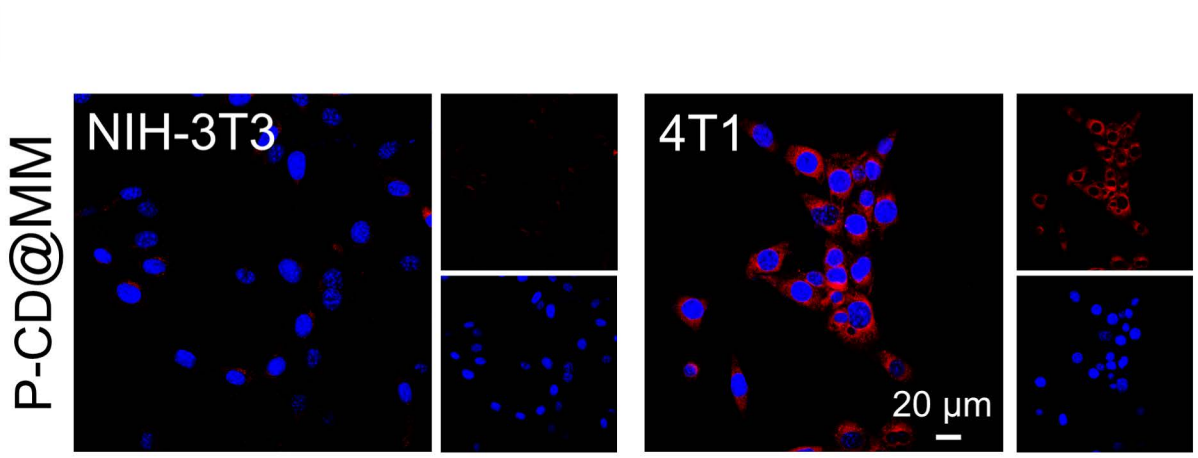

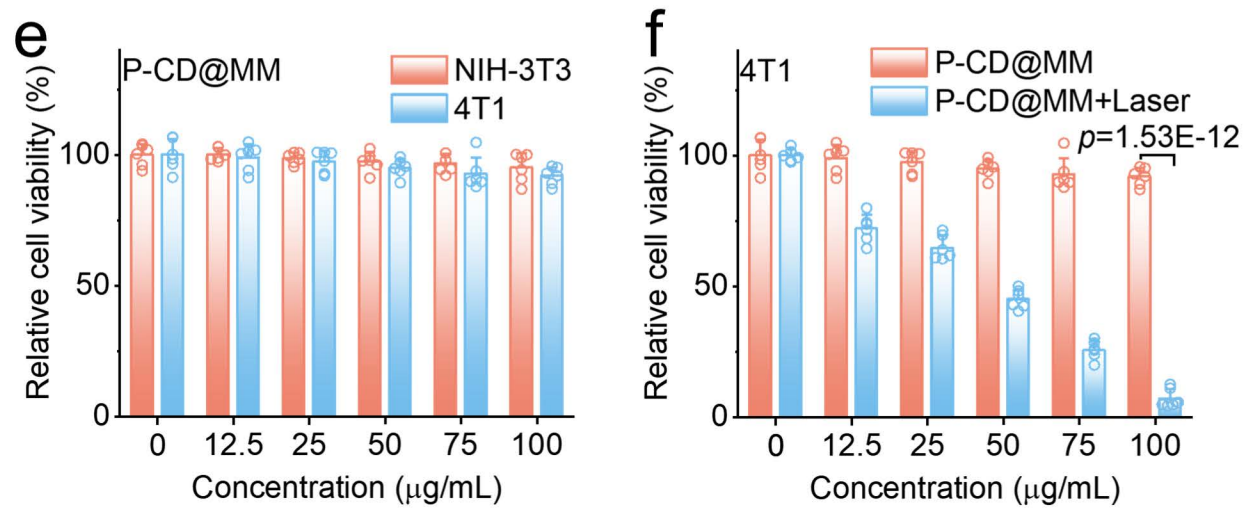

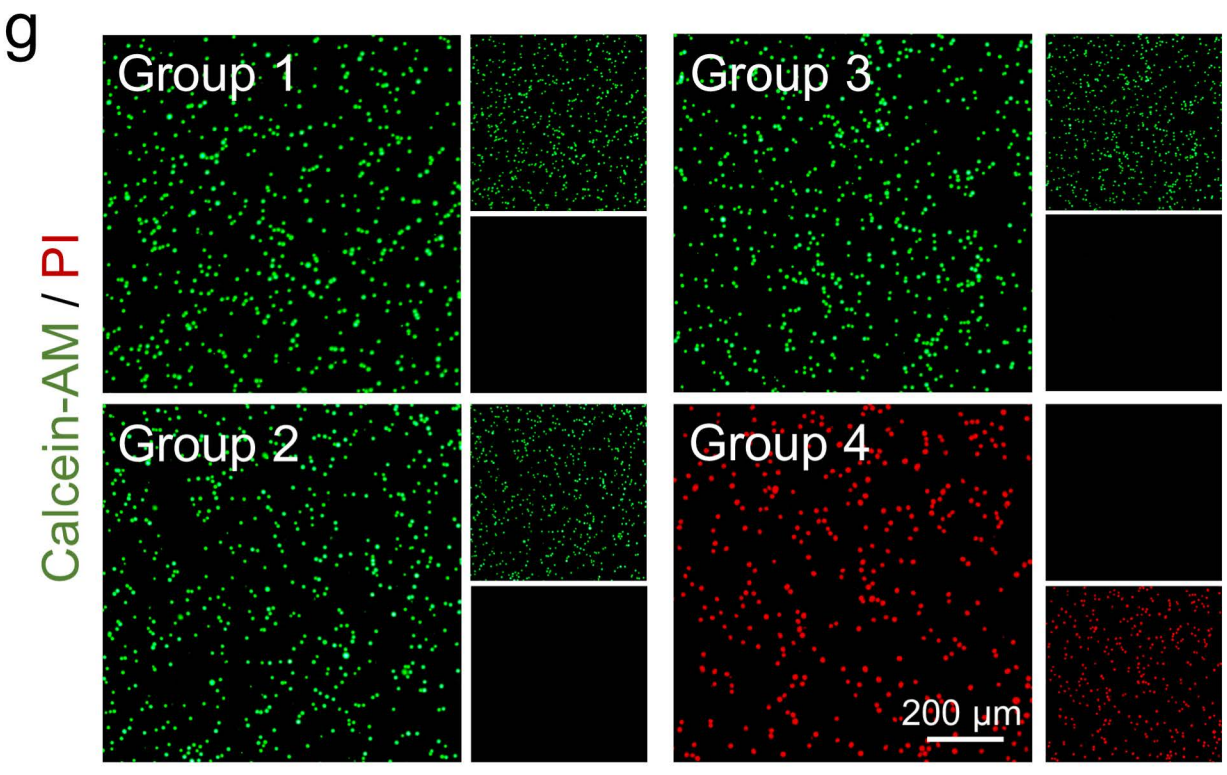

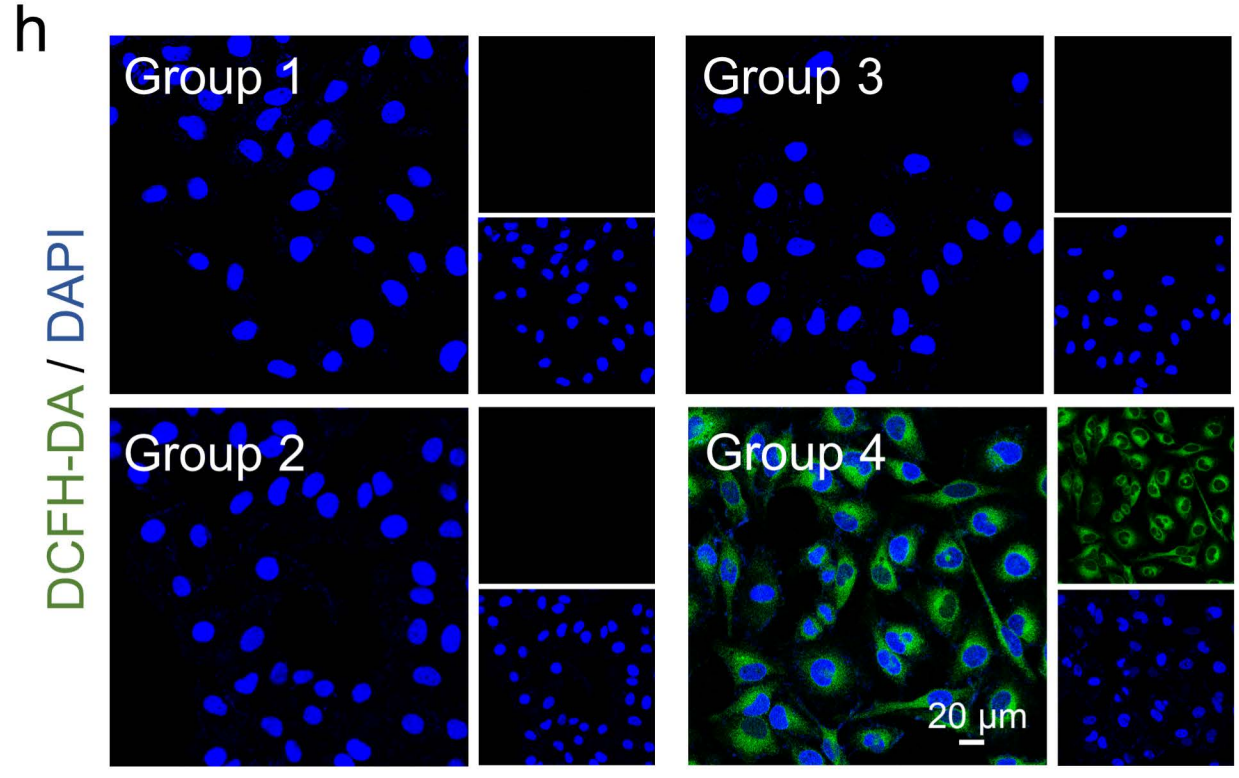

Group 1: Control Group 2: Laser Group 3: P-CD@MM Group 4: P-CD@MM + Laser

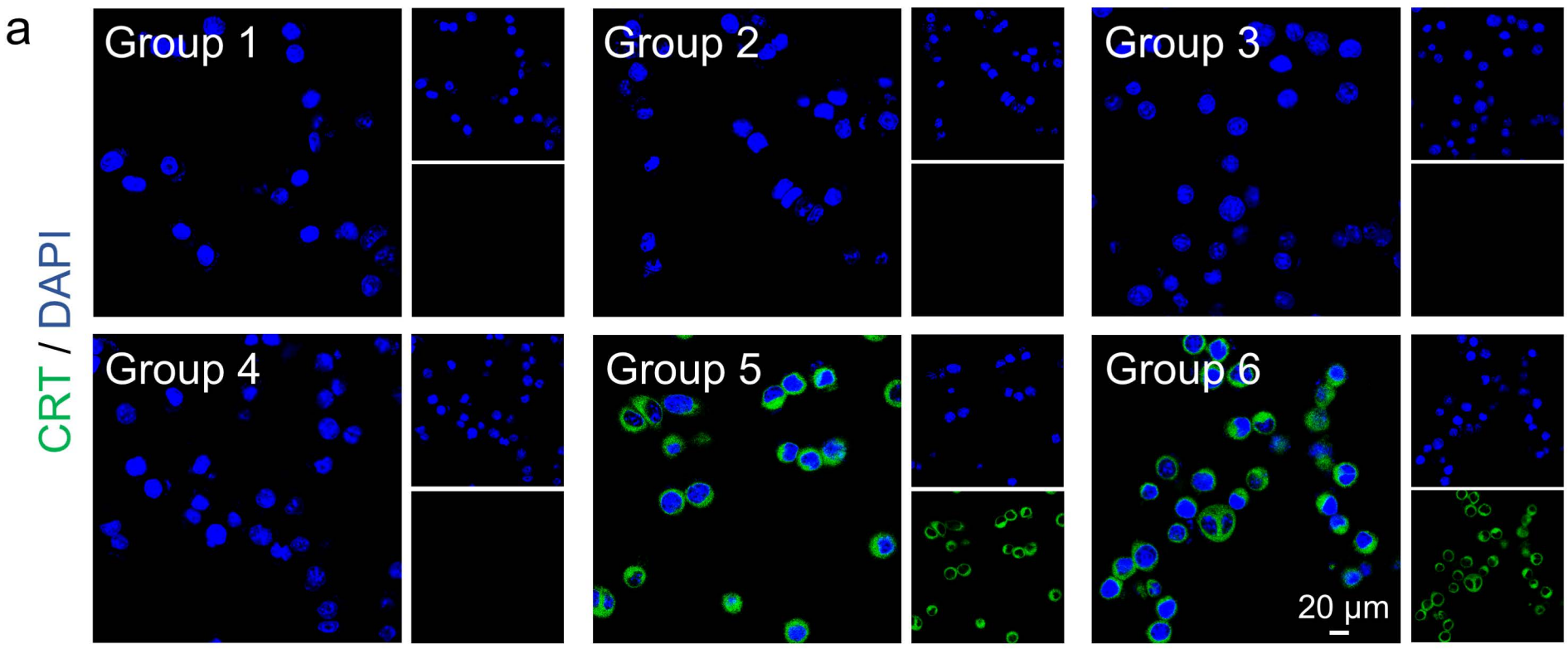
a
Group 1
Group 2
Group 3
Group 4
Group 5
Group 6
CRT / DAPI
20 μm

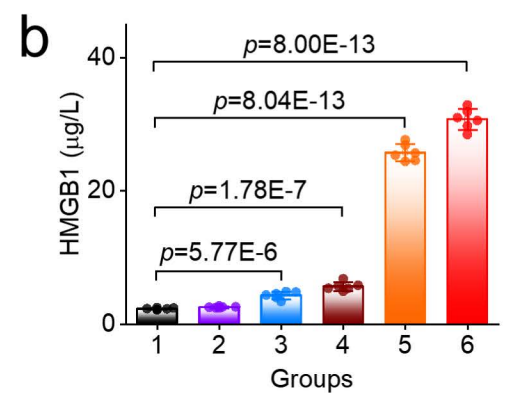
b
HMGB1 (μg/L)
p=8.00E-13
p=8.04E-13
p=1.78E-7
p=5.77E-6
Groups
c
ATP (μM)
p=1.53E-12
p=1.72E-13
p=2.96E-5
p=0.0032
Groups

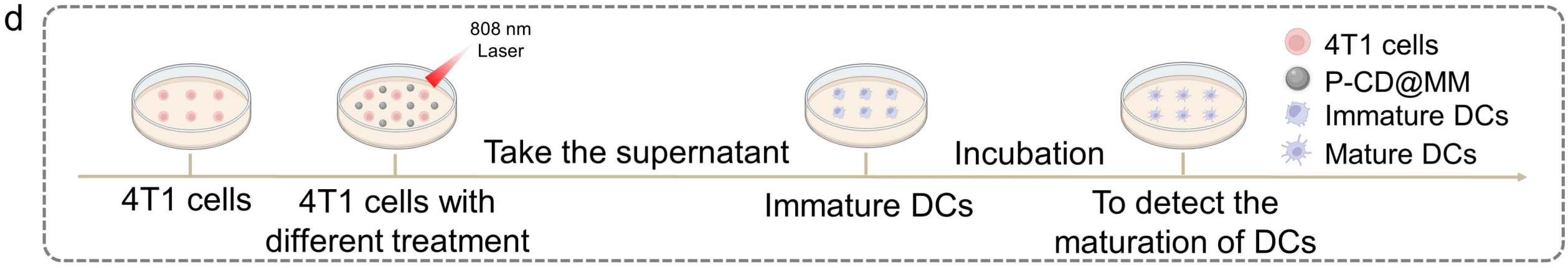
d
808 nm
Laser
Take the supernatant
Incubation
4T1 cells
P-CD@MM
Immature DCs
Mature DCs
4T1 cells
4T1 cells with
different treatment
Immature DCs
To detect the
maturation of DCs

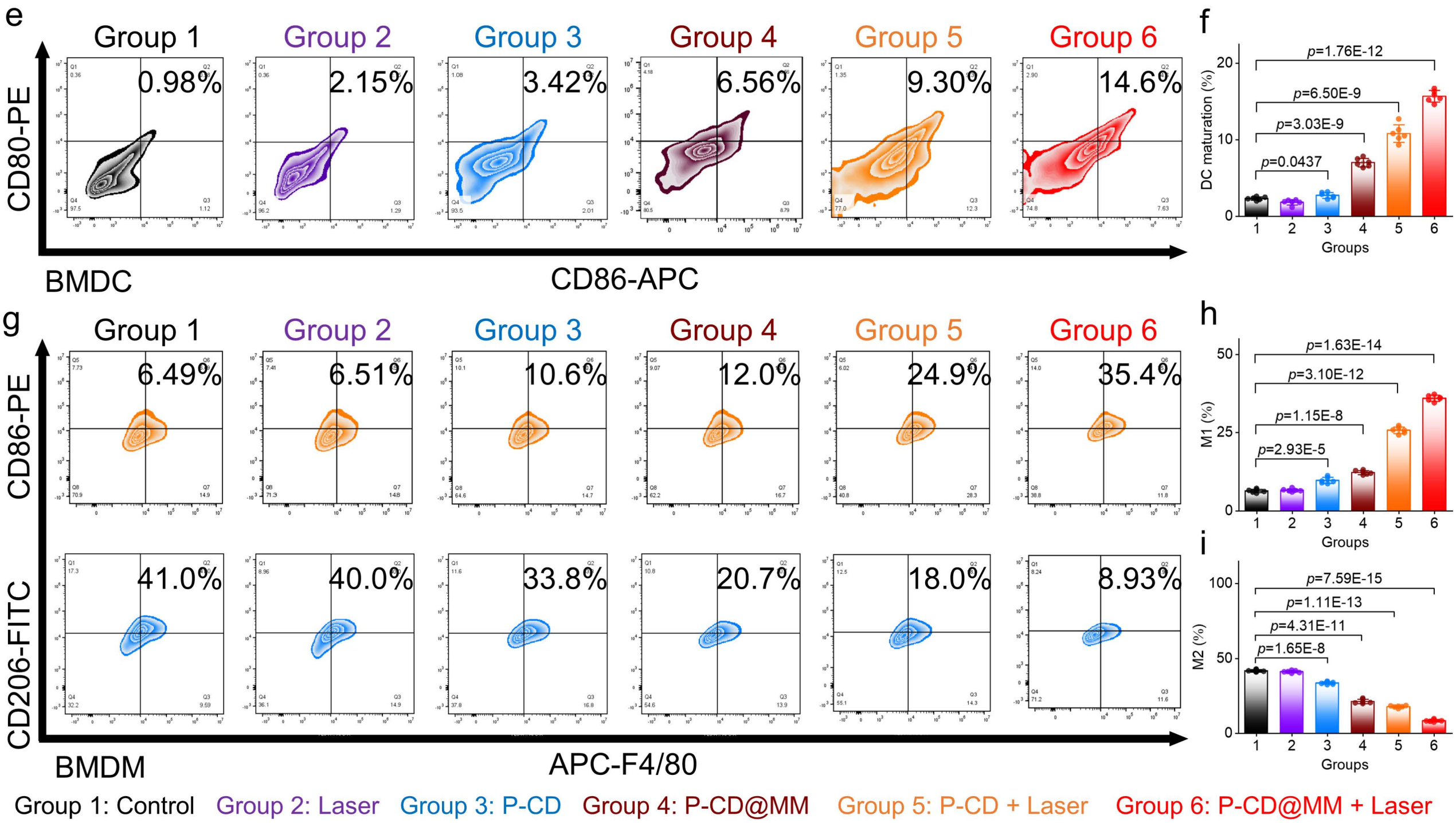
e
Group 1
Group 2
Group 3
Group 4
Group 5
Group 6
0.98%
2.15%
3.42%
6.56%
9.30%
14.6%
CD80-PE
BMDC
CD86-APC
f
DC maturation (%)
p=1.76E-12
p=6.50E-9
p=3.03E-9
p=0.0437
Groups
g
Group 1
Group 2
Group 3
Group 4
Group 5
Group 6
6.49%
6.51%
10.6%
12.0%
24.9%
35.4%
41.0%
40.0%
33.8%
20.7%
18.0%
8.93%
CD86-PE
CD206-FITC
BMDM
APC-F4/80
h
M1 (%)
p=1.63E-14
p=3.10E-12
p=1.15E-8
p=2.93E-5
Groups
i
M2 (%)
p=7.59E-15
p=1.11E-13
p=4.31E-11
p=1.65E-8
Groups
Group 1: Control
Group 2: Laser
Group 3: P-CD
Group 4: P-CD@MM
Group 5: P-CD + Laser
Group 6: P-CD@MM + Laser

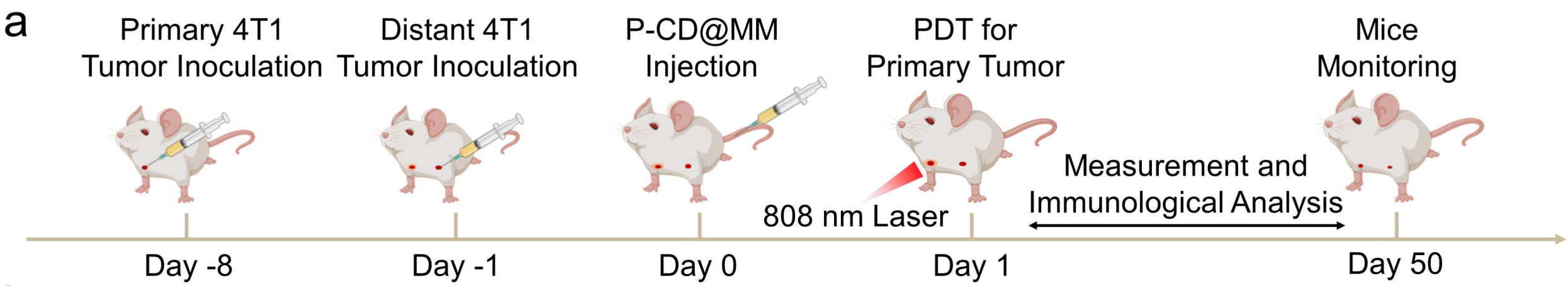

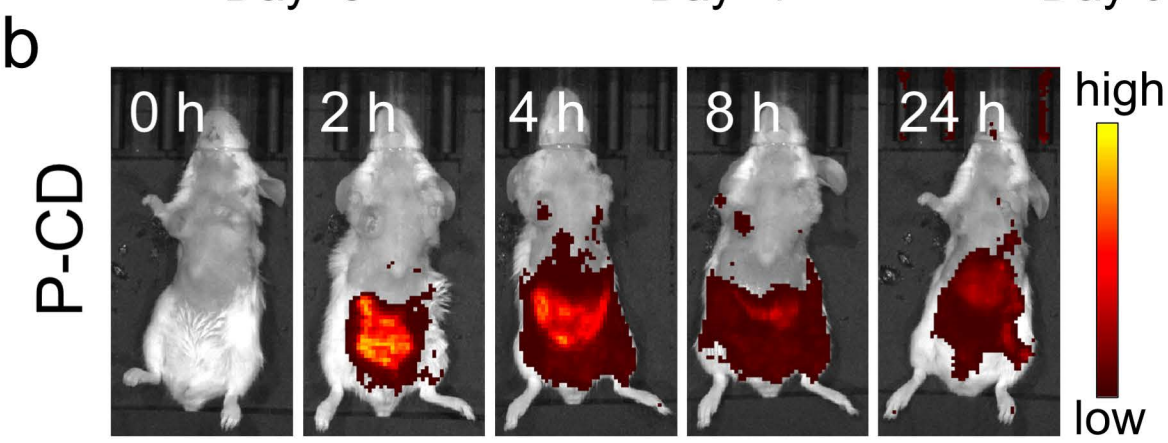

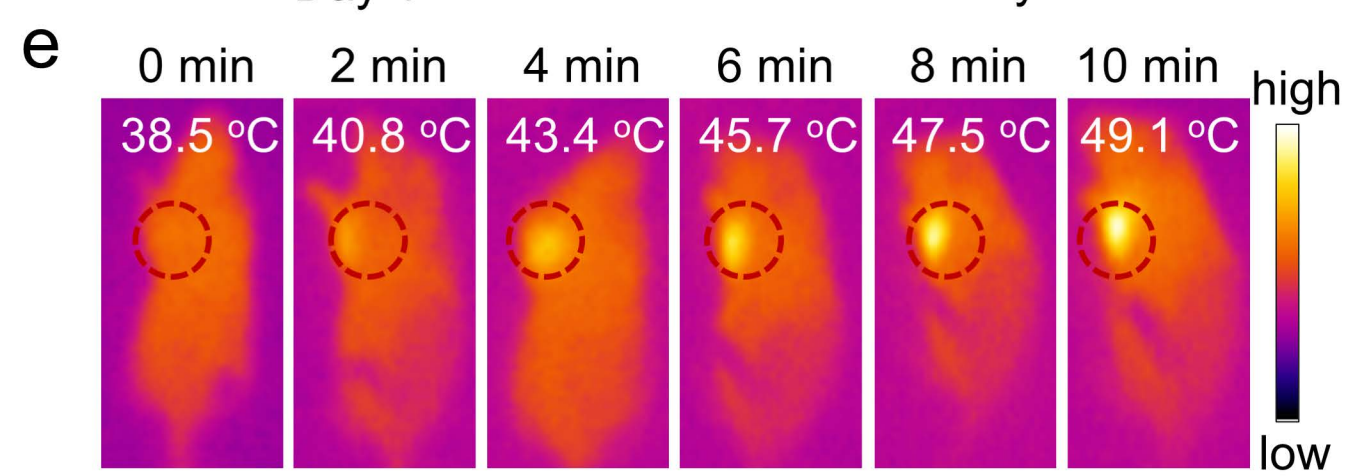

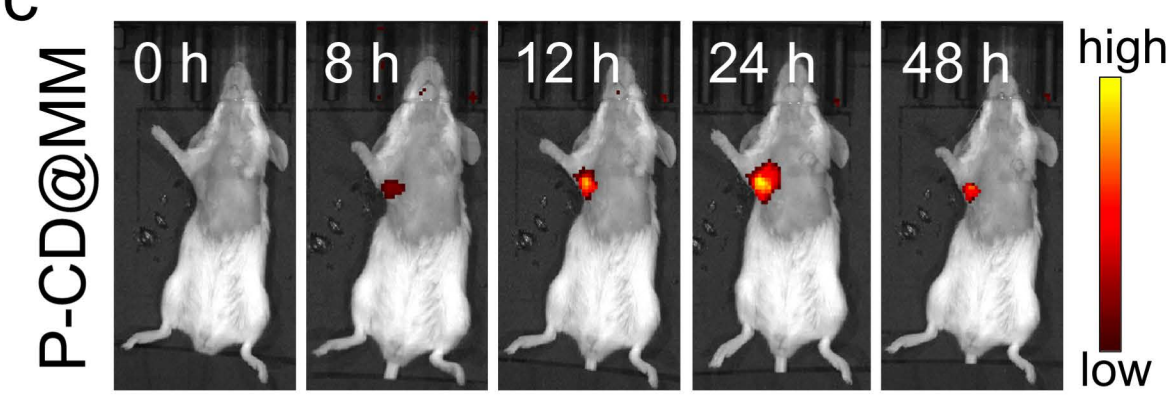

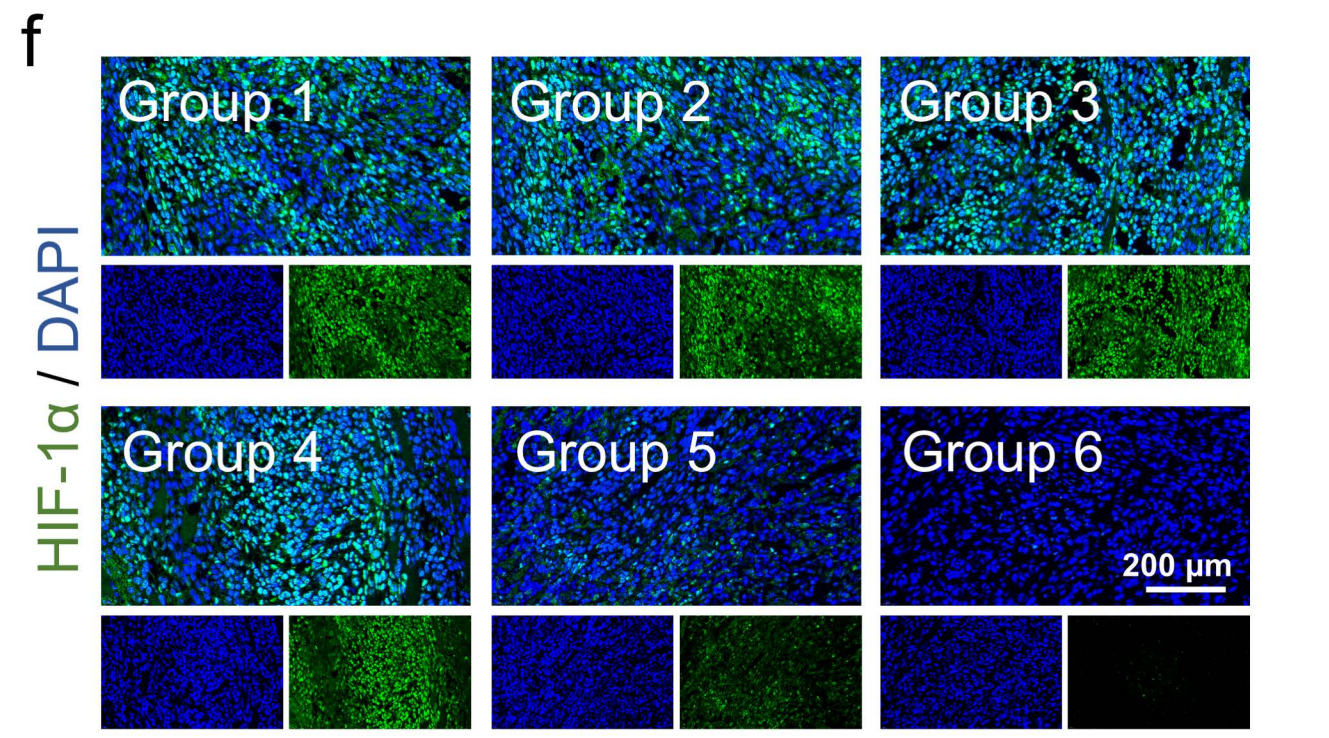

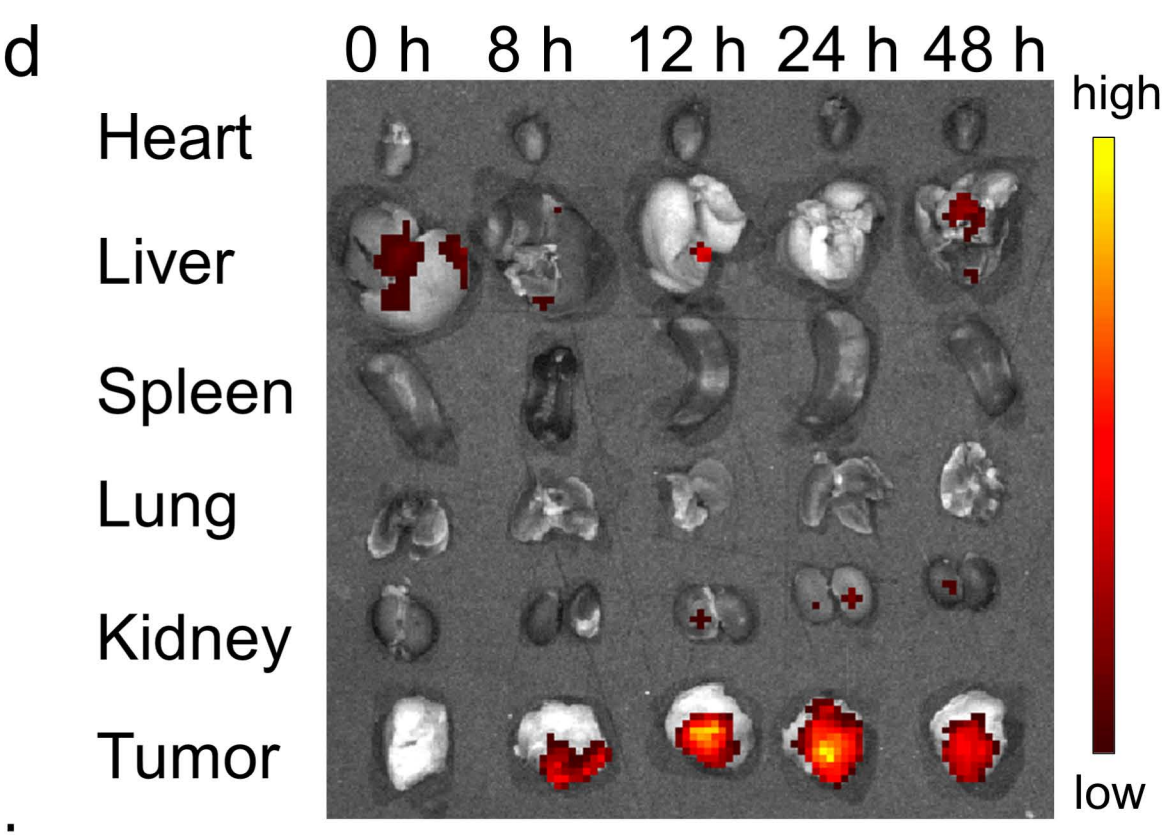

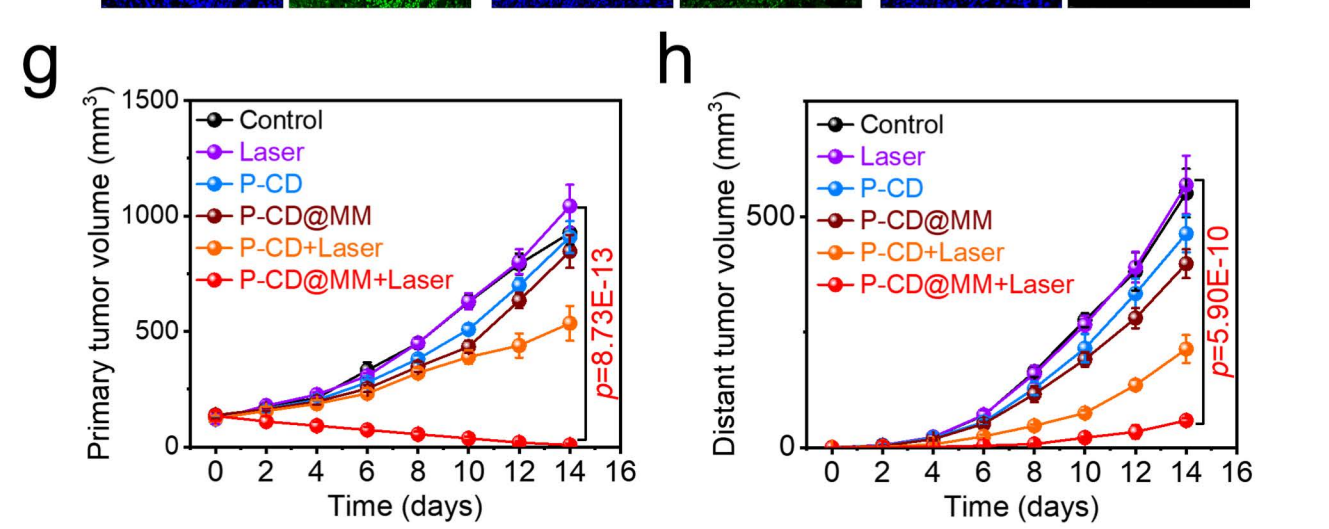

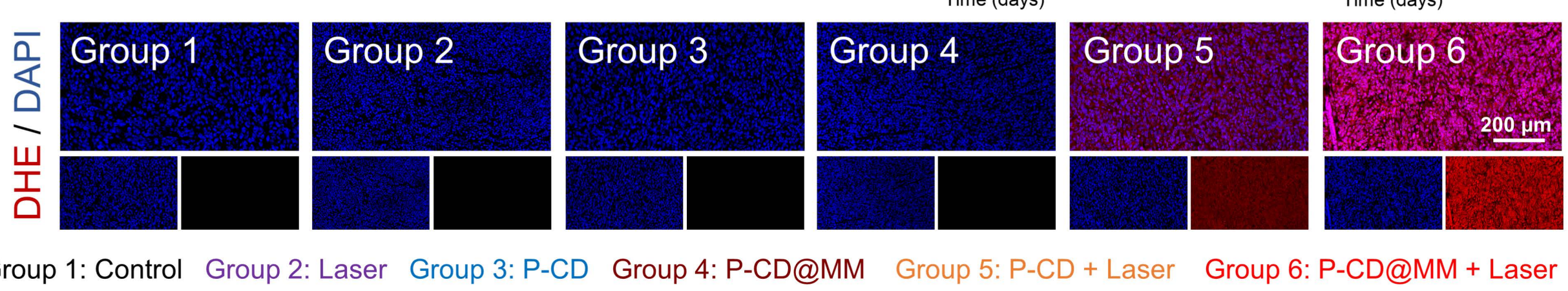

Group 1: Control Group 2: Laser Group 3: P-CD Group 4: P-CD@MM Group 5: P-CD + Laser Group 6: P-CD@MM + Laser

a

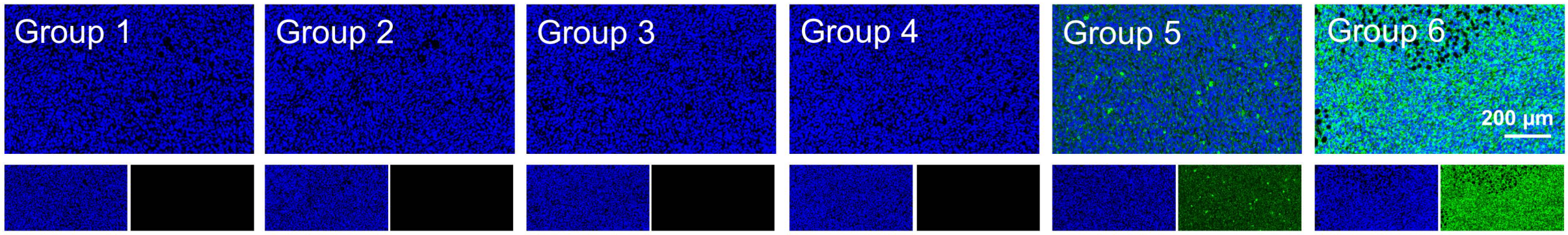

b

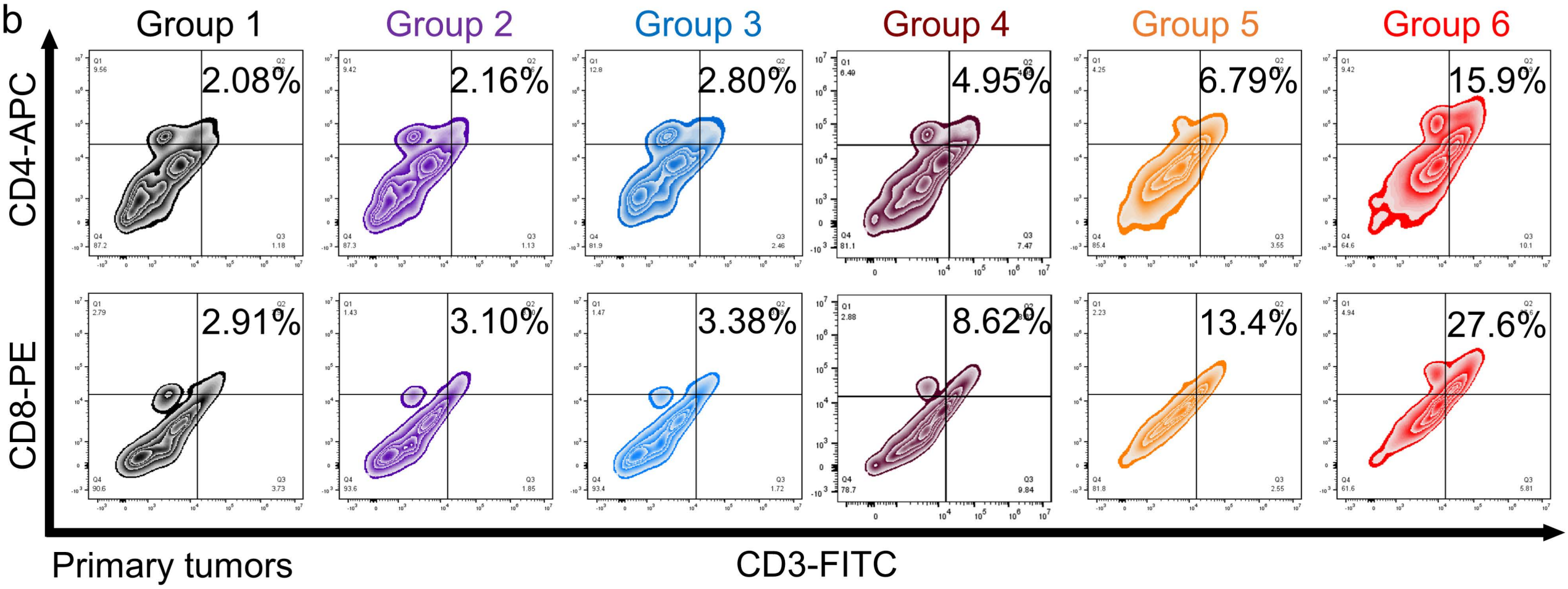

c

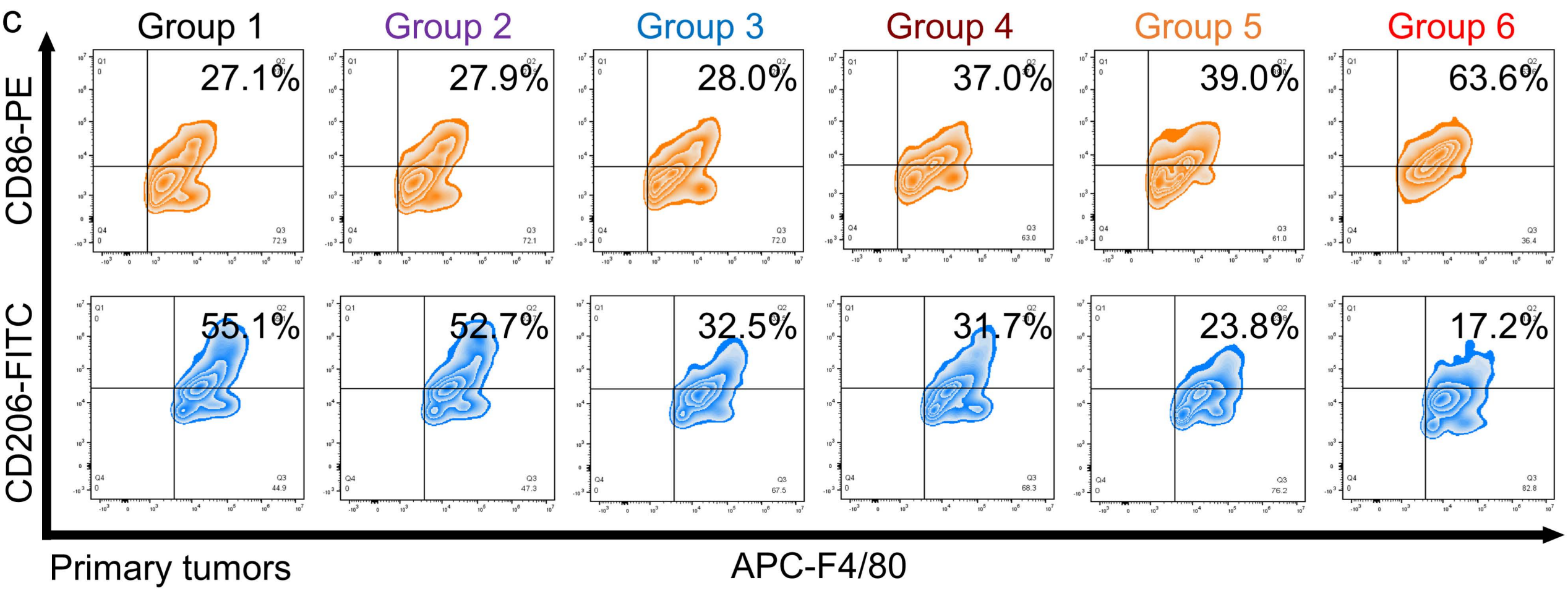

d

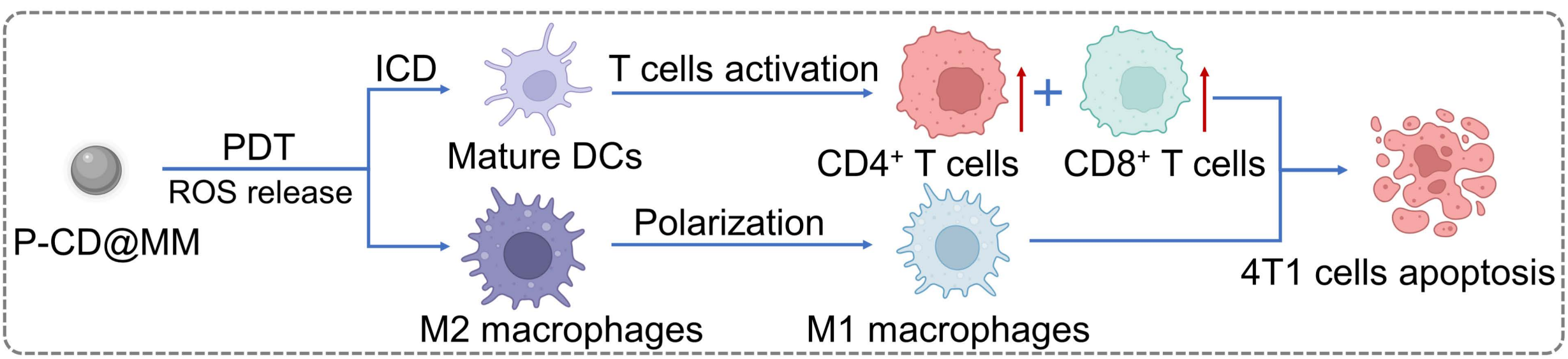

Group 1: Control Group 2: Laser Group 3: P-CD Group 4: P-CD@MM Group 5: P-CD + Laser Group 6: P-CD@MM + Laser

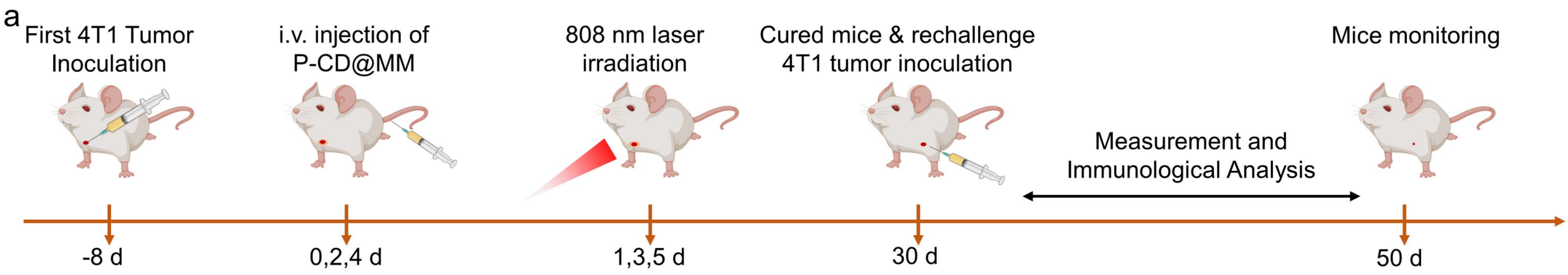
a
First 4T1 Tumor Inoculation
i.v. injection of P-CD@MM
808 nm laser irradiation
Cured mice & rechallenge 4T1 tumor inoculation
Mice monitoring
Measurement and Immunological Analysis
-8 d
0,2,4 d
1,3,5 d
30 d
50 d

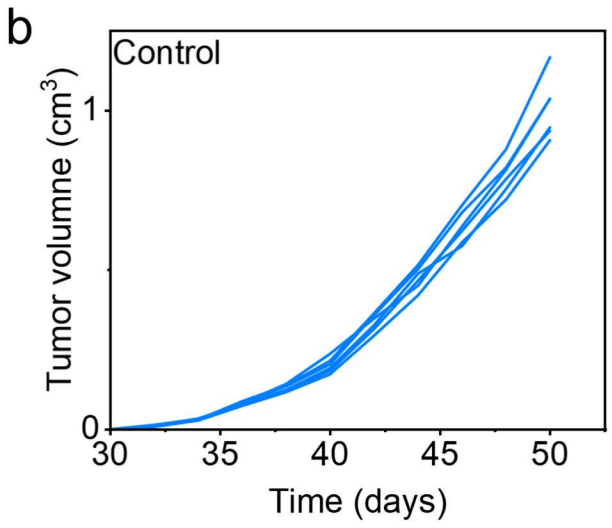
b
Control
Tumor volumne (cm3)
Time (days)

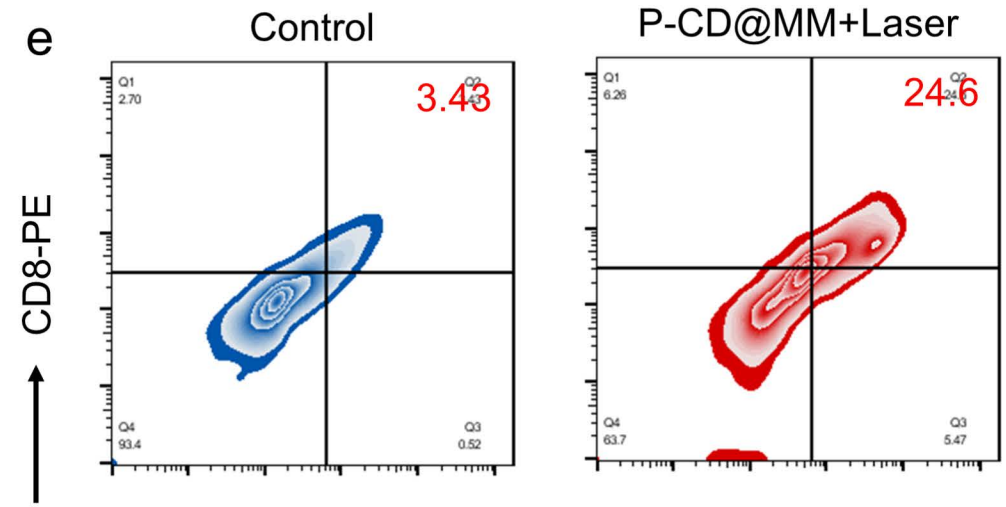
e
Control
P-CD@MM+Laser
3.43
24.6
CD8-PE

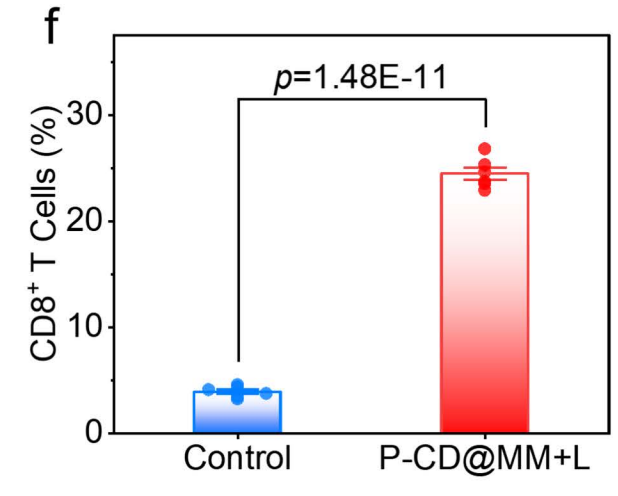
f
p=1.48E-11
CD8+ T Cells (%)
Control
P-CD@MM+L

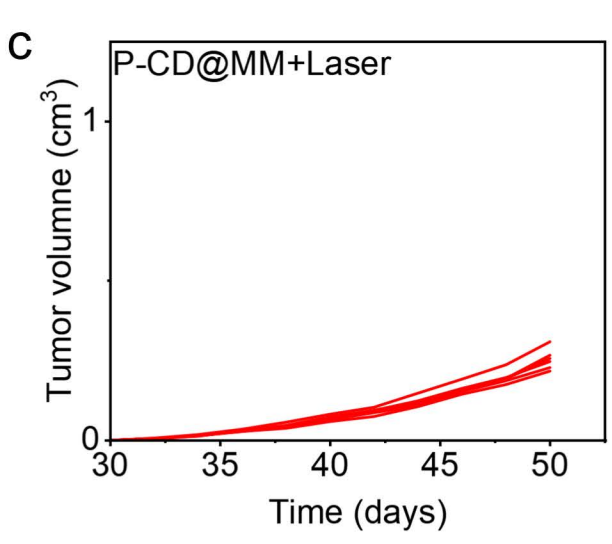
c
P-CD@MM+Laser
Tumor volumne (cm3)
Time (days)

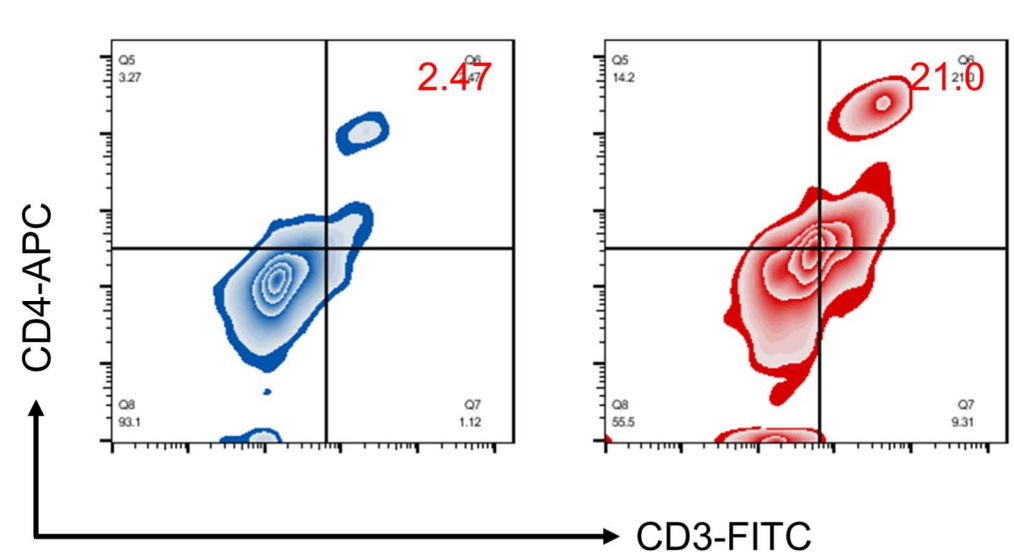
2.47
21.0
CD4-APC
CD3-FITC

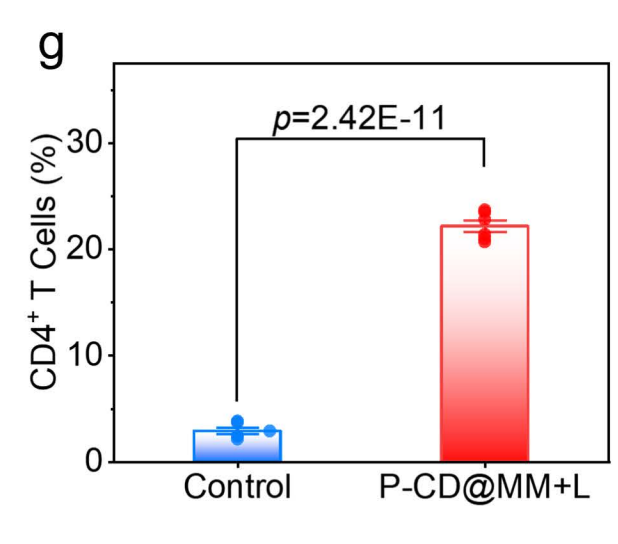
g
p=2.42E-11
CD4+ T Cells (%)
Control
P-CD@MM+L

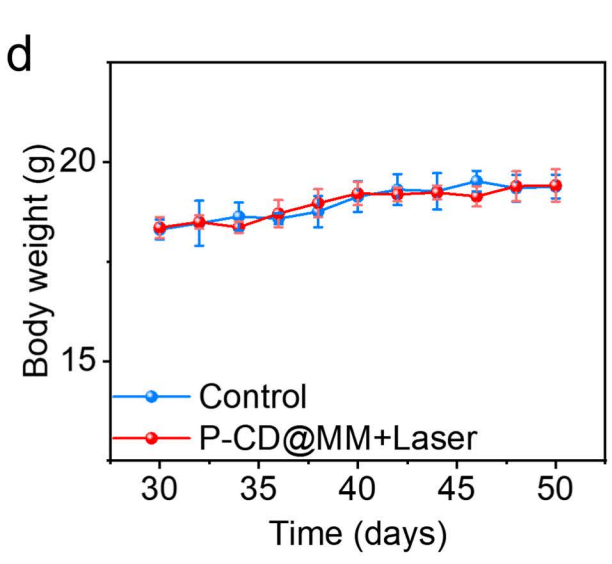
d
Body weight (g)
Control
P-CD@MM+Laser
Time (days)

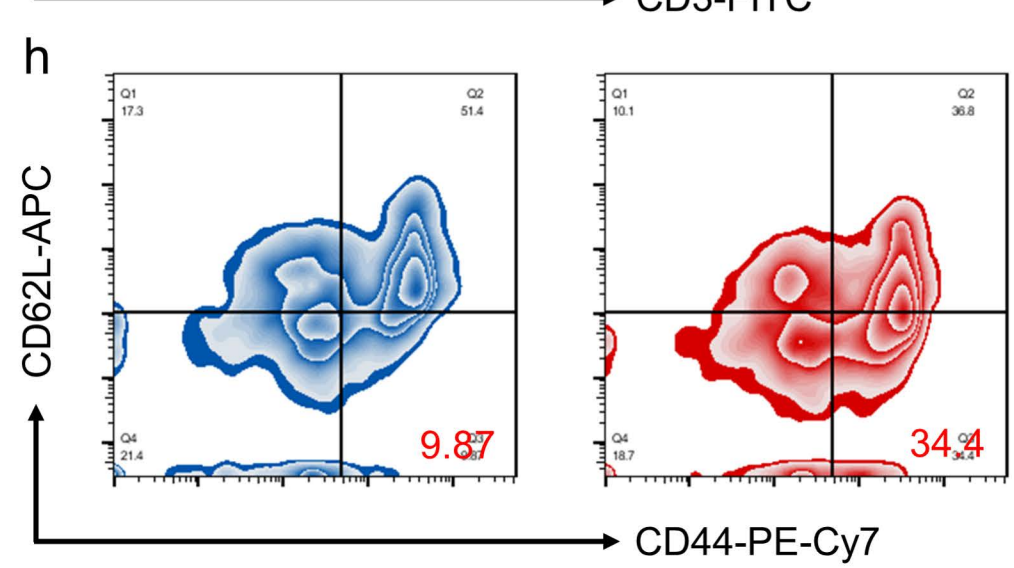
h
9.87
34.4
CD62L-APC
CD44-PE-Cy7

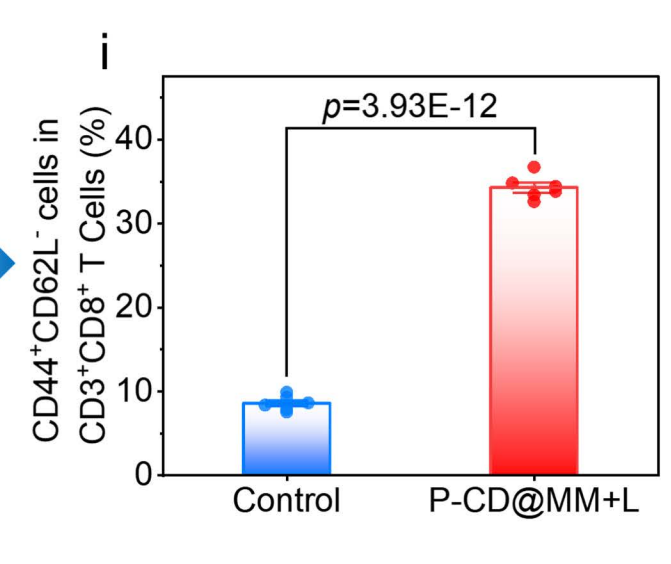
i
p=3.93E-12
CD44+CD62L- cells in CD3+CD8+ T Cells (%)
Control
P-CD@MM+L